

Spontaneous otoacoustic emissions  
in an active nonlinear time domain  
model of the cochlea

DISSERTATION

zur Erlangung des akademischen Grades  
Doctor rerum naturalium  
(Dr. rer. nat.)  
im Fach Physik

vorgelegt

der Fakultät Mathematik und Naturwissenschaften  
der Technischen Universität Dresden

von

Dipl.–Math. Florian David Fruth  
geboren am 31. März 1984 in Leimen

Eingereicht am 04.10.2013.

1. Gutachter:

2. Gutachter:

# Abstract

The auditory systems of numerous species including humans exhibit remarkable properties. Mammalian hearing is characterized by four hallmarks, given by an extreme sensitivity, a wide dynamic range, a sharp frequency selectivity, and spontaneous otoacoustic emissions (SOAEs). The last-mentioned are sounds which are generated by the cochlea, the hearing organ within the inner ear, in absence of external stimulation and become manifest as pressure fluctuations in the ear canal. The four characteristics, in particular SOAEs, are associated with an active nonlinear amplification process taking place on a mechanical level in the cochlea. A previously proposed generic one-dimensional model of the human cochlea in the frequency domain, which comprises hydrodynamically coupled critical oscillators of gradually varying eigenfrequencies, was found to capture three of the four characteristics, with exception of the fourth characteristic, SOAEs. In this thesis, we extend the above frequency domain model and propose a spatially discrete, active nonlinear one-dimensional model of the cochlea in the time domain describing human SOAEs including their basic statistical features. We consider the distribution of the frequencies of emissions ranging from 0.5 to 8 kHz, the monotonically decaying distribution of the numbers of emissions per cochlea, and the distribution of the distances between neighboring emissions exhibiting a maximum at one semitone. By means of a combination of mainly elastic longitudinal coupling with a weak dissipative part, clusters of synchronized oscillators appear in our model, resulting in a preferred minimal distance between neighboring spontaneous emissions. The model we propose captures all three above mentioned experimental distributions of SOAEs by employing dynamical noise, elastic and dissipative longitudinal coupling, and irregularities in the bifurcation parameter, which are normally distributed and exponentially correlated in space. Thus, the model can account for all four hallmarks of human hearing including essential statistical features of SOAEs.

# Kurzfassung

Die auditorischen Organe vieler Tierarten inklusive des Menschen weisen bemerkenswerte Eigenschaften auf. Der Gehörsinn von Säugetieren wird anhand von vier Hauptmerkmalen charakterisiert: Eine hohe Empfindlichkeit, ein großer dynamischer Bereich, eine scharfe Frequenzselektivität und spontane otoakustische Emissionen (SOAEs). Letztere sind Geräusche, die von der Cochlea, dem Hörorgan im Innenohr, in Abwesenheit von äußerer Stimulation produziert werden und als Druckschwankungen im Ohrkanal messbar sind. Die vier Hauptmerkmale, insbesondere SOAEs, stehen in Verbindung zu einer aktiven nichtlinearen Signalverstärkung, die auf mechanischer Ebene in der Cochlea abläuft. Ein von anderen Autoren entwickeltes generisches eindimensionales Modell der menschlichen Cochlea im Frequenzbereich, das aus hydrodynamisch gekoppelten kritischen Oszillatoren mit graduell variierenden Eigenfrequenzen besteht, beschreibt drei der vier Charakteristiken des Gehörsystems, mit Ausnahme der vierten Charakteristik, der SOAEs. In der vorliegenden Dissertation erweitern wir das obige Modell im Frequenzbereich und präsentieren ein räumlich diskretes, aktives nichtlineares eindimensionales Cochlea-Modell im Zeitbereich, das menschliche SOAEs und deren grundlegenden statistischen Eigenschaften beschreibt. Wir betrachten die Verteilung der Emissionsfrequenzen, welche von 0.5 bis 8 kHz reichen, die monoton abfallende Verteilung der Anzahl der Emissionen pro Cochlea und die Verteilung der Frequenzabstände benachbarter Emissionen, die ein Maximum bei einem Halbton aufweist. Eine Kombination aus vorwiegend elastischer und einem schwachen Anteil von dissipativer longitudinaler Kopplung führt zur Entstehung synchronisierter Gruppen von Oszillatoren in unserem Modell und so zu einem präferierten Mindestabstand benachbarter spontaner Emissionen. Unser Modell beschreibt alle drei obigen experimentellen Verteilungen unter Verwendung von dynamischem Rauschen, elastischer und dissipativer longitudinaler Kopplung sowie statischer Unordnung im Bifurkationsparameter, die normalverteilt und exponentiell korreliert im Raum ist. Somit weist das Modell alle vier Hauptmerkmale des menschlichen Gehörsinnes auf, inklusive grundlegender Statistiken spontaner Emissionen.

# Acknowledgements

First of all I, would like to thank my two supervisors. This thesis would not have been possible without the vast knowledge, guidance, and extraordinary support of Prof. Dr. Benjamin Lindner and Prof. Dr. Frank Jülicher. I am grateful for the opportunity to join the group of Prof. Dr. Frank Jülicher at the Max Planck Institute for the Physics of Complex Systems. In addition, I am indebted to Prof. Dr. Benjamin Lindner for his patience and intensive supervision of my research, and for giving me the chance to go to Berlin with him to join his group at the Bernstein Center for Computational Neuroscience.

Furthermore, I would like to thank the members of the committee and the two referees for their efforts.

The theoretical results presented in this thesis are compared to experimental results, which were generously provided by Prof. Dr. Carrick Talmadge, who I want to thank for his great support.

I would also like to express my gratitude to Dr. Christian Schreiber. First of all, he is a dear friend. Besides, he was the one who encouraged me to apply at the Max Planck Institute for the Physics of Complex Systems, and he proofread a substantial part of this manuscript. Furthermore, I want to thank Ellie Mutchler for being an awesome dancing partner and friend, and for proofreading. I am grateful for the support of my awesome colleagues, in particular Dr. Kai Dierkes, who was of great help during my time in Dresden, as well as Stefan Wieland, Sergej Voronenko, Felix Droste, and Sven Blankenburg for proofreading and making valuable comments on this manuscript.

Many friends and acquaintances made the past years in Dresden and Berlin a wonderful time. In order not to forget someone, I hereby thank you all, in particular all those who spent countless hours with me playing foosball or dancing tango. Last but not not least, I would like to thank my family, i.e. my mother, father, the wife of my father, my cousins, uncle and aunts, and my grandma for their constant support.



# Contents

<b>1</b>	<b>Introduction</b>	<b>1</b>
1.1	Biophysics of hearing . . . . .	2
1.1.1	Physiology of the cochlea and active amplification . . . . .	2
1.1.2	Historical overview . . . . .	8
1.1.3	Otoacoustic emissions - measures and models . . . . .	11
1.2	The physics of waves . . . . .	16
1.2.1	Linear wave propagation in one dimension . . . . .	16
1.2.2	Nonlinear waves . . . . .	17
1.3	Active oscillators . . . . .	20
1.3.1	Hopf bifurcation . . . . .	21
1.3.2	Noisy oscillators . . . . .	23
1.4	Models of the mammalian cochlea . . . . .	24
1.4.1	Linear models . . . . .	25
1.4.2	Nonlinear models . . . . .	26
1.5	Organization of the thesis . . . . .	29
<b>2</b>	<b>Simple model for nonlinear waves in the cochlea</b>	<b>31</b>
2.1	Wave propagation by critical oscillators . . . . .	31
2.2	Discretization of the equations and solution methods in the time domain . . . . .	36
2.3	Linear waves as a limit case of the nonlinear model . . . . .	43
2.4	Comparison with a frequency domain approximation . . . . .	45
2.5	Determination of incoming and outgoing pressure waves . . . . .	48
2.5.1	Extracting $\mathbf{p}_{in}$ in the time domain . . . . .	49
2.6	Low frequency modes . . . . .	50
<b>3</b>	<b>Effects of boundary conditions, longitudinal coupling and static disorder</b>	<b>55</b>
3.1	Dynamic boundary condition mediated by the middle ear . . . . .	56
3.2	Stimulus frequency otoacoustic emissions . . . . .	61
3.3	Spontaneous activity of the system . . . . .	64
3.4	Longitudinal coupling of oscillators . . . . .	66
3.5	Static disorder in the properties of oscillators and spontaneous emissions . . . . .	67

3.5.1	Characteristic frequency . . . . .	68
3.5.2	Oscillator nonlinearity . . . . .	69
3.5.3	Bifurcation parameter . . . . .	69
<b>4</b>	<b>Statistics of spontaneous emissions in the model and in vivo</b>	<b>71</b>
4.1	Emission frequencies . . . . .	76
4.2	Emission numbers . . . . .	77
4.3	Relative frequency intervals between emissions . . . . .	80
4.4	Stimulus frequency otoacoustic emissions revisited . . . . .	90
4.5	Extensions of the model . . . . .	91
<b>5</b>	<b>Summary and conclusions</b>	<b>97</b>
	Bibliography . . . . .	103

# Chapter 1

## Introduction

One essential sense enabling us to perceive our surrounding environment is the auditory sense, which detects even minuscule pressure fluctuations in the air. Although the act of hearing involves a considerable processing of information by the neural system, already on the mechanical level a considerable amount of processing and information filtering takes place. Despite its importance, the mechanics of hearing is not yet understood in detail. The basic principles and constituents are believed to be known, but the exact nature of the interplay between the components is unresolved. Put differently, how exactly the ear functions remains under debate.

This dissertation focuses on the mechanics of human hearing, which displays an active nonlinear amplification of incoming stimuli. This active mechanism of the human auditory system possesses four key features: First, the exquisite sensitivity of our auditory system allows for the recognition of faint sounds such as the rustling of leaves or the buzzing of mosquitos. Second, our auditory system covers a wide dynamic range of input stimuli and is thus also able to perceive intense sounds as well, for instance of airplanes taking off, where pressure levels are six orders of magnitude higher than rustling leaves. This is achieved without suffering from severe damages of the auditory system. Third, the ability to distinguish different frequencies of pure tones can reach values as low as 1‰ relative difference [140]. Setting this number in context, this is substantially less than the tones of two neighboring keys on a piano, corresponding to a difference of one semitone, which gives a relative frequency difference of about 6%. The fourth hallmark is the remarkable observation that the cochlea generates spontaneous otoacoustic emissions (SOAEs), i.e., sounds emitted by the inner ear in absence of any external stimulation, becoming manifest in pressure fluctuations in the ear canal.

In this thesis, we describe how mechanics facilitates the process of sound detection, and we put forward a model that can account for all four hallmarks of the active mechanism. In particular, we provide a possible answer to the question of why and how the cochlea exhibits spontaneous activity. SOAEs exhibit

certain characteristic statistical features captured by our model. The statistics of interest are given by the distribution of SOAE frequencies, the number of SOAEs per cochlea, and the spacing between neighboring SOAEs. Interestingly, it turns out that neighboring emissions exhibit a preferred minimal distance of one semitone.

It is commonly assumed that the production of SOAEs is an epiphenomenon of the active amplification at work. Put differently, SOAEs are thought to possess no direct use and can be considered a footprint of the active nonlinear amplification mechanism with which we can gain further understanding of this process.

In the following chapter, we describe the biology of the cochlea, the mechanical processing of sound stimuli, and the constituents of cochlear mechanics. Pure tone stimuli elicit nonlinear traveling waves of the basilar membrane within the cochlea. We discuss the physics of these waves related to the sound stimuli. Furthermore, we describe active oscillators with which we later model the vertical displacement of the basilar membrane within the cochlea. Additionally, we put this work in context by presenting descriptions of nonlinear waves and previously proposed cochlea models. Finally, we outline the structure of this thesis, providing a guide for the subsequent chapters.

## 1.1 Biophysics of hearing

In this section, we describe the mechanics and the physiology of the human auditory system, which contains a fluid-filled inner ear and is connected via bones and membranes to the gas-filled outer environment. Moreover, we present details about sound processing of the human inner ear on a mechanical level. In particular, we describe amplification properties of the inner ear.

The experimental findings presented here are also valid for most mammals as they resemble each other and share the key structure of the auditory system. Note that, in general, structures and architecture of hearing organs vary broadly between different animal classes and also between animals belonging to the same class [86, 87]. However, the basic unit of sound detection is shared by virtually all species: Hair cells act as mechano-electrical transducers, converting mechanical oscillations into ion flows and consequently into electrical currents which are transmitted to afferent neurons.

### 1.1.1 Physiology of the cochlea and active amplification

The outer part of the ear is composed of the pinna, the concha and the ear canal, see Fig. 1.1. The tympanum separates the outer ear from the middle ear, which consists of a air-filled cavity containing three bones: Hammer, incus, and stapes. These bones transmit vibrations of the tympanic membrane by means of a lever-like motion to the oval window impinging on the inner ear. The middle ear is separated from the inner ear by the oval and round window. The inner ear of mammals is a fluid-filled duct, shaped like a snail shell and well encapsu-

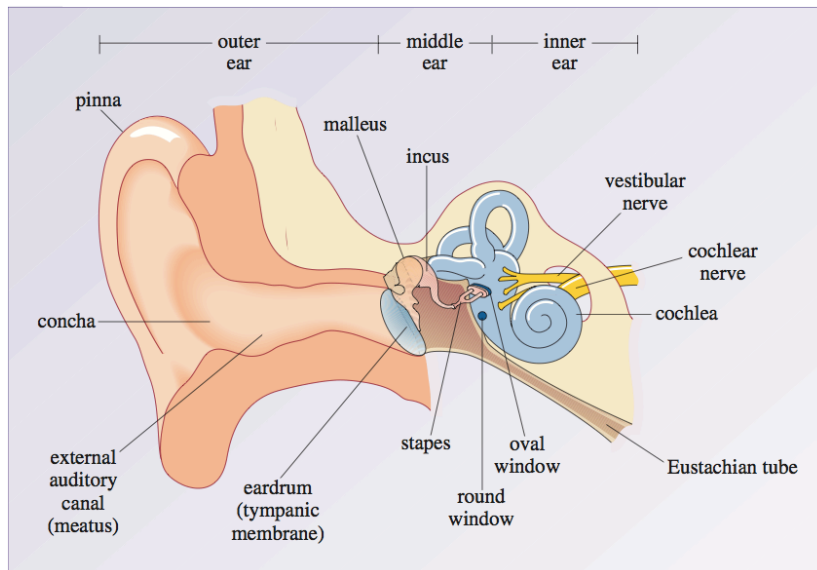


Figure 1.1: **Overview of the ear.** The ear is divided into outer, middle and inner ear, separated by tympanum and oval window. The outer ear consists of the pinna, the concha, and the ear canal. The air-filled middle ear comprises three little bones - the ossicles: Incus, malleus, and stapes, which impinge on the oval window. The Eustachian tube connects the middle ear with the nasopharynx, the back of the nose and upper throat, thus equalizing the pressure on both sides of the tympanum. The fluid-filled inner ear is encapsulated by bone except for the areas of the oval and round window. It contains the organ of balance and the cochlea, the organ of hearing. The vestibular and cochlear nerve transmit electrical pulses to the brain. Graph reproduced with permission of Palgrave Macmillan [5].

lated in one of the hardest bones of the human body, the temporal bone of the skull. It contains the balance and hearing organ, the so-called cochlea, and is connected to the outer world via the middle and outer ear.

The cochlea is a fluid-filled, coiled duct, resembling a snail's shell, of about 10 mm height and 5mm width, and in the uncoiled state it possesses a length of about 35 mm. The cochlea is divided into three chambers in longitudinal direction, which are separated from each other via membranes, as depicted in Fig. 1.2 and Fig. 1.3. Reissner's membrane separates the upper chamber (scala vestibuli) from the middle chamber (scala media), whereas the lower chamber (scala tympani) and the middle chamber are separated by an elastic membrane called basilar membrane (BM) - except for the apical end of the cochlea, where the two channels are connected via a hole in the BM termed helicotrema. The cross-sectional area of the cochlea decreases from base to apex. The upper and

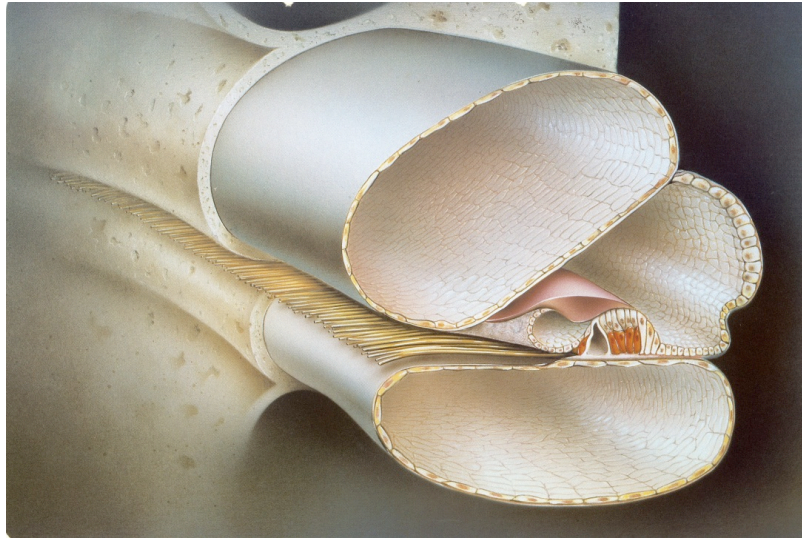


Figure 1.2: **Cross section of the cochlea.** The cochlea is divided into three chambers which are separated by the basilar membrane and the Reissner's membrane. On top of the basilar membrane sits the organ of Corti including the hair cells (marked in red) whose tips are connected to the overlying tectorial membrane. Graph modified from [4].

lower chambers are filled with water-like fluid. In contrast, the middle chamber contains a viscous fluid and several tissues: The organ of Corti, the BM and the tectorial membrane. Due to the viscosity of the fluid in the middle chamber, each cross section of the middle chamber moves essentially as one. The organ of Corti is supported by the BM and contains the key elements of hearing: The outer and inner hair cells together with their protrusions called stereocilia, whose tips are connected to the tectorial membrane. Hair cells act as mechano-electrical transducers, converting mechanical deflections of stereocilia into electrical currents by means of opening ion channels in the stereocilia [57]. The BM and organ of Corti are segmented in longitudinal direction, where each segment contains one inner and three to five outer hair cells. Each of these segments possesses a local best frequency that maximizes the response of the section to external stimulation. This characteristic frequency varies along the cochlea and decreases exponentially from base to apex, locating high eigenfrequencies near the base and low ones on the apical portion. The BM is rather stiff and narrow near the apex and becomes relatively loose and wide near the base.

Sound pressure waves coming from the outer environment enter the pinna, travel through the ear canal and hit the tympanic membrane. From there the ossi-

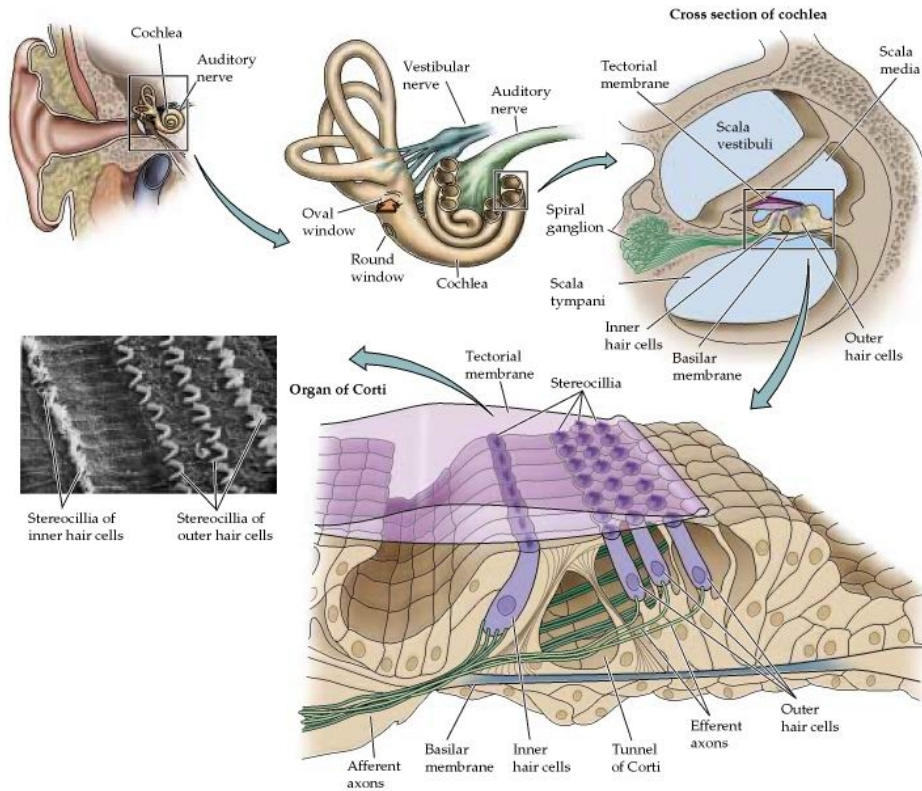


Figure 1.3: **Overview of the cochlea. The subgraphs show an increasingly detailed image of the cochlea and its constituents.** The graph in the upper left corner is an overview of the whole ear. The graph in the middle of the upper row shows the inner ear organ, which consists of the organ of balance and the organ of hearing, together with the vestibular and auditory nerve. In the upper right corner we see a cross section of the cochlear tube, consisting of three chambers with tissues in the middle chamber. The lower right graph depicts a detailed view of these tissues. The basilar membrane supports the hair cells, which are arranged in four rows and whose tips make contact with the tectorial membrane. The graph in the lower left corner displays the regular arrangement of hair cells, organized into one row of inner hair cells and three (to five) "V"- or "W"-shaped outer hair cells. Graph reproduced with permission from [121].

cles transduce the sound vibrations to the oval window, which impinges on the cochlea. Motions of the oval window cause fluctuations in pressure difference between the upper and lower chamber within the cochlea. Movements of the oval window are compensated by opposite movements of the round window, which is located in the lower chamber. In his famous experiments on human cadaver cochleae, Békésy found that a sinusoidal tone elicits a traveling wave on the BM traveling from base to apex [14]. Note that these traveling waves are drastically slower than the sound velocity in water. Vertical oscillations of the BM are directly associated with deflections of stereocilia. The direction of deflections of the stereocilia is perpendicular to the longitudinal axis. Thus, a segment of the BM moving up and down leads to a radial sliding motion of the tectorial membrane relative to both the inner and outer hair cells, and consequently to a deflection of the stereocilia. Hair cells are mechano-electrical transducers, i.e., deflections of the stereocilia result in electrical currents stimulating neurons that are connected to the hair cells. Certain neurons transmit the electrical signal to the neuronal pathway of hearing, finally leading to the sensation of tone perception.

The BM typically contains 15000-16000 hair cells organized in four to six rows: One row of inner hair cells and three to five rows of outer hair cells, with the number of rows increasing towards the apex [116]. Hair cells are innervated by both afferent neurons, which transmit signals towards the central nervous system, and efferent neurons, which carry signals away from the central nervous system. Signal transmission in and between connected neurons is achieved by means of distinct action potentials, each of which is a rapid increase in the electrical membrane potential, followed by a prompt decrease. Thus, action potentials take the form of pulses and are often called spikes. The process of spike emission is termed firing. The average number of spikes per unit time is known as the firing rate.

Inner cells are considered to function mainly as detection units sending signals to the brain. Outer hair cells are thought to function predominantly as amplification units. This is supported by the disparity regarding their innervation: The majority of the slightly more than 30000 afferent neurons present in the cochlea are associated with inner hair cells, whereas efferent neurons are mainly connected to the outer hair cells. However, inner hair cells are sparsely innervated by efferent neurons, and outer hair cells are sparsely innervated by afferent neurons [66].

Each afferent neuron is connected to only one inner hair cell. There are about ten afferent neurons which are connected to each individual inner hair cell. These neurons are typically sensitive to different specific pressure amplitude ranges. Some neurons are receptive to small stimulus intensities; those show a high spontaneous firing rate, and their response to stimuli saturates for medium pressures. In contrast, other neurons show drastically higher pressure thresholds. These neurons have a low spontaneous firing rate, and can exhibit graded responses for stimuli even stronger than 100 decibel (this unit will be

defined in subsection 1.1.3). At each location, the neurons are most susceptible to the characteristic eigenfrequency of the corresponding BM part.

For low frequencies, the neurons fire once per period, whereas at higher stimulus frequencies they fire once every few cycles. However, in both cases, neurons fire at a specific phase of the oscillation for stimulus frequencies up to 4 kHz. This gives rise to a rate coding of the frequency by the neurons. In conclusion, the encoding of sound signals by afferent neurons in the cochlea takes place on a spatial and temporal level, as well as by the individual response patterns of the neurons, i.e., which of the neurons fire.

When Békésy performed his experiments, he was forced to stimulate the cochlea strongly in order to be able to observe a response. This was due to limitations of apparatus sensitivity, but also due to the postmortem state of the probes. However, it "turns out, you hear a lot better when you are alive" (Thomas Duke). Indeed, it has been found that the alive, intact cochlea exhibits an active nonlinear amplification of incoming pressure waves [63]. In particular, the response of the BM to faint signals is substantially more pronounced than what is observed in cadavers. This gave rise to the nowadays commonly accepted paradigm of the 'cochlear amplifier' - an active nonlinear amplification mechanism of the BM response. Small stimuli are amplified, enabling the ear to detect very faint sounds, whereas the amplitude of the BM motion in response to strong stimuli is nonlinearly compressed. This active mechanism is essential for the astonishing properties of the cochlea, outperforming any artificial sound detection system by far, and compressing many orders of magnitude in terms of sound pressure level into few orders of magnitude in output, i.e., magnitude of vertical displacement of the BM. Signatures of this nonlinear process include the distortion product: For simultaneous stimulation with two frequencies  $f_1$  and  $f_2$  ( $f_1 < f_2$ ), the cochlea exhibits a response at the stimulus frequencies but also at a combination tone with frequency  $2f_1 - f_2$ . This would not hold true for a linear system. However, the exact implementation of the physical mechanism and the details of the interplay between its constituents currently remains under debate.

Hair cells display many features associated with this active mechanism, in particular the so-called active hair bundle motility. Hair bundles are not solely passive antennas, but they can generate mechanical work and power deflections of their tips. They exhibit nonlinear amplification, and the hair bundles of some species such as the bull frog or turtle have been shown to frequently oscillate spontaneously [36, 95, 29]. Mammalian hair cells possess the additional property of electromotility, which describes the property of length change of the hair cell in response to a change of the electrical field potential [23]. In the mammalian cochlea, BM and hair cells are intimately related. Vertical movements of the BM are directly related to deflections of stereocilia. Thus, active motion of the BM could well be powered by active hair cells. These observations indicate that hair cells play a vital role in the active nonlinear amplification process and are a possible candidate for the generation of SOAEs.

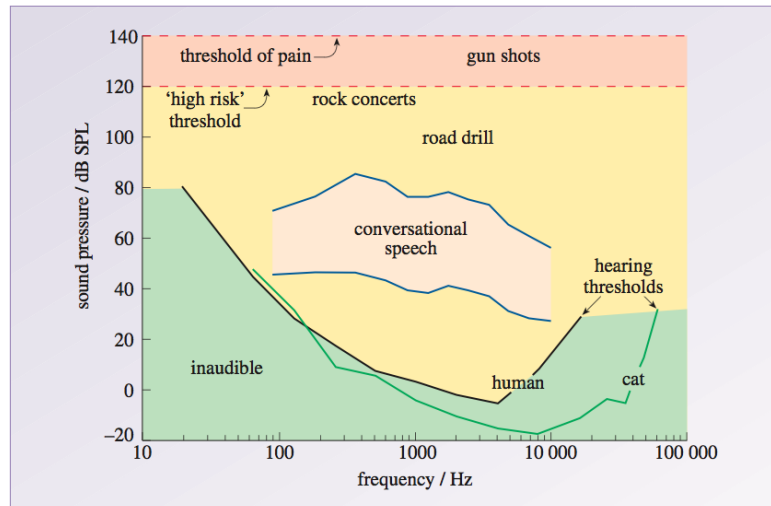


Figure 1.4: **Threshold curves of intact young cochleae of a human and a cat, plotted in dB as a function of frequency.** For selected sound sources such as rock concerts, gun shots, and road drill, the sound pressure level is depicted. 120 dB mark the high risk threshold of damage of the auditory system. The threshold of pain is located at 140 dB. For sounds from human conversation, frequency and dynamic range are plotted. Graph reproduced with permission of Palgrave Macmillan [5].

The range of sounds perceived by the human ear is both a function of frequency and loudness, see Fig. 1.4. The human cochlea is most sensitive to sounds with frequencies around 4 kHz, and becomes increasingly insensitive to both higher and lower frequencies [5]. To be heard, sounds of low frequencies have to be drastically more intense than sounds within the medium frequency range. Note that the threshold curve (black line) is plotted for the range of frequencies that corresponds to the range of characteristic frequencies found on the BM. The threshold curve and perceived frequency range vary significantly between individuals. High frequency thresholds rise with age.

### 1.1.2 Historical overview

Theories of hearing reach back to the time of ancient Egypt and Greece [40]. Due to a lack of experimental data, many theories about the nature of hearing arose [164]. In his book 'Treatise of Man', published in 1662, Descartes put forward one of the first ideas of how hearing might function. He proposed that auditory signals were solely encoded by both their amplitude and their specific time trace of the individual sound. Two centuries later, important discoveries in theory and experiments gave rise to novel approaches and models.

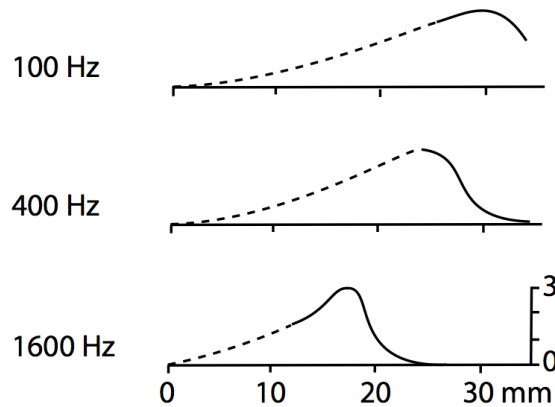


Figure 1.5: **Envelopes of traveling waves in the human post-mortem cochlea elicited by pure tones.** Envelopes of traveling waves in human cadavers as a function of longitudinal position for three different stimulus frequencies. The location of the base and the helicotrema are  $x = 0$  and  $x = 35$  mm, respectively. Adopted from [36], the graph is a reproduction from [15].

By the middle of the 19th century, the Fourier analysis was a well-established technique, and a series of significant experimental investigations were carried out revealing the microscopic structure of the mammalian inner ear [28, 30]. Employing these insights in 1863, H. von Helmholtz made a significant contribution to the research field of hearing by introducing the resonance theory. This framework describes the BM as a strip composed of transverse strings of gradually changing eigenfrequencies, where incoming sound elicits a resonance at a frequency-dependent position [55]. However, this model faced the central problem that fluid damping does not allow for a sharp frequency resolution observed in vivo.

Another substantial contribution was made in 1928. Békésy found in his pioneering experiments from the late 1920s to the 1940s on human postmortem cochleae, for which he earned the Nobel prize, that the cochlea exhibits traveling waves in response to sinusoidal stimulation, see Fig. 1.5 [11, 12, 13, 14]. The response of human cadaver ears to pure tone stimuli is displayed in Fig. 1.5. We see that higher frequencies cause the traveling wave to peak closer to the base. Note that the response is out of the physiological range which is of the order of nanometers. In those experiments, the cochlea responded in a linear manner to stimulation. In 1948, Zwislocki proposed a model, based on established physical principles, which explained experimental evidence well and could account for the linear cochlear responses including the traveling waves, taking into account hydrodynamic interactions of the fluid [163, 164]. As a result, "in the 1950s the function of the cochlea seemed to be understood" [165]. Note that the model proposed by Zwislocki was linear, in accordance with experimental data at that time. By the end of the 1960s, this view was severely challenged as

contrary evidence arose due to novel observation techniques such as the Mössbauer technique. Experiments in 1967 revealed substantially sharper peaks for the maxima of traveling waves in living guinea pigs than what had been observed in experiments by Békésy [62]. Additionally, it was discovered that the location of these maxima depends on the stimulus intensity. In the early 1970s, the finding of increased sharpness was supported by experiments by Rhode on squirrel monkeys, providing evidence for both the physiological vulnerability of the BM and decreasing BM displacement amplitudes after death [127]. Moreover, he discovered that in living cochleae, the BM displacement growth as a function of stimulus intensity exhibits a nonlinear compression [126].

Note that many invasive experiments, and all in living cochleae, are only performed in non-human animals. However, cochleae of humans and other mammals are structurally rather similar. Consequently, experimental findings concerning one species can be inferred to hold true for other species such as humans as well.

By the end of the 1960s, another important step was taken towards the current understanding of cochlear mechanics: The discrepancy between the innervation of inner and out hair cells was discovered. Connections from the cochlea and afferent nerve fibers, which transmit nerve signals to the brain, are predominantly found to innervate inner hair cells, only 5-10% are connected to outer hair cells [141, 142]. This led to the question of the functional role of the outer hair cells. In 1977, inner hair cells were found to be as sharply tuned as nerve fibers [130], implying that no further filtering of the signal between the inner hair cells and the afferent neurons was necessary.

In 1978, Kemp discovered otoacoustic emissions, i.e., sound emissions from the cochlea, caused by external stimulation [67]. One year later, he observed that these emissions are often present even in the absence of any external stimulation [69], the spontaneous otoacoustic emissions were found. The gathered evidence of these discoveries finally led to the notion of active nonlinear cochlear mechanics, and it was commonly accepted that Békésy and Zwislocki had described only the passive cochlea. Remarkably, an active process had been put forward already at the end of the 1940s by Gold [50], proposing that the remedy for the poor frequency resolution in the model by Helmholtz could be an active, electromechanical feedback mechanism, which in case of overcompensation might lead to spontaneous emissions. Gold's contribution was predominantly rejected and discarded until his hypothesis, which resulted from theoretical considerations, was found to be true by the experiments of Kemp 30 years later. An important statistical aspect of spontaneous emissions was discovered in 1983: Adjacent spontaneous emissions exhibit a preferred minimum distance of one semitone, later confirmed by larger studies [135, 31, 131, 146].

In 1985, it was found that unlike inner hair cells, outer hair cells possess somatic electromotility, meaning that their cell bodies change their length in response to electrical stimulation, even up to rather high frequencies [23, 133, 6]. Furthermore, Crawford and Fettiplace discovered that hair bundles can show spontaneous oscillations [29]. This led to the assumption that outer hair cells might be responsible for electromechanical feedback and SOAEs. The observed activ-

ity of the hair bundles was associated with the presence of myosin adaptation motors [56, 76]. Footprints of active mechanics of the ear including SOAEs have also been found in other species such as lizards, fruit flies, toadfishes, guinea pigs, and barn owls. [52, 88, 122, 111, 149].

However, a detailed, exhaustive understanding of the exact biophysical mechanism giving rise to the active amplifications and SOAEs has still not been reached. How nature achieves this, is currently under debate and is an active, vital research topic in the field of the mechanics of hearing [7]. The question of the interplay between somatic motility and active hair-bundle motility is an example of a current subject of research [123, 124, 112].

### 1.1.3 Otoacoustic emissions - measures and models

In this section, we describe ways to quantify and determine otoacoustic emissions. Furthermore, we present models of non-mammalian inner ears which aim at describing spontaneous otoacoustic emissions.

In general, the Fourier transform of a variable  $y$  considered in a time interval  $[0, T]$  is henceforth denoted by " $\tilde{y}$ " and is defined as follows:

$$\tilde{y}(f) = \int_0^T y(t)e^{-2\pi ift} dt. \quad (1.1)$$

The power spectrum of the time trace of  $y$  reads

$$S_y(f) = \frac{\tilde{y}\tilde{y}^*}{T}. \quad (1.2)$$

From the mathematical point of view, these definitions suffice to analyze otoacoustic emissions.

A revolutionary finding was that the inner ear does not only receive acoustical energy provided from the outer environment, but it also actively generates and emits it [118]. These otoacoustic emissions become manifest in sounds detectable in the ear canal either in the presence or, remarkably, even in the absence of external stimuli. There is a variety of different otoacoustic emissions such as stimulus frequency otoacoustic emissions (SFOAEs), which are evoked by pure tones, click evoked otoacoustic emissions, which are transient responses to click stimuli, and spontaneous otoacoustic emissions (SOAEs), which occur in absence of any external stimulation. Click evoked otoacoustic emissions, displayed in Fig. 1.6 A-D, are nowadays routinely employed in hospitals as a noninvasive audiometric test of neonates, who cannot cooperate in conventional hearing tests [70]. From the cochlear response to click stimuli, departures from intact auditory function can be detected. Stimulus frequency otoacoustic emissions measure the cyclo-stationary cochlear response to pure tones at the stimulus frequency. They are of research interest as they exhibit interesting features such as a regular variation of amplitude as a function of stimulation frequency. Furthermore, they are connected to other types of otoacoustic emissions such

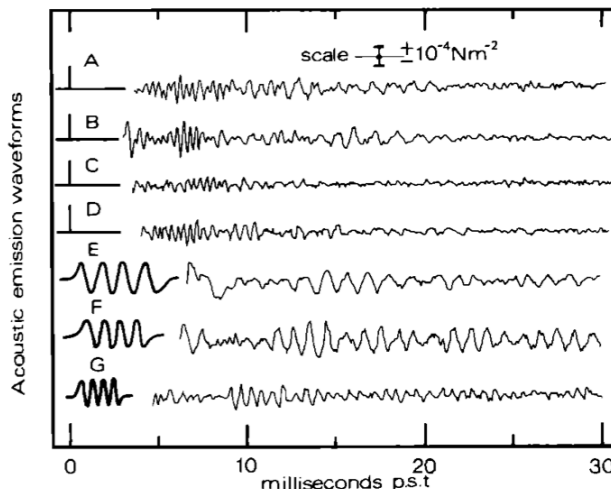


Figure 1.6: **Otoacoustic emission time trace examples of intact young ears.** For each graph A-G we see the pressure in the ear canal as a function of post-stimulus time. A-D show four typical responses to click stimuli. E-G show responses to an excitation with tone burst consisting of a sinusoidal stimulus of cycles with frequencies of 800 Hz (E), 1100 Hz (F), and 1800 Hz (G). Graph adopted from [67].

as SOAEs and to hearing thresholds. Fig. 1.6 E-F displays typical time traces for tone bursts of sinusoidal stimuli of four cycles.

SOAEs, predicted by Gold in 1948 [50] and discovered by Kemp in 1979 [68], are present in the majority of humans. However, they are not a necessary consequence of normal hearing. Typical spectra of SOAEs, as shown in Fig. 1.7 A and B, exhibit a smooth background with discrete, well separated peaks on top. Human SOAEs are remarkably stable. The amplitude of individual SOAEs can vary, but the frequency remains rather stable over decades [47, 24].

In order to detect SOAEs, time traces of pressure fluctuations in the ear canal are measured, and the resulting power spectra are computed. There is as yet no consensus on the optimal detection criterion, as experiments face substantial challenges and diverse noise sources such as line noise [146]. A frequently employed criterion for a peak to count as an emission is that it rises 3 decibel in sound pressure level (dB SPL) above the noise floor [131]. dB SPL or short dB is a logarithmic, relative unit defined by the formula

$$L = 20 \cdot \log_{10} (P/P_{ref}), \quad (1.3)$$

where  $L$  is the level measured in dB,  $P$  is a pressure, and  $P_{ref}$  is a reference pressure, chosen to be  $2 \cdot 10^{-5}$  Pa. By definition, a signal has a sound pressure level of 0 dB if the root mean square value of the signal is equal to  $P_{ref}$ . For a sinusoidal signal, the root mean square is given by the amplitude of the

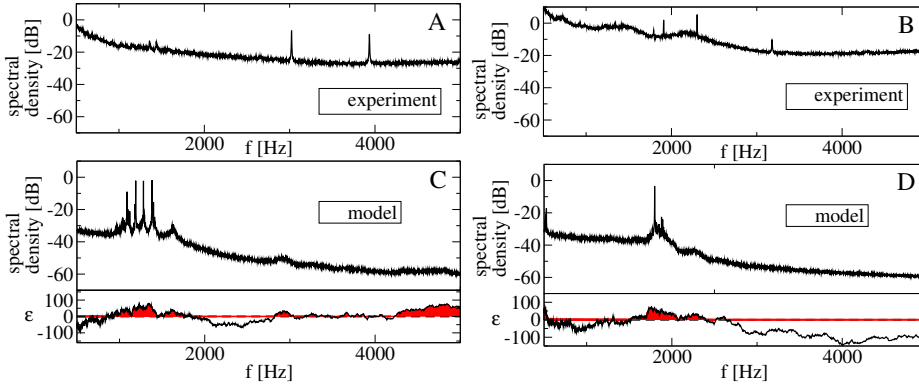


Figure 1.7: **Example of experimental and model power spectra of  $p_e$ .** A, B: Examples of experimental power spectra, with courtesy of Talmadge, panel A published previously [146]. C, D: Upper panel: Typical power spectrum of the model which we will introduce in chapter 4. Parameters corresponding to tables 2.1, 3.1, 4.1. Lower panel: The corresponding bifurcation parameter  $\epsilon(x)$ , which governs the oscillatory activity, plotted as a function of the eigenfrequency  $f(x) = \omega(x)/(2\pi)$ . Red shaded areas indicate frequency regions where the oscillators are active.

signal divided by  $\sqrt{2}$ . Equivalently, one can define  $L = 10 \cdot \log_{10}(S(f)/S_{ref})$ , where  $S(f)$  is the power spectrum at frequency  $f$ , and  $S_{ref}$  is a reference value corresponding to the chosen  $P_{ref}$ .

The logarithmic unit decibel corresponds well to human sound perception which is also logarithmic. More precisely, psychoacoustics has shown that humans perceive a multiplicative increase in sound amplitude as an additive rise in subjective loudness.

Single SOAEs are narrow band emissions of sinusoidal form that can be well described by a self-sustained oscillator subject to white noise [18, 145]. We consider SOAEs as results of stochastic processes. In particular, values of individual SOAE frequencies and distances between neighboring SOAEs are random, but they both follow certain distributions and exhibit specific statistics. In the following, we introduce some statistics of SOAEs, based on experiments by Talmadge, which he generously made available to us [146].

The distribution of the number of SOAEs per ear follows an exponential shape, see Fig. 1.8 A. Up to 32 SOAEs per ear are reported. SOAEs can be detected for up to 8000 Hz and exhibit a bimodal distribution with maxima at 1500 Hz and 3000 Hz, see Fig. 1.8 B. There are extra-cochlear noise sources possibly leading to peaks in the power spectrum of the pressure in the ear canal. However, those noise sources, such as respiration, cardiovascular activity or muscle contractions are of frequencies below 500 Hz. As SOAEs are observed in order to study spontaneous cochlear activity, emissions are considered to be SOAEs only for frequencies above 500 Hz, for which physiological sources can be excluded.

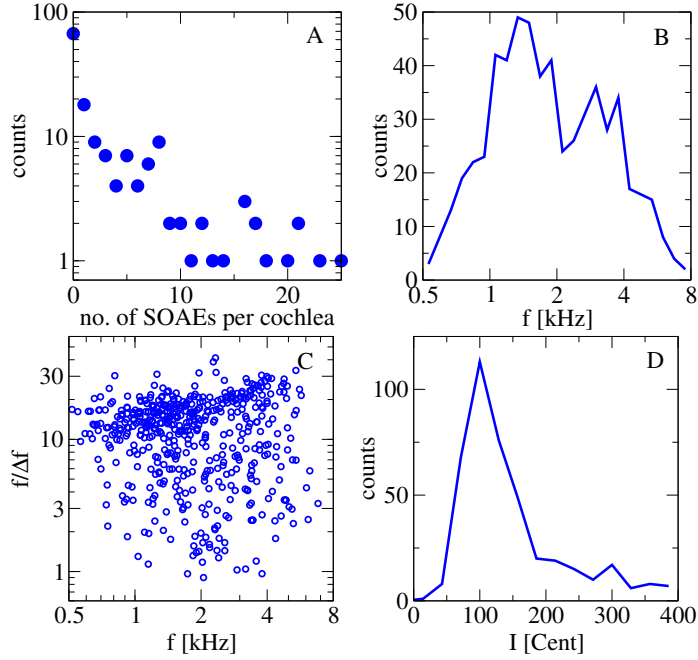


Figure 1.8: **Statistics of SOAE frequency, number of SOAEs per cochlea, and inter-emission frequency intervals in experiment.** Data shown for 152 individual ears in experiment, kindly provided by Talmadge [146]. A: Histogram of SOAE number per cochlea. The average number of SOAEs per cochlea is about 3.9, equivalent to a total count of 588 emissions. B: Count histograms of emission frequency detected. C: Inverse relative frequency intervals  $\frac{\bar{f}}{\Delta f} = \frac{\sqrt{f_1 f_2}}{|f_2 - f_1|}$ , where  $f_1$  and  $f_2$  are frequencies of two adjacent emissions in the spectrum. D: Histogram of relative frequency intervals, given in units of Cent for the same data as in C.

Neighboring SOAEs are not arbitrarily close but possess a regular preferred minimal spacing of roughly one semitone [20]. Two measures of the frequency distance are of particular interest: For two neighboring frequencies  $f_2 > f_1$ , the inverse relative interval is given by

$$\bar{f}/\Delta f = \sqrt{f_1 f_2}/|f_2 - f_1|. \quad (1.4)$$

Expressing the relative distance in units of Cent, we define

$$I(f_2, f_1) = 1200 \cdot \log_2(f_2/f_1). \quad (1.5)$$

The minimal spacing of one-halftone corresponds to exactly 100 Cent and to a value of  $\bar{f}/\Delta f \approx 17$ . The scatterplot of the inverse relative interval as a function of the mean frequency  $\sqrt{f_1 f_2}$  shows a trend from lower values towards higher inverse relative interval values, see Fig. 1.8 C. In Fig. 1.8 D we see the histogram

of the same data as in C, measured in units of Cent. It exhibits a pronounced maximum at 100 Cent and few values smaller than 50 Cent or greater than 200 Cent. Note that both interval measures were employed previously to characterize SOAEs [131, 19, 137]. In chapter 4, we will discuss distances between neighboring emissions in more detail.

The investigation of SOAEs serves as a window through which we can try to gain a further understanding of cochlear mechanics. An understanding of these statistics of SOAEs might shed light on the process of SOAE generation and thus on the cochlear amplifier itself. In chapter 4 we will present a model which incorporates longitudinal coupling and irregularities in the local activity of the individual BM segments. Fitting free parameters associated to the coupling and the irregularities, the model exhibits spontaneous emissions and can account for the above mentioned statistics of SOAEs.

Interestingly, the intriguing finding of a preferred minimal distance between neighboring SOAEs is not solely observable in humans or other mammals: Amongst others species, lizards' inner ears have been found to exhibit such a characteristic spacing as well, together with very robust SOAEs, despite the fact that their inner ear anatomy is strikingly different from mammals' [74]. In particular, the lizard's inner ear organ lacks a frequency-selective BM traveling wave [85, 73, 89, 16], which is a requirement in some model for mammalian SOAEs [161].

Vilfan & Duke [152] described SOAEs and the regular spacing between neighboring SOAEs in lizards by means of longitudinal coupling. In their model, the lizard's inner ear is represented by a chain of Hopf oscillators in the oscillatory regime with a gradually changing eigenfrequency. They were able to show that either purely dissipative or a combination of predominantly elastic plus small dissipative next-nearest neighbor coupling can lead to frequency clustering of the oscillators. Put differently, the chain of oscillators is separated into several groups of oscillators, where all oscillators within one group oscillate with the same frequency. In the following, we refer to these groups as clusters. Clustering leads to a finite number of separated peaks in the power spectrum. The frequency differences between the peaks in the power spectrum correspond to the frequency differences of the average frequencies between the different clusters. Thus, frequency clustering leads to distinct emissions with characteristic inter-emission intervals, thus providing a possible explanation for the characteristic spacing of SOAEs. This idea was employed by H.P. Wit and P. van Dijk to describe a small segment of the mammalian cochlea, coupled only longitudinally, thus neglecting any hydrodynamical interactions [158]. It was shown that this coupling can lead to a spacing of one semitone, as it is observed in humans. We will employ and explain this idea in more detail in chapter 4.

Note that while lizards are the most prominent example of non-mammalian SOAE producing species, there are other species such as mosquitos who also exhibit spontaneous oscillations of hair cells. The hearing organ of the mosquito species *Toxorhynchites brevipalpis* involves only one single antenna. The dy-

namics of the antenna was modeled by D. Avitabile et al. [8], representing it by a stiff rod and describing its deflection by a harmonic oscillator which is coupled to a set of active threads that power oscillations of the antenna. The model can account for key characteristics of antenna dynamics including nonlinear amplification and spontaneous oscillations.

## 1.2 The physics of waves

Waves are a ubiquitous phenomenon, observable as water waves, electromagnetic waves such as light, vibrating strings, pressure waves in the air, traveling cochlear waves, and many more. One way to classify theories of waves is by making the distinction between linear and nonlinear waves. In this section, we describe linear waves in one dimension, as we will treat cochlear hydrodynamics in this way in the consecutive chapter. We present a method of solution, the WKB method, which captures passive cochlear waves well. Furthermore, we introduce theoretical descriptions of nonlinear waves to put our model of nonlinear cochlear waves into context. Finally, we present experimental data, providing evidence that cochlear waves are indeed nonlinear.

Note that we do not define waves or wave equations as there is no consensus in the literature. Consequently, diverse definitions exist, many of which exclude certain interesting cases that are considered to be waves.

### 1.2.1 Linear wave propagation in one dimension

Although in nature most waves are in fact nonlinear, many can be approximated well by means of linear theories, for instance vibrations of strings, electromagnetic radiation in linear media, or acoustic waves of small amplitude. Linear waves are described by linear wave equations, which possess the convenient property that arbitrary superpositions of solutions are again solutions of the same equation. Thus, complex solutions can be decomposed into simple components, for instance by means of Fourier analysis.

For an observable  $z$ , the prototype of the one-dimensional wave equation is given by the partial differential equation

$$\partial_t^2 z = c^2 \partial_x^2 z. \quad (1.6)$$

Here and in the following,  $\partial_t$  and  $\partial_x$  denote the partial derivative with respect to position  $x$  and time  $t$ , respectively. The quantity  $c$  represents the (local) wave propagation velocity, which can be verified below by the form of the solutions of this equation: For constant  $c$  the two independent solutions are given by  $f(x - ct)$  and  $g(x + ct)$  for arbitrary two-times differentiable functions  $f, g$ . The two solutions represent forwards and backwards traveling waves, respectively. Standing waves are defined by the property that they can be separated into a space- and time-dependent part, i.e.,  $f(x, t) = f_1(x)f_2(t)$ .

Note that  $c$  is not necessarily a constant but for instance could be dependent on the location. The hydrodynamic interaction within the cochlea, presented later

in section 2.1, is described by an equation as above with a position-dependent  $c(x)$ . Finding an exact analytical solution for such a space-dependent  $c(x)$  can be intricate. One possible and often surprisingly good approximation is the Wentzel-Kramers-Brillouin (WKB) method, which approximates solutions of linear differential equations whose highest order derivative is multiplied by a small parameter. In order to apply the WKB method to the equation above, we apply the Fourier transformation to Eq. (1.6) with a space-dependent  $c(x)$ :

$$-\omega^2 \tilde{z} = c(x)^2 \frac{d}{dx} \tilde{z}. \quad (1.7)$$

By defining  $Q(x) = 1/\sqrt{c(x)}$  and  $\epsilon = i/\omega$ , the equation above, which is a linear, homogeneous ordinary differential equation of second order, can be written as

$$\epsilon^2 \frac{d^2 z}{dx^2} = Q(x)z. \quad (1.8)$$

The assumptions for the WKB method to work are that  $\epsilon$  is small, and  $Q(x) \neq 0$ . Writing  $z$  as a power of a small quantity, the WKB method gives in first order the approximation [10]

$$z(x) \approx Q(x)^{-1/4} \left( C_1 e^{\gamma(x)} + C_2 e^{-\gamma(x)} \right), \quad \gamma(x) = \frac{1}{\epsilon} \int_{x_0}^x Q(x')^{1/2} dx', \quad (1.9)$$

where  $C_1, C_2$  are two constants. This is the approximation of the solution of the wave equation (1.6) with space-dependent  $c(x)$  and for a single frequency  $\omega$  under consideration. For  $Q(x) > 0$  and  $\epsilon$  purely imaginary, the solution above is written as sum of the forward and reverse traveling wave. The first order approximation does not include reflections except for at the boundaries. Note that even for cases where  $\epsilon$  is not small, the WKB method can yield surprisingly accurate results. It can be used for solving the linear wave equation, as was done in case of the cochlea [41]. Note that the WKB method is a valid approximation for regions outside the nonlinear resonance.

### 1.2.2 Nonlinear waves

Nonlinear waves are described by nonlinear wave equations, implying that the superposition principle does not hold in general. This may lead to emergent structures and makes the finding of solutions considerably more intricate. However, nonlinear wave equations are of great significance as they are employed in many branches of physics to describe numerous nonlinear phenomena, such as earthquakes, traffic flows, shock waves, solitons, or traveling waves in healthy, living cochleae. In the following, we introduce a selection of the broad range of nonlinear wave equation types, all of which come in diverse variants.

A prominent example for a nonlinear wave equation describing solitary water waves [134] is given by the Korteweg-de Vries equation, whose canonical, nondimensional form reads

$$\partial_t h + \partial_x^3 h + 6h \partial_x h = 0. \quad (1.10)$$

One analytical solution takes the form

$$h(x, t) = \frac{c}{2} \operatorname{sech}^2 \left( \frac{\sqrt{c}}{2} (x - ct - x_0) \right), \quad (1.11)$$

describing a wave propagating along the x-direction with velocity  $c$ , where  $x_0$  is an arbitrary constant. The Korteweg-de Vries equation, developed in 1895, can successfully describe experiments such as the first reported observation of solitons (and its succeeding studies) by Russell in 1834, who observed a solitary wave traveling along a canal. One of the predictions of the Korteweg-de Vries system is that higher waves travel faster, visible in the dimensionless solution above as the height is given by half its velocity. This is in accordance with experimental observations by Russell. Although the Korteweg-de Vries equation was mostly forgotten, it was rediscovered decades later in a different context: It was derived as the continuum limit of the Fermi-Pasta-Ulam system modeling both nonlinear beaded strings and one-dimensional crystals. Furthermore, Korteweg-de Vries type equations are applied in plasma physics and for the description of shock waves [151].

The Boussinesq equation, a typical variant of which reads

$$\partial_t^2 h - \partial_x^2 h + 3h\partial_x^2 h + \alpha\partial_x^4 h = 0, \quad (1.12)$$

admits the solution [1]

$$h(x, t) = \frac{1}{6} (1 + 8k^2 - c^2) - 2k^2 \tanh^2 (k(x + ct)), \quad (1.13)$$

where  $k$  and  $c$  denote the wavenumber and speed, respectively. The Boussinesq equation is applied to describe similar phenomena as the Korteweg-de Vries equation and can be employed to model surface motion of shallow water waves including tsunamis, which can be considered waves in shallow water due to their long wavelength compared to the ocean depth.

Another major example of a nonlinear partial differential equation is given by the FitzHugh-Nagumo equation, which is a simplified version of the Hodgkin-Huxley model for the axon membrane potential dynamics in a spiking neuron. The FitzHugh-Nagumo equation is known to describe traveling wave fronts in excitable media such as nerve fibers [53]. The related Nagumo equation

$$\partial_t h = D\partial_x^2 h + h(1 - h)(h - a), \quad (1.14)$$

where  $a \in [0, 1]$ , and  $D > 0$ , exhibits the analytical traveling wave solution

$$h(x, t) = \left( 1 + \exp \left[ x/\sqrt{2D} + t \left( a - \frac{1}{2} \right) \right] \right)^{-1}. \quad (1.15)$$

The Nagumo equation is a model for active pulse transmission, employed amongst others in circuit theory and in biology [26].

Lastly, we present the Swift-Hohenberg equation, which is widely used in modern science to describe pattern formation in both simple and complex fluids, neural tissues, optical physics, etc. One variant including dispersion is given by the equation [79]

$$\partial_t h + 2\partial_x^2 h + \partial_x^4 h - \sigma \partial_x^3 h = \alpha h + \beta h^2 - \gamma h^3 \quad (1.16)$$

for parameters  $\sigma, \alpha, \beta$  and  $\gamma$ . It was found that in case of  $\sigma \neq 0$  there exist (non-stationary) traveling waves. Furthermore, variants of the Swift-Hohenberg equation were shown to admit soliton solutions as well [96].

Turning towards cochlear waves,  $h$  henceforth denotes the vertical displacement of the BM. The wave equation for  $h$ , which we employ in this thesis for the description of nonlinear cochlear waves, can be written as

$$\partial_t^2 h = \partial_x^2 [\gamma_1 \partial_t z + \gamma_2 z + \gamma_3 \partial_x^2 z + \gamma_4 |z|^2 z], \quad (1.17)$$

where  $z$  is a complex variable with real part  $h$ , and  $\gamma_1, \gamma_2, \gamma_3, \gamma_4$  are complex parameters. The values of  $\gamma_1, \gamma_2$  and  $\gamma_3$  are constant, in contrast to the space-dependent coefficient  $\gamma_2$  which leads to a space-dependent traveling wave propagation velocity. The equation above arises from a linear hydrodynamic equation, which relates the pressure within the cochlea to the vertical BM deflection  $h$ , in combination with longitudinal coupling and nonlinear local oscillator dynamics describing the motion of a single element given by the Hopf normal form, where the single element represents a small segment of the BM. No analytic solution is known for this equation or its frequency domain representation, even in the linear case with  $\gamma_4 = 0$ . In this thesis, the equation is solved numerically in the presence of dynamical white Gaussian noise. Note that the formulation of the equation above is not optimal for the numerical integration. Thus, we choose a different form, which will be described in chapter 2.

From the experimental data displayed in Fig. 1.9 A, one can conclude that cochlear waves are indeed nonlinear as the superposition principle does not hold true. Envelopes of traveling waves in the living guinea pig cochlea are shown, caused by pure tone stimulations of 15 kHz and various strengths ranging from 15 to 100 dB. The relation between input and BM displacement is approximately linear near the base, corresponding to small  $x$  values. In contrast, for locations in the vicinity of the characteristic frequency corresponding to the peak region of the waves, a sublinear growth of the maximal displacement as a function of stimulus intensity is visible. This indicates a compressive nonlinearity. It is evident that the waves alter their shape and become broader for increasing input amplitudes. Note that, in general, maxima also shift to the basal part for stronger stimuli.

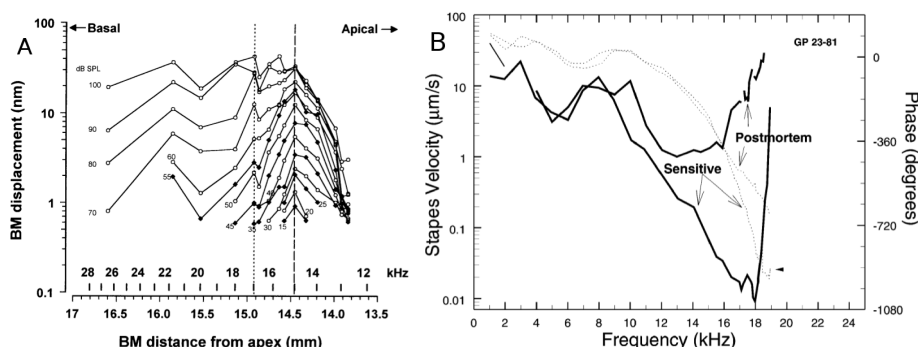


Figure 1.9: **Pure tone responses of the guinea pig cochlea.** A: The BM displacement for pure tones of  $f = 15$  kHz with different stimulus strengths is plotted as a function of position along the cochlea in living guinea pigs [132]. The second horizontal axis denotes the best frequency of the location of the BM associated with its position. B: The effect of death on the cochlear response to pure tones. The black solid curves denote the magnitude of the response of the cochlea presented as isovelocity mechanical tuning curve for a fixed portion of the BM as a function of stimulus frequency, i.e., the magnitude of the stapes velocity is plotted for which the considered portion of the BM, which is located in the basal turn, oscillates with a velocity of  $50 \mu\text{m/s}$  for varied frequencies. The solid lines denote the magnitude of the response of the living and dead cochlea, respectively. The dashed lines indicate the phase of the BM response relative to the stapes. Data from [109], presented in the reprinted version of [129].

Fig. 1.9 B illustrates the difference between the ante- and post-mortem organ. Isovelocity curves for a specific portion of the cochlea are plotted as a function of driving frequency. The graph shows the velocity with which the stapes have to be driven to attain a fixed BM velocity of  $50 \mu\text{m/s}$  for the BM part under consideration. The solid lines denote the magnitude of the stapes velocity, and the dashed lines represent the phase of the BM oscillation relative to the stapes. Both lines are given for both the living and dead specimen. It is apparent that in the post-mortem state, the cochlea must be driven significantly stronger to elicit the same velocity response, indicating that the active amplification mechanism has deteriorated or vanished. The relative phase of BM and stapes seems basically unaffected by death.

### 1.3 Active oscillators

In this section, we describe properties of active oscillators and transitions leading to self-sustained oscillations. Active oscillators are highly relevant in the field of mechanics of hearing, as both hair bundle and BM dynamics have been well captured in the framework of active oscillators. We also employ active os-

cillators as vital elements in the model of SOAEs which we present in this thesis.

Dynamical systems with an observable  $x(t)$  can exhibit qualitatively very different dynamics. Active oscillators are physical systems that possess a power source, which enables them to overcome damping and to oscillate spontaneously. Thus, active oscillators can exhibit self-sustained spontaneous oscillations, finally arriving at a cyclo-stationary state, which makes them qualitatively different from passive oscillators whose amplitude of oscillations decay over time in presence of damping [42]. Active oscillators can be used to describe persistent oscillations in the absence of external periodic stimulation, such as the heart beat, circadian rhythms, oscillating chemical reactions, and spontaneously oscillating hair bundles [144, 114]. Physical realizations of active oscillators can be constructed for instance by including nonlinear damping (the van der Pol oscillator is a prominent example for such an oscillator), nonlinear stiffness, or time-delayed feedback [42].

Suppose a dynamical system can be described by a single control parameter  $C$  which governs the internal state of the system. A continuous variation of this parameter may lead to abrupt qualitative changes of the dynamical system. If by variation of  $C$ , fixed points of the dynamical system vanish, emerge or lose their stability, these qualitative changes are termed bifurcations. The values of  $C$  at which they occur are called bifurcation points. A particularly interesting case arises if an oscillator is passive for control parameter values  $C < C_{crit}$  and active for  $C > C_{crit}$ , where  $C_{crit}$  is the critical value. This will be discussed in the following subsection.

### 1.3.1 Hopf bifurcation

Consider a two-dimensional dynamical system with a stable fixed point to which the perturbed systems returns by means of exponentially damped oscillations. The stability of the fixed point is equivalent to negative real parts of both eigenvalues of the system's Jacobian. If for a variation of  $C$ , both eigenvalues cross the imaginary axis simultaneously into the right half of the complex plane at a critical parameter value  $C_{crit}$ , the system is said to undergo a Hopf bifurcation. Thus, the fixed point loses its stability. If by transversing the critical point a stable limit cycle arises, the bifurcation is termed supercritical Hopf bifurcation [144]. In the following, we focus only on this case, and we will refer to it as Hopf bifurcation. However, note that there is also a subcritical Hopf bifurcation. To summarize, a Hopf bifurcation is given if a fixed point of a dynamical system loses stability and gives birth to a limit cycle, with the dynamical system undergoing a transition from a passive to an active oscillator.

It can be shown that regardless of the specific details of the dynamical system, all systems in the proximity of a Hopf bifurcation share certain generic properties which are due to the characteristics of this bifurcation.

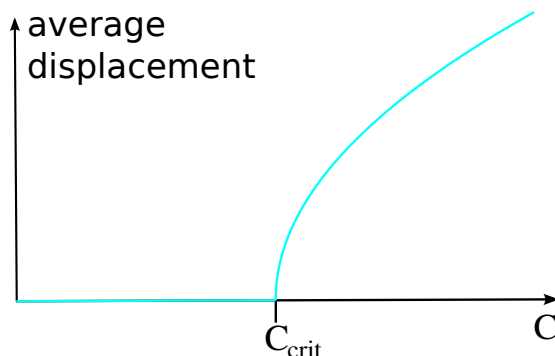


Figure 1.10: **Average size of spontaneous limit cycle oscillations in vicinity of a supercritical Hopf bifurcation as function of the control parameter  $C$ .** Sketch of the average displacement of an oscillator in the (cyclo-)stationary state near a supercritical Hopf bifurcation, plotted as a function of the control parameter  $C$ .  $C_{crit}$  is the critical point. For values  $C < C_{crit}$ , the system is stable and a perturbed system returns to its equilibrium. In the oscillatory regime,  $C > C_{crit}$ , the equilibrium becomes unstable and the perturbed system performs limit cycle oscillations of amplitude  $|x_1| \sim \sqrt{C - C_{crit}}$ .

For an arbitrary system close to a Hopf bifurcation with state variable  $x(t) = \sum_{n \in \mathbb{N}} x_n e^{in\omega t}$ , the response to a periodic driving  $f(t) = f_1 e^{i\omega t} + f_{-1} e^{-i\omega t}$  in the cyclo-stationary state can be approximated as

$$f_1 = \mathcal{A}x_1 + \mathcal{B}|x_1|^2 x_1, \quad (1.18)$$

where  $\mathcal{A}$  and  $\mathcal{B}$  are complex coefficients depending on  $\omega$  and the control parameter [25]. Note that no quadratic terms are present. If the system is at its critical point and is driven with its resonance frequency, the linear terms vanishes, i.e.,  $\mathcal{A} = 0$  holds.

After a possibly nonlinear transformation of variables, each system can be described by the so-called Hopf normal form

$$\frac{dz}{dt} = (\epsilon + i\omega_0)z + (a + ib)|z|^2 z + \mathcal{O}(|z|^5), \quad (1.19)$$

where  $z$  is the complex state variable,  $\epsilon$  is the bifurcation parameter, which determines the stability of the system, and  $a, b$  are real coefficients [157]. Note that we consider only the supercritical Hopf bifurcation. In the subcritical case, there would be a term of 5th order that might be non-negligible. For the above equation,  $\epsilon = 0$  is the critical point. For  $\epsilon < 0$  the system behaves as a passive oscillator with a stable fixed point at the origin, and oscillations decay with the rate  $|\epsilon|$ . For  $\epsilon > 0$  the fixed point becomes unstable, and the system becomes an active oscillator exhibiting limit-cycle oscillations, see Fig. 1.10. Of special interest is the case of the system posed exactly at  $\epsilon = 0$ , where the oscillator is termed critical and exhibits a pronounced nonlinear behavior.

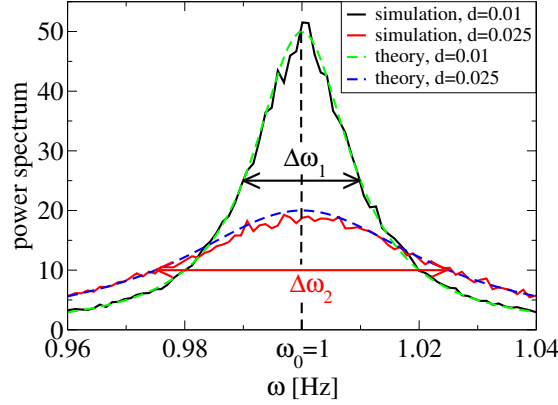


Figure 1.11: **Spontaneous power spectra of the noisy Hopf oscillator.** Spontaneous power spectra of the real part of  $z$  of the Hopf oscillator driven by white noise for medium noise strength  $d = 0.025$  obtained by simulation (red line) and theoretical predictions (blue line), and for weak noise strength  $d = 0.01$  (simulation result represented by black line, theoretical prediction marked green). The medium and weak noise lead to peak widths  $\Delta\omega_1 = 0.02$  Hz and  $\Delta\omega_2 = 0.05$  Hz, respectively. The corresponding quality factors are  $Q_1 = 50$  and  $Q_2 = 20$ , respectively. Parameter values are given by  $\epsilon = 1$ ,  $\omega_0 = 1$ ,  $a = -1$ , and  $b = 0$ . The theoretical calculations are according to Eq. (1.21).

Applications of the Hopf oscillator include the description of hair bundle dynamics, which we discuss in more detail in the next section [35, 93, 94, 114]. Furthermore, the mammalian hearing system shares many key features with a system close to a Hopf bifurcation, such as a sharp frequency selectivity, an extreme sensitivity detecting small signals, and a wide dynamic range [25, 41].

### 1.3.2 Noisy oscillators

In this subsection, we turn towards the interesting case of the normal form endowed with a noise source. We investigate the Hopf oscillator subject to additive white noise, which we will use later in this thesis to model the dynamics of the BM subject to diverse noise sources.

The equation for the dynamics of a single stochastic Hopf oscillator in the time domain subject to additive white Gaussian noise reads

$$\frac{dz}{dt} = (\epsilon + i\omega_0)z + (a + ib)|z|^2z + \xi, \quad (1.20)$$

where the strength of the noise  $\xi$  is given by  $d$ . The dynamics of the stochastic Hopf oscillator can be well captured by a theoretical description under the condition of weak noise [54, 65].

In the oscillatory regime, i.e. for  $\epsilon > 0$ , and for a purely real nonlinearity by setting  $b = 0$ , the power spectrum of the real part of  $z$  is a Lorentzian and can be approximated by

$$S(\omega) = \frac{\epsilon^2}{2da^2} \left( 1 + \frac{\epsilon^2}{d^2a^2} (\omega_0 - \omega)^2 \right)^{-1}. \quad (1.21)$$

It is apparent from the formula that the noise intensity  $d$  and the bifurcation parameter  $\epsilon$  shape the power spectrum. An increase in  $\epsilon$  results in a more pronounced peak in the power spectrum, whereas for stronger  $d$  the maximal value of the peak decreases and the peak broadens, see Fig. 1.11. Note that the integral over the peak, i.e., the power of the emission, is independent of the noise intensity.

For a peak in the power spectrum, the quality factor  $Q$  is defined to be the ratio of its center frequency and its full width at the half-maximum magnitude, i.e.,  $Q = \frac{\omega}{\Delta\omega}$ , and in the theoretical approximation we have  $Q = \omega\epsilon/(2d|a|)$ . Thus, the formula predicts an inverse proportionality of noise strength and quality factor, which corresponds well to simulation results, see Fig. 1.11.

Hair bundle dynamics can be well described in the framework of stochastic Hopf oscillators [80, 101, 102]. The active regime of the Hopf oscillator describes spontaneously oscillating hair bundles which in case of the bull frog are observed frequently. The stochasticity stems from various sources such as thermal motion of the surrounding fluid, stochastic opening and closing of ion channels, and stochasticity due to internal myosin motors, which have also been associated with the activity of the hair bundle [36, 101].

Studies have shown that hair bundles contribute significantly to our ability to hear and are thought to be a key component. However, their mechanical response properties, in particular the gain, are worse than what is observed for the entire auditory organ in experiments. This might be due to the noise hair bundles are exposed to. The question is how the ear achieves its performance despite a limited performance of its single constituents. It turns out that elastic coupling of hair bundles might reduce the influence of noise. Indeed, it was shown coupling of hair-bundle models leads to an effective noise reduction [36]. Furthermore, for Hopf oscillators exposed to noise, a reduction of noise leads to improved amplification properties.

## 1.4 Models of the mammalian cochlea

In this section, we discuss a selection of models describing mammalian cochleae in order to place the model of this thesis in context. We outline both linear and nonlinear models, focusing on one-dimensional models. In particular, we present models which can account for spontaneous activity of the cochlea resulting in SOAEs.

The mammalian cochlea is the subject of extensive research and has been described by numerous structurally different models. The scale of complexity of

the models varies significantly: Some models aim at describing the cochlea as realistically as possible, using a three-dimensional representation of the cochlear geometry, for instance models developed by the group of Karl Grosh [99]. Others prefer to use a slight reduction of complexity and use two-dimensional representations. Many models use a one dimensional hydrodynamic approach which is able to capture essential characteristics of cochlea behavior (which is related to their property of the so-called critical layer absorption [81, 2]). Here, dimensionality is understood to apply to the description of the pressure within the cochlea. Put differently, in a one-dimensional hydrodynamic representation, the pressure within a cross section of the cochlea is uniform.

### 1.4.1 Linear models

Prior to the early 1970s, the mechanics of the cochlea was believed to be linear. Consequently, early models were linear as well. This includes one of the first significant contributions to this field, the theory of local resonators suggested by Helmholtz in 1863 [55]. He introduced a model with a tonotopic structure, i.e., an exponential position-best frequency map acting as a form of spatial Fourier transform. In a nutshell, Helmholtz neglected hydrodynamic interactions, which arise due to the fluid motion, and he described the BM as a strip composed of parallel transverse fibers which can passively resonate with a gradually changing frequency along the BM in response to sound stimulation. Assuming negligible tension in longitudinal direction, Helmholtz' theory of the cochlea is described by a chain of harmonic oscillators with varying eigenfrequencies.

At the end of the 1940s, Zwislocki developed a model which was the first to account for the body of empirical evidence present at that time, provided mainly by experiments carried out by Békésy [163, 164, 11, 12, 13]. Zwislocki's one-dimensional model included equations resulting from hydrodynamic interactions, which amongst others employed force balance and conservation of fluid volume. These equations governing hydrodynamics are still widely used in one-dimensional models up to date. Assuming a linear relation between the pressure difference (between the upper and lower chamber) and the vertical BM deflection governed by an exponentially varying stiffness, the model can account for traveling waves in response to periodic stimulation.

Since the discovery of the inherent nonlinearity of the living, intact cochlea at the end of the 1960s, linear models or linear variants of models serve mainly the purpose of eliciting certain functioning principles or are designed to describe cochlear function for small stimulus amplitudes, rather than explaining the entire cochlear mechanics.

In 1993, Mammano and Nobili represented the cochlea by means of a one-dimensional linear model in the frequency domain, describing the BM as a continuum. In their model, the BM dynamics of a small BM segment is modeled by a harmonic oscillator with shearing resistance, driven by forces which describe the actions generated by the motion of both the stapes and the entire organ of Corti. These forces are transferred simultaneously by the fluid to the BM [84]. Longitudinal elastic coupling is neglected in this model. In the first part

of the paper, the cochlea is described by means of a passive model with damped oscillators as described above. An active version of the model is also presented. It is an extension of the passive model, introducing an undamping term which stems from outer hair cell considerations and does not overcompensate for the present damping. The model can account for traveling waves and describes the cochlear response to pure tone stimulations with low pressure. However, it cannot account for nonlinearities, for instance those being present at stimulations with higher intensities.

In 2003, Wen and Boahen introduced a two-dimensional linear cochlear model with active bidirectional coupling [155]. The model also takes into account active forces generated by the outer hair cells. The bidirectional longitudinal coupling, through which each segment receives feedback and feedforward, is justified by the presence of specific architectural components observed in the organ of Corti, namely Deiter's cells and phalangeal processes, connecting neighboring segments in longitudinal direction. The model can account for a large amplification and a sharp tuning. However, it is yet unclear if these physiological structures serve the function they are used for in the model.

### 1.4.2 Nonlinear models

The class of nonlinear models is quite large, containing a broad range of different approaches. Here, we present a selection of different important models, focusing mainly on one-dimensional frameworks, to put the description which we propose in this thesis into context.

In the 1990s, Talmadge and collaborators proposed an active nonlinear model in the time domain, which employs a one-dimensional approach [147, 148]. Time-delayed stiffness plus inhomogeneities in the frequency gradient along the cochlea is the mechanism which is used to account for SOAEs. The BM is modeled as a one-dimensional chain of van der Pol-type oscillators which are equipped with time-delayed stiffness [160] and coupled to their neighbors via hydrodynamic interactions. The time-delayed stiffness in this model comes in combination of a slow and fast time delay, where the latter acts as power source by effectively introducing negative damping. A passive harmonic oscillator is placed at the basal end to describe the middle ear. The two model types presented in the two papers [147, 148] differ slightly but share the main features. This model can produce SOAEs. The model variant in [147] is reported to exhibit a spacing distribution with a maximum at one semitone, as observed in humans. However, no statistics are shown. Although the system was observed to reach a steady state, SOAE were not necessarily reaching a stable emission frequency. Note that it cannot be determined where SOAEs occur in this model before the simulation is carried out.

A similar approach was taken by Epp et al. [45], which is based amongst others on the model above [97, 148]. Epp et al. described the cochlea by means of a one-dimensional model in the time domain, where the local oscillator dynamics are determined by a differential equation corresponding to a harmonic oscilla-

tor with a specific, partially negative, damping profile and a delayed feedback stiffness. The model can account for different aspects of otoacoustic emissions including SOAEs and their regular spacings of roughly 100 Cent equivalent to one semitone. However, no statistics of the emissions were computed.

Duifhuis described the cochlea by a one-dimensional model consisting of a chain of hydrodynamically coupled van der Pol or van der Pol-type oscillators with specific damping functions [40]. This setup might be able to account for SOAEs. However, SOAEs of the model are not presented [40].

In 2003, Kern proposed a one-dimensional model of the cochlea using coupled Hopf oscillators in the stable regime as basic units to describe cochlear dynamics and BM responses. The hydrodynamics are described by means of equations resulting from water surface wave and energy density considerations [72]. Extensions of this model are also considered, including active oscillators equipped with a feedforward mechanism [71]. Although this model might be able to account for SOAEs, they are not examined in this work.

A model of a small section of the cochlea was considered by Wit and van Dijk [158] to explain the preferred distance of SOAEs in humans. They described a small portion of the BM by a chain of Hopf oscillators coupled solely by means of dissipative and elastic coupling, thus neglecting hydrodynamic interactions and employing the idea presented by Vilfan and Duke [152]. They were able to show that longitudinal coupling can lead to cluster formation, where oscillators within one cluster oscillate with a common frequency, which results in a minimal distance between neighboring SOAEs.

Another one-dimensional model of the cochlea, describing it also by means of a chain of Hopf oscillators, was developed by Liu et al. [82]. The chosen setup is similar to the one presented by Vilfan and Duke. However, oscillators are coupled in a solely dissipative manner, thus neglecting hydrodynamic interactions. Responses to pure tone stimulation are presented where the stimulus acts in the same manner on each individual oscillator. The case of SOAEs is not considered. The assumption of considering only dissipative coupling and neglecting elastic coupling and hydrodynamic interaction seems controversial. Moreover, the global action of the stimulus does not correspond to experiments, where the stimulation only acts via the oval window.

In 2006, Wen extended the linear model outlined in the previous section, introducing a nonlinearity by incorporating a saturating outer hair cell force [156]. It was hereby assumed that this is the main source of the cochlear nonlinearity. The model responses are comparable to experimental data.

A two-dimensional model of the cochlea in the frequency domain was put forward Neely and Kim [106, 107], modeling local dynamics of each segment of the cochlea by means of two degrees of freedom. Put differently, cochlear micro-mechanics are described by an array of mass-spring-damper systems, where one mass represents the tectorial membrane, and the other mass models the BM. The two masses are connected to rigid walls and to each other via springs and dampers, as sketched in Fig. 1.12. The active mechanism is incorporated by including a feedback loop with an active pressure source acting on the second

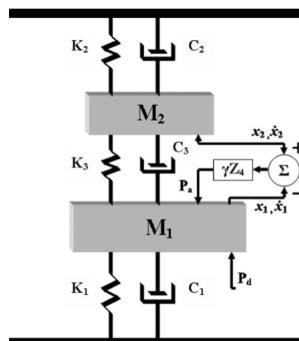


Figure 1.12: **Sketch of the cochlear micro-mechanics model with two degrees of freedom.** The graph depicts the micro-mechanical description which was employed by Neely, Kim, Elliott, Ku, and Lineton. Two masses  $M_1, M_2$  with vertical coordinates  $x_1, x_2$  are connected to rigid walls and to each other by means of springs and dampers, indicated by  $K_i$  and  $C_i$ , respectively ( $i = 1, 2, 3$ ). The tectorial membrane and the BM are represented by  $M_1$  and  $M_2$ , respectively. The system contains a feedback loop of strength  $\gamma$ , implemented by means of an active pressure source  $P_a$ . The BM, i.e.  $M_1$ , is driven by  $P_a$  and  $P_d$ , the pressure difference between the scala tympani and scala vestibuli. Graph adopted from [44].

mass. The BM is driven by both the active pressure and the pressure difference between the upper and lower chamber of the BM. Note that many parameters are fitted to match measured responses [106]. The macro-mechanics are described by the hydrodynamic equation put forward in earlier models [164, 81]. The parameters of this model were adjusted to describe the cat cochlea for which there was more experimental data available.

Later the model was formulated in the time domain, and parameters were adjusted to describe the human cochlea [44, 77, 78]. Ku, Elliott and Lineton employed the idea of Neely and Kim to obtain statistics of SOAEs [77, 78]. For a model variant without stabilizing nonlinearity, instabilities were introduced by static inhomogeneities in the feedback gain along the cochlea. Statistics of the resulting instabilities were investigated. More precisely, histograms of frequencies of occurring instabilities and relative frequency differences between neighboring instabilities were calculated. The model can account for the preferred minimal distance of  $\sqrt{f_1 f_2} / |f_2 - f_1| \approx 15$ , given two neighboring SOAEs at frequencies  $f_1$  and  $f_2$ , observed in experiments. The frequencies of instabilities of the model range from 1 or 2 up to 20 kHz in contrast to a restricted range of 0.5 to 6 or 8 kHz in experiments. The statistics of the number of emissions per cochlea are not shown.

The modified model incorporates a saturating nonlinearity which turns linear instabilities into limit cycle oscillations [78]. Some parameters of the model are also altered. The resulting model can account for the trend in the inverse

relative frequency spacing  $\sqrt{f_1 f_2}/|f_2 - f_1|$  towards higher values for rising frequencies, which is observed in experiments.

Apart from the descriptions presented above, there are numerous other passive or active models [33, 34, 75, 81, 159]. Furthermore, there exist detailed three-dimensional representation of the cochlea [49], or physical models that were actually manufactured in reality [27].

While existing models presented above may provide interesting insights and can account for certain features, many of them lack simplicity and are not generic: Some descriptions have to make specific assumptions such as time-delayed stiffness or feedforward mechanisms whose existence is hypothesized but not experimentally verified, others employ two- or three-dimensional approaches.

For the majority of the models, no statistics of SOAEs were presented. Furthermore, there is no model which can account for the whole body of statistics that has been observed in experiments. In the following chapters, we introduce a generic model of the human cochlea which can account for all the four hallmarks of human hearing. In particular, the model can account for SOAEs and their main statistics.

## 1.5 Organization of the thesis

In chapter 2 we introduce a simple and generic model of the active nonlinear cochlea in the time domain, employing a one-dimensional approach consisting of a chain of hydrodynamically coupled critical Hopf oscillators. This model corresponds to and extends a previous description formulated in the frequency domain [41]. To introduce this model, we discuss hydrodynamic interactions within the cochlea and model the local oscillator dynamics of the BM. Furthermore, we describe how to integrate this model forward in time and investigate how this model relates to the previously proposed model in the frequency domain. Finally, we determine incoming and outgoing waves for this model.

Subsequently, we present a more biophysical description in chapter 3, introducing a boundary condition, which represents the middle ear, and elastic as well as dissipative longitudinal coupling between neighboring oscillators. This provides a setup where all otoacoustic emissions are well defined and can be studied more easily than in the setup of chapter 2. We study SFOAEs and spontaneous activity, finding strong numerical evidence that only disorder in the bifurcation parameter leads to SOAEs. In particular, disorder in the frequency gradient enlarges some peaks slightly, but it does not suffice to elicit pronounced SOAEs.

In chapter 4, we exploit these findings and investigate SOAEs in more detail. We model the bifurcation parameter as essentially critical but with small static (time-independent) irregularities that are correlated in space. These irregularities lend individuality to each realization of the model cochlea. Furthermore, we employ elastic and dissipative longitudinal coupling to obtain clusters of syn-

---

chronized oscillators and thus a separation of neighboring SOAEs as observed in experiments. The resulting model contains free parameters: The strength of the dynamical noise, the elastic and dissipative longitudinal coupling, and the standard deviation as well as the correlation length of the irregularities in the bifurcation parameter. The dynamical noise is mainly used for regularization purposes. We fit the remaining free parameters in order to match statistics of experimental SOAEs, which are given by the frequency range of SOAEs, the number of SOAEs per realization, and the inverse relative distance between neighboring SOAEs. Finally, we discuss the noiseless system as well as some of its variants. These include a) the model with a negative mean bifurcation parameter, which leads to a more realistic shape of the distribution of the number of SOAEs per realization, and b) the system subjected to global phase noise, which results in realistic widths of SOAEs.

We conclude this thesis by summarizing the results in chapter 5, presenting an outlook on possible future investigations, and explaining how to test the model and its predictions. Put differently, we address open questions and possible ways to extend and test the description introduced in this dissertation.

## Chapter 2

# Simple model for nonlinear waves in the cochlea

In this chapter, we introduce a simple and generic one-dimensional model in the time domain of the active nonlinear behavior of the cochlea. The BM dynamics is described by a chain of critical oscillators coupled via hydrodynamic interactions. Although this model is generic and one-dimensional, it can account for many key features of the auditory system without suffering from instabilities or making detailed assumptions. The cochlea model reproduces the experimentally observed extreme sensitivity, wide dynamic range and sharp frequency selectivity, and it can account qualitatively and quantitatively for traveling waves [41, 64]. We derive the model equations and demonstrate how the model can be simulated forward in time. Furthermore, we put the simple model in the context of other descriptions of the cochlea by demonstrating that it extends a previous model put forward in the frequency domain [41]. Additionally, we investigate the low frequency modes exhibited by the model.

This chapter also serves as foundation for the development of a more biophysical model in chapter 3. There, we will include several features we neglect in this chapter for the sake of simplicity in order to highlight the core features of this model.

### 2.1 Wave propagation by critical oscillators

In the following, we propose a model which extends the model developed by T. Duke and F. Jülicher [41], which is set up in the frequency domain. This is convenient for investigating cyclo-stationary responses to stimuli which are periodic in time. Nevertheless, there exist some drawbacks and aspects a model in the frequency domain is not perfectly adjusted to address. We extend the model by T. Duke and F. Jülicher by considering a corresponding set of equa-

tions in the time domain. This enables us to include various kinds of noise more easily, to study transient phenomena such as responses to click stimuli, and to study spontaneous otoacoustic emissions. First, we derive the governing hydrodynamic equations in the time domain, which have been used frequently in previous models [164, 81, 146, 41]. Finally, we focus on the local oscillator dynamics.

The cochlea is a fluid-filled cavity in the skull, encapsulated by both bone and the membranes of the oval and round window. The density  $\rho$  of the intracochlear fluid is comparable to that of water. The cochlea is longitudinally divided into three chambers. In the upper and lower chamber the fluid behaves similarly to water, whereas in the middle chamber the fluid is substantially more viscous. Due to this fact, at each cross section the middle chamber moves essentially as one. The coiling of the cochlea is believed to serve the purpose of making the cochlea more compact, i.e., to conserve space [6]. It is believed that coiling does not alter the essential response of the cochlea [14, 143], which is supported by the fact that there exist mammals without substantial coiling, for instance the spiny anteater. However, recent research suggests that coiling might affect cochlear mechanics in the low frequency region by tilting waves and directing the wave energy density towards the outer portion of the BM, which effectively causes higher amplitudes of the traveling waves compared to the uncoiled case [90, 91]. According to theoretical calculations, coiling can amplify low-frequency sounds in the human cochlea by as much as 20 dB.

In order to simplify matters, we neglect the curvature and the varying cross-sectional area of the cochlea [150]. Consequently, we describe the cochlea as a rectangular box with two chambers separated in the middle by the BM, except for the helicotrema at the apex where the chambers are connected. See Fig. 2.1 for a sketch of the model.

As the inner ear is an insulated system, we can safely assume conservation of fluid volume. Assuming also incompressibility of the fluid leads to the following implications: A volume flow  $J_1$  in the upper chamber is associated with a volume flow  $J_2$  of the same magnitude and opposite sign in the lower chamber. Furthermore, a change in the volume flow is accompanied by a vertical displacement  $h$  of the BM. Considering a segment  $[x, x + \Delta x]$  of the cochlea, it holds

$$-\Delta V = b\Delta x\Delta h \Rightarrow -\frac{\Delta J_1}{\Delta x} = b\partial_t h \Rightarrow -\partial_x J_1 = b\partial_t h,$$

where  $V$  is the volume of the upper chamber in the segment  $[x, x + \Delta x]$ , and  $b$  is the breadth of the BM. From the calculation above,  $\partial_x J_2 = b\partial_t h$  follows similarly. By defining

$$j = J_1 - J_2 \tag{2.1}$$

we obtain

$$\partial_x j = -2b\partial_t h. \tag{2.2}$$

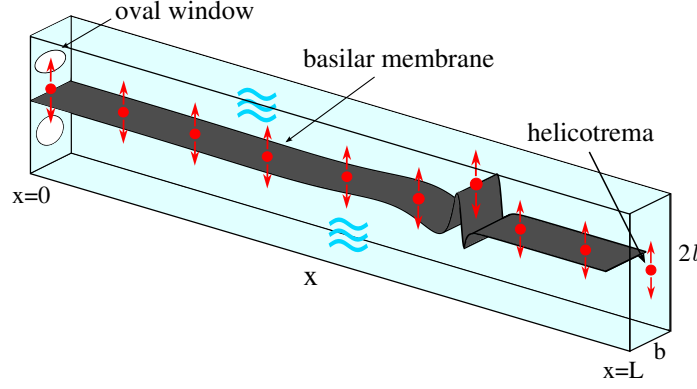


Figure 2.1: **Schematic representation of the cochlear model.** The rectangular cochlea of length  $L$ , breadth  $b$  and height  $2l$ , is separated by the BM (dark gray) in two fluid-filled chambers. The oval window is located at position  $x = 0$ , the helicotrema at  $x = L$ . The ellipse below the oval window indicates the round window. Vertical displacements of the BM are denoted by  $h(x)$ . The BM is represented by a chain of oscillators (red dots) which are coupled via hydrodynamic interactions (blue waves).

Furthermore, balance of forces is assumed. Considering again a segment  $[x, x + \Delta x]$  of the upper chamber of the cochlea, this condition reads  $F = ma$ , where  $F$  is the net force acting in horizontal direction on the segment,  $m$  is its mass, and  $a$  is the acceleration in longitudinal direction of the fluid in the segment. Physiological movements of the BM are considerably smaller than the height  $l$  of the upper and lower chamber (both possess the same height):  $h$  is typically on the order of nanometers, whereas  $l = 1$  mm. Thus, we obtain  $l - h \approx l$ . It follows  $F = b(l - h)(P_1(x) - P_1(x + \Delta x)) \approx bl(P_1(x) - P_1(x + \Delta x))$ , where  $P_1$  is the pressure in the upper chamber. In addition,  $ma = \rho Va = \rho \Delta x b(l - h)a \approx \rho \Delta x b l a = \rho \Delta x \partial_t J_1$  holds true. From these considerations we obtain

$$-bl\partial_x P_1(x) = \rho\partial_t J_1. \quad (2.3)$$

Analogously,  $-bl\partial_x P_2(x) = \rho\partial_t J_2$  can be derived, where  $P_2$  is the pressure in the lower chamber. We define

$$p = P_1 - P_2 \quad (2.4)$$

as the pressure difference between the two chambers. Thus, we arrive at

$$-bl\partial_x p = \rho\partial_t j. \quad (2.5)$$

Combining the temporal derivative of Eq. (2.2) and the spatial derivative of Eq. (2.5) results in

$$\partial_x^2 p = \frac{2\rho}{l} \partial_t^2 h, \quad (2.6)$$

which provides the hydrodynamic interaction and coupling along the BM.

*The model in the frequency domain proposed by T. Duke and F. Jülicher*

The equations of the model in the frequency domain which was proposed by T. Duke and F. Jülicher contains two equations: The Fourier transformation of Eq. (2.6), which reads

$$\frac{d^2 \tilde{p}}{dx^2} = -\frac{2\rho\omega^2}{l} \tilde{h}, \quad (2.7)$$

together with the local oscillator relation given by the Hopf normal form in the frequency domain,

$$\tilde{p} = \hat{\alpha}(\omega(x) - \omega)\tilde{h} + i\hat{\beta}|\tilde{h}|^2\tilde{h}, \quad (2.8)$$

where  $\hat{\alpha}$  and  $\hat{\beta}$  are real constants, and  $\omega(x)$  is the local best frequency of the BM. We will address the choice of these parameters later in more detail. The two equations are supplemented by the boundary conditions, which fix the pressure at both ends of the cochlea:  $\tilde{p}(x=0) = \gamma$ , where  $\gamma$  is the pressure amplitude, and  $\tilde{p}(x=L) = 0$  as the two channels are connected at  $x=L$ .

Now we turn towards a description of the local oscillator dynamics in the time domain. In our description, a single oscillator models the vertical motion of one small segment of the organ of Corti and the BM, including one inner and three to five outer hair cells and their rod-like protrusions termed stereocilia.

Hopf oscillators in the vicinity of the critical point provide a good description of dynamics of hair bundles, cochlear partitions, and the auditory system itself: As outlined in section 1.1.1, stereocilia, which are intimately associated with the BM motion, exhibit features observable in experiments on the whole auditory system. One such property is the nonlinear amplification. For some non-mammalian species, stereocilia have been found to frequently exhibit spontaneous oscillations [94]. It was shown that stereocilia deflection dynamics can be well described by Hopf oscillators near the critical point. Furthermore, for a model of an individual cochlear partition it was derived that the interplay of active hair bundle motility and somatic motility can lead to a Hopf bifurcation [112].

Finally, note that critical oscillators, i.e., Hopf oscillators at the critical point, share essential properties with the hearing organs of mammals, such as sharp frequency selectivity, extreme sensitivity, and a wide dynamic range [43]. Hopf oscillators which are slightly in the oscillatory regime exhibit self-sustained oscillations, thus they provide a possible candidate for modeling spontaneous otoacoustic emissions of the cochlea.

Due to these facts, it seems appropriate to employ Hopf oscillators for the description of local BM dynamics. Note that this description is independent of the physical details. It does not predict how exactly nature manufactures the mechanism and how the dynamical system adjusts itself to maintain proximity to the critical point. In contrast, it is a generic description revealing that the

above mentioned properties are independent of the exact realization but are due to the proximity of a dynamic instability. However, there exists a possible mechanism explaining how the vicinity to the supercritical Hopf bifurcation point could be achieved [42].

The Hopf normal form in the time domain, representing the local BM dynamics, reads

$$\frac{dz}{dt} = (\epsilon + i\omega(x))z - \frac{\beta}{\alpha} |z|^2 z - \frac{i}{\alpha} p. \quad (2.9)$$

The dynamics of a Hopf oscillator in the time domain is described by a complex variable  $z = h + iu$ , where  $h$  is the vertical displacement of the BM, and  $u$  is an auxiliary variable related to the velocity of the BM. The bifurcation parameter  $\epsilon$  governs the spontaneous activity. In this chapter, we only show simulation results for the system where all oscillators are critical, i.e.,  $\epsilon = 0$ . The local best frequency  $\omega(x) = \omega_0 e^{-x/d}$  is a function of the distance  $x$  to the stapes, decaying exponentially from base to apex with decay constant  $d$ . The passive stiffness  $\alpha \cdot \omega(x)$  (per unit area of the BM) governs the relation between the pressure difference  $p$  and the vertical deflection  $h$ . We will investigate this in more detail below. The parameter  $\alpha$  is constant as both stiffness and characteristic frequency vary in a similar manner along the BM [14]. The nonlinearity  $\beta$  shapes the peak of the traveling wave. Its value is unknown and might possibly depend on location and frequency. For simplicity,  $\beta$  is assumed to be a constant real number. The numerical value of  $\beta$  is chosen such that the model fits the experimental SFOAE response [41], i.e., that it describes the magnitude of the experimentally observed BM vibration in case of sinusoidal stimuli with driving frequencies in the range of the local characteristic frequencies present on the BM. Unless stated otherwise, all parameters are real numbers. For exact numerical values see table 2.1.

The boundary conditions for this chapter are given by fixating the pressure at the stapes and the helicotrema:

$$p(x = 0, t) = A \sin(\omega t), \quad (2.10)$$

$$p(x = L, t) = 0. \quad (2.11)$$

At the helicotrema, located at the apex at  $x = L$ , the two channels are connected. Thus, the pressure difference vanishes. We prescribe a pressure amplitude  $A \in \mathbb{R}$  on the left side. Note that later we are going to replace the boundary condition at the base by a more sophisticated one, taking middle ear dynamics into account, which is more appropriate for the investigation of SOAEs.

In general, the middle ear amplifies incoming sound, where the amplification is strongly dependent on the frequency and amplitude and the specific details of the sounds, such as its duration and source. For simplicity, in this chapter the effect of the middle ear is taken into account by amplifying incoming sound by 20 dB - regardless of sound pressure level or frequency.

The terms appearing in Eq. (2.9) correspond to the standard Hopf normal form,

Table 2.1: List of parameters for chapter 2

Parameter	Definition	Value
$\alpha$	BM stiffness proportionality factor	$5 \cdot 10^3$ Pa s/m
$b$	average breadth of BM	1.1 mm
$\beta$	nonlinearity	$1.25 \cdot 10^{22}$ Pa/m <sup>3</sup>
$d$	decay constant	7 mm
$\Delta x$	distance between oscillators	$10^{-5}$ m
$\epsilon$	bifurcation parameter	0 Hz
$l$	height of upper/lower chamber	1 mm
$L$	length of cochlea	35 mm
$\rho$	density of fluid in cochlea	$10^3$ kg/m <sup>3</sup>
$\omega_0$	angular frequency at $x = 0$	$10^5$ Hz
$\omega(x)$	local best frequency	$\omega_0 e^{-x/d}$

with exception of the last term. What determines the exact form of the term  $-\frac{i}{\alpha}p$ ? A heuristic justification is that this choice ensures that  $p$  acts solely on  $u$ , the imaginary part of  $z$ . The variable  $u$  is related to the velocity of  $h$ , see subsection 2.3. Thus, this specific choice seems reasonable as in an harmonic oscillator forces act solely on the velocity. The exact form of the term  $-i/\alpha$  stems from considerations in the frequency domain representation: Assuming that  $|\tilde{z}|^2 \tilde{z} \approx \widetilde{|z|^2 z}$ , the Fourier transform of Eq. (2.9) reads  $\tilde{p} \approx \alpha(\omega(x) - \omega)\tilde{z} + i\beta|\tilde{z}|^2 \tilde{z}$ . Furthermore, approximating  $|\tilde{z}| \approx 2|\tilde{h}|$  and inserting  $\tilde{z} = 2\tilde{h}$  leads to

$$\tilde{p} \approx 2\alpha(\omega(x) - \omega)\tilde{h} + i8\beta|\tilde{h}|^2 \tilde{h}. \quad (2.12)$$

Assuming exact equality, this equation corresponds to the frequency domain model, in particular Eq. (2.8).

In the linear case, i.e. for  $\beta = 0$ ,  $\alpha$  is the constant governing the response of the BM to a certain pressure difference  $\tilde{p}$ . In linear order we have  $\tilde{p} = 2\alpha(\omega(x) - \omega)\tilde{h}$ . For low frequencies  $p$  and  $h$  are in phase, which corresponds to a purely real  $\alpha$ . For  $\omega = 0$  we obtain  $\tilde{p} = 2\alpha\omega(x)\tilde{h}$ . This relation of the static deflection corresponds well to experimental data for constant  $\alpha \in \mathbb{R}$ . Put differently, the static stiffness per unit area is given by  $\alpha\omega(x)$  [14]. This results in the formulation of Eq. (2.9) in the time domain with the factor  $\alpha$  appearing in the nonlinearity, and it also leads to the term  $-\frac{i}{\alpha}\tilde{p}$ .

## 2.2 Discretization of the equations and solution methods in the time domain

In this section, we consider how to interpret the equations presented in the previous section. In particular, we discretize the equations spatially. Finally, we

show how to simulate these equations forward in time.

The above continuum description of cochlear mechanics in the time domain consists of one real valued equation governing hydrodynamic interactions, given by Eq. (2.6), and one complex valued equation - or equivalently two real valued equations - describing local oscillator dynamics, given by Eq. (2.9). The equations are supplemented by the boundary conditions for the pressure at both ends, given by Eqs. (2.10) and (2.11). Consequently, the equations for the real valued system variables  $h$ ,  $u$ , and  $p$  read:

$$\partial_t^2 h = \frac{l}{2\rho} \partial_x^2 p, \quad (2.13)$$

$$\frac{dh}{dt} = -\omega(x)u + \epsilon h - \frac{\beta}{\alpha} (h^2 + u^2) h, \quad (2.14)$$

$$\frac{du}{dt} = \omega(x)h + \epsilon u - \frac{\beta}{\alpha} (h^2 + u^2) u - \frac{1}{\alpha} p, \quad (2.15)$$

complemented by the boundary conditions

$$p(x = 0, t) = A \sin(\omega t), \quad p(x = L, t) = 0. \quad (2.16)$$

Model parameters can be found in table 2.1. At first glance the system seems simultaneously under- and overdetermined: It provides one rule for the time evolution of  $u$  but none for  $p$ , and two for  $h$ .

In order to evolve the system forward in time, for given  $h$  and  $u$  at time  $t_0$ , we calculate  $p$  at time  $t$  to determine  $\partial_t h, \partial_t u$  and thus compute  $h$  and  $u$  at time  $t + \Delta t$ . For calculating  $p$  at time  $t$ , we repeatedly insert Eqs. (2.14) and (2.15) into the left side of Eq. (2.13). Put differently, we substitute  $\partial_t h$  and  $\partial_t u$  repeatedly by their governing equations, finally obtaining a second-order ordinary differential equation in  $p$ ,

$$\begin{aligned} \partial_x^2 p = \frac{2\rho}{l} \partial_t^2 h = \frac{2\rho}{l} & \left( -\omega(x)u + \epsilon h - \frac{\beta}{\alpha} (h^2 + u^2) h \right) \left( \epsilon - \frac{\beta}{\alpha} (3h^2 + u^2) \right) \\ & - \frac{2\rho}{l} \left( \omega(x)h + \epsilon u - \frac{\beta}{\alpha} (h^2 + u^2) u \right) \left( \omega(x) + \frac{\beta}{\alpha} 2uh \right) \\ & + \frac{2\rho}{l\alpha} p \left( \omega(x) + \frac{\beta}{\alpha} 2uh \right). \end{aligned} \quad (2.17)$$

The resulting ordinary differential equation can be written in the form

$$\frac{d^2 p(x)}{dx^2} + p(x) \gamma(x, h(x), u(x)) = g(x, h(x), u(x)), \quad (2.18)$$

where  $\gamma, g$  are  $p$ -independent, nonlinear functions, determined by Eq. (2.17). Now we discretize the equations and the variables  $p, h$ , and  $u$  spatially in longitudinal direction.

The hydrodynamic equation (2.13) can be understood in its continuous formulation, but the local oscillator equations (2.14), (2.15) are to be interpreted discretely in space in longitudinal direction as the cochlear physiology provides a natural discretization: The human organ of Corti is divided in longitudinal direction into roughly 3500 segments, corresponding to an average segment width of  $10 \mu m$  [32]. Each segment, the so-called cochlear partition, comprises one inner hair cell and usually three to four outer hair cells. Consequently, we discretize our model spatially in longitudinal direction with an equidistant spacing of  $\Delta x = 10 \mu m$ , giving rise to a chain of oscillators  $z_0, \dots, z_N$  with  $N = 3500$ . This implies that we perform a discretization approximation for Eq. (2.13).

We change coordinates by  $x \rightarrow j$  and  $f(x) \rightarrow f_j$ , where  $x = j\Delta x$ . Spatial derivatives are discretized in the standard way [40, 44] by means of

$$\frac{d^2 f(x)}{dx^2} = \frac{f_{j+1} - 2f_j + f_{j-1}}{(\Delta x)^2}.$$

Consequently, we obtain a discretized version a system of linear equations

$$\frac{p_{j+1} - 2p_j + p_{j-1}}{(\Delta x)^2} + p_j \gamma(x = j\Delta x, h_j, u_j) = g(x = j\Delta x, h_j, u_j).$$

It is now necessary to solve the discretized ordinary differential equation for each instance in time. One way of obtaining a solution for this type of equation is given by the shoot-and-match method, which was employed in the frequency domain model which we extend [41]. However, for this setup the shoot-and-match method, where one starts from one side and tries to match the second boundary condition, turns out to be unstable. This is mainly because the desired values for  $p(x = 0, t)$  cannot always be matched with the required precision. In contrast, the method of finite differences fulfills the correct boundary conditions for  $p(x = 0, t)$ ,  $p(x = L, t)$ , see Eq. (2.16), by definition and turns out to be well suited for this model. It turned out that this scheme had been used for other one-dimensional cochlea models as well [44, 100, 139]. The method of finite differences solves the differential equation by solving the corresponding tridiagonal matrix equation, which results from the discretization. In matrix form, the resulting system of equations can be written as

$$\begin{pmatrix} 1 & 0 & & & & & & & & 0 \\ a & b_1 & a & & & & & & & \\ & \ddots & \ddots & \ddots & & & & & & \\ & & a & b_i & a & & & & & \\ & & & \ddots & \ddots & \ddots & & & & \\ & & & & a & b_{N-1} & a & & & \\ 0 & & & & & 0 & 1 & & & \end{pmatrix} \begin{pmatrix} p_0 \\ p_1 \\ \vdots \\ p_i \\ \vdots \\ p_{N-1} \\ p_N \end{pmatrix} = \begin{pmatrix} g_0(h_0, u_0) \\ g_1(h_1, u_1) \\ \vdots \\ g_i(h_i, u_i) \\ \vdots \\ g_{N-1}(h_{N-1}, u_{N-1}) \\ g_N(h_N, u_N) \end{pmatrix}, \quad (2.19)$$

with  $a = \frac{1}{(\Delta x)^2}$  and  $b_j = -2a + \gamma_j$ , where  $\gamma_j = -\frac{2\rho}{l\alpha} \left( \omega(x_j) + \frac{\beta}{\alpha} 2u_j h_j \right)$ .

It holds  $g_0 = A \sin(\omega t_0)$  and  $g_N = 0$ . For  $1 \leq j \leq N - 1$  we have

$$g_j = \frac{2\rho}{l} \left( -\omega(x_j)u_j + \epsilon h_j - \frac{\beta}{\alpha} (h_j^2 + u_j^2) h_j \right) \left( \epsilon - \frac{\beta}{\alpha} (3h_j^2 + u_j^2) \right) - \frac{2\rho}{l} \left( \omega(x_j)h_j + \epsilon u_j - \frac{\beta}{\alpha} (h_j^2 + u_j^2) u_j \right) \left( \omega(x_j) + \frac{\beta}{\alpha} 2u_j h_j \right).$$

We solve the above matrix equation with the efficient algorithm "tridag" for tridiagonal matrix equations [108]. For an  $N \times N$  matrix, the algorithm needs approximately  $3N$  steps to calculate the solution vector  $p$ . This is substantially faster than general algorithms for inverting matrices which may need a number of steps proportional to  $N^2$ . Note that due to the absence of pivoting, the algorithm can theoretically crash even if the matrix equation is solvable, but this unlikely event never occurred during the numerous times this algorithm has been used for our research.

The dynamics in time are discretized by using finite time steps of size  $\Delta t = 10^{-5}$  s. To compute  $h(x, t_0 + \Delta t)$  and  $u(x, t_0 + \Delta t)$ , the second-order Runge-Kutta method is employed, as it turns out that the Euler method requires too small time steps and thus slows down simulations substantially. Throughout this thesis, the starting conditions are chosen to be  $h_i = u_i = p_i = 0$  for all  $i = 0, \dots, N$ . Note that system dynamics for times after a short relaxation time are independent of the initial conditions.

In Fig. 2.2 the response of the time domain model to a weak sinusoidal signal with a frequency of 1300 Hz is plotted. It is visible how the traveling wave builds up over time from shortly after the onset of the stimulus, shown in the upper graph, until it has reached a cyclo-stationary state after 50 ms, displayed in the lowest graph of Fig. 2.2. The wave travels from left to right. As observed in experiments, the magnitude of the BM deflection in response to stimuli builds up along the BM until the wave reaches the resonance frequency, after which there is a steep decay. Note that the waves accumulate on the apical side of the peak. The magnitude of the displacement caused by these waves decays over time (not shown here).

In Fig. 2.3 we see the Fourier transform of the BM responses of the model to periodic stimuli of different strengths and frequencies. In experiment as well as in our model, the response to faint stimuli is sharp, localized at the region of the resonance frequency. For stronger inputs, the BM response becomes broader and the maximum of the envelope of the BM response shifts to the left. For experimental traveling waves in the guinea pig, see Fig. 1.9 A. Note that, due to the frequency gradient, for high frequencies the maximum of the BM response is located near the base, low frequencies elicit a maximum in the proximity of the apex.

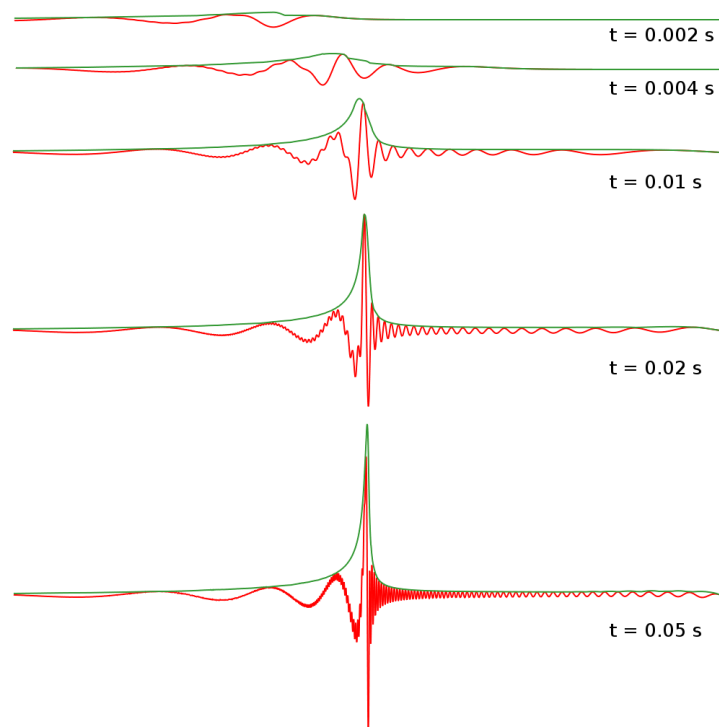


Figure 2.2: **BM vibrations for different instances in time in presence of a sinusoidal signal.** The response of the BM to a periodic low-level stimulus of 20 dB amplitude and a frequency of 1300 Hz is shown. For different instances in times  $t$ , denoted in the upper right corners of the individual graphs, the red lines denote snapshots of instant BM deflections as a function of longitudinal position  $x$ , ranging from  $x = 0$  on the left side to  $x = L$  on the right side. The green lines represent the envelope of the BM deflections, for each location  $x$  denoting the value  $\max_{t' \leq t} |h(x, t')|$ .

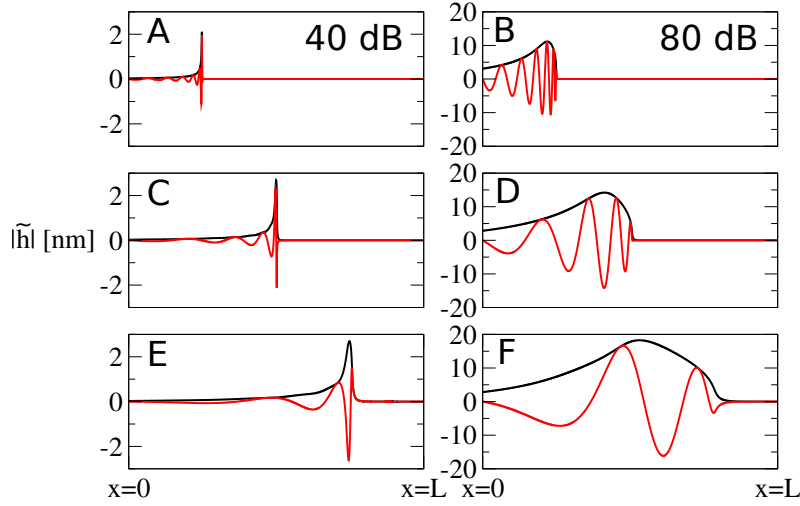


Figure 2.3: **BM vibration amplitude  $|\tilde{h}|$  in response to sinusoidal stimuli of different frequencies and strengths.** In each graph,  $|\tilde{h}|$ , given in units of nanometers, is shown as a function of longitudinal position  $x$ . In the left column, i.e. for graphs A, C, and E, the sound pressure level is 40 dB. In the right column, i.e. for graphs B, D, and F, the sound pressure level is 80 dB. The pure tone frequency is given by 4.6 kHz in graphs A and B, 1.3 kHz in graphs C and D, and 0.37 kHz in graphs E and F. Note that all oscillators in the simulated model are at the critical point, i.e.  $\epsilon = 0$ .

### Solving the set of equations in an alternative way

There exists another way to evolve the presented model forward in time. As before, we have the following system of three real valued equations, where we omitted the terms with the bifurcation parameter  $\epsilon$  for simplicity:

$$\partial_t^2 h = \frac{l}{2\rho} \partial_x^2 p, \quad (2.20)$$

$$\frac{dh}{dt} = -\omega(x)u - \frac{\beta}{\alpha} (h^2 + u^2) h, \quad (2.21)$$

$$\frac{du}{dt} = \omega(x)h - \frac{\beta}{\alpha} (h^2 + u^2) u - \frac{1}{\alpha} p. \quad (2.22)$$

In the previous section we obtained a second-order ordinary differential equation in  $p$  by inserting Eq. (2.21) and Eq. (2.22) repeatedly into Eq. (2.20). Here we use a different approach deriving an ordinary differential equation in  $\partial_t u$ , which will result in the elimination of  $p$ : First, Eq. (2.22) is solved for  $p$  and then

inserted into the right side of Eq. (2.20). Then, Eq. (2.21) is inserted into the left side of Eq. (2.20). This results in the following equation:

$$\frac{2\rho}{l} \partial_t \left[ -\omega(x)u - \frac{\beta}{\alpha} (h^2 + u^2) h \right] = \partial_x^2 [\alpha\omega(x)h - \beta (h^2 + u^2) u - \alpha\partial_t u].$$

By applying the chain rule on both sides, inserting Eq. (2.21), and reordering terms, we obtain

$$\begin{aligned} & -\frac{2\rho}{l} \left( \omega(x) + 2\frac{\beta}{\alpha} uh \right) \partial_t u + \alpha \partial_x^2 \partial_t u \\ &= \frac{2\rho}{l} \frac{\beta}{\alpha} (3h^2 + u^2) \left( -\omega(x)u - \frac{\beta}{\alpha} (h^2 + u^2) h \right) + \alpha\omega(x) \left[ \partial_x^2 h - 2\frac{1}{d} \partial_x h + \frac{1}{d^2} h \right] \\ & \quad - \beta [6u(\partial_x u)^2 + (3u^2 + h^2)\partial_x^2 u + 2u(\partial_x h)^2 + 2hu\partial_x^2 h + 4h\partial_x h\partial_x u]. \end{aligned}$$

As before, the spatial discretization is performed by  $x \rightarrow j$  and  $f(x) \rightarrow f_j$ , where  $x = j\Delta x$ . Applying the standard spatial derivative discretizations, as denoted in the previous subsection, gives rise to

$$\begin{aligned} & \left( -\frac{2\rho}{l} \left( \omega(x_j) + 2\frac{\beta}{\alpha} u_j h_j \right) - \frac{2\alpha}{(\Delta x)^2} \right) \partial_t u_j + \frac{\alpha}{(\Delta x)^2} (\partial_t u_{j-1} + \partial_t u_{j+1}) = \\ & \quad \frac{2\rho}{l} \frac{\beta}{\alpha} (3h_j^2 + u_j^2) \left( -\omega(x_j)u_j - \frac{\beta}{\alpha} (h_j^2 + u_j^2) h_j \right) \\ & \quad + \alpha\omega(x_j) \left[ \frac{h_{j+1} - 2h_j + h_{j-1}}{(\Delta x)^2} - 2\frac{1}{d} \frac{h_{j+1} - h_{j-1}}{2\Delta x} + \frac{1}{d^2} h_j \right] \quad (2.23) \\ & \quad - \beta \left[ 6u_j \left( \frac{u_{j+1} - u_{j-1}}{2\Delta x} \right)^2 + (3u_j^2 + h_j^2) \frac{u_{j+1} - 2u_j + u_{j-1}}{(\Delta x)^2} \right] \\ & \quad - \beta \left[ 2u_j \left( \frac{h_{j+1} - h_{j-1}}{2\Delta x} \right)^2 + 2h_j u_j \frac{h_{j+1} - 2h_j + h_{j-1}}{(\Delta x)^2} \right] \\ & \quad - \beta \left[ 4h_j \frac{h_{j+1} - h_{j-1}}{2\Delta x} \frac{u_{j+1} - u_{j-1}}{2\Delta x} \right]. \end{aligned}$$

In matrix form, the resulting system of equations can be written as

$$\begin{pmatrix} 1 & 0 & & & 0 \\ a & b_1 & a & & \\ & a & b_2 & a & \\ & & \ddots & \ddots & \ddots \\ & & & a & b_{N-1} & a \\ 0 & & & & 0 & 1 \end{pmatrix} \begin{pmatrix} \partial_t u_0 \\ \partial_t u_1 \\ \vdots \\ \partial_t u_N \end{pmatrix} = \begin{pmatrix} s_0 \\ s_1 \\ \vdots \\ s_N \end{pmatrix}, \quad (2.24)$$

with  $a = \frac{\alpha}{(\Delta x)^2}$ ,  $b_j = -\left( \frac{2\rho}{l} \left( \omega(x_j) + 2\frac{\beta}{\alpha} u_j h_j \right) + \frac{2\alpha}{(\Delta x)^2} \right)$ . The  $s_j$  for  $1 < j < N$  are equal to the right side of the discretized equation (2.23). At the

boundaries we have  $p(x = 0, t) = A \sin(\omega t)$  and  $p(x = L, t) = 0$ , which gives us  $\partial_t u_0$  and  $\partial_t u_N$ . The boundary conditions are incorporated via the first and last line of the matrix and by setting

$$s_0 = \partial_t u_0 = w_0 h_0 - \frac{\beta}{\alpha} (h_0^2 + u_0^2) u_0 - \frac{1}{\alpha} A \sin(\omega t), \quad (2.25)$$

$$s_N = \partial_t u_N = w_0 e^{-L/d} h_N - \frac{\beta}{\alpha} (h_N^2 + u_N^2) u_N. \quad (2.26)$$

Thus, we can now calculate  $\partial_t u_j$  by solving the matrix equation (2.24) as described in the previous section. Furthermore, we already knew  $\partial_t h_j$ , as the governing equation does not contain any pressure terms. The knowledge of  $\partial_t h_j$  and  $\partial_t u_j$  enables us to integrate  $h_j$  and  $u_j$  forward in time. The next steps are the same as in the previously described integration scheme.

Note that both methods are equivalent, which is not shown here. In particular, this alternative method does not explicitly calculate  $p_j$ , but it can be calculated via Eq. (2.22).

## 2.3 Linear waves as a limit case of the nonlinear model

In this section, we compare the Hopf normal form with the harmonic oscillator, and we present approximate solutions of the linear cochlea, which turns out to be insightful for the investigation of the cochlear traveling wave.

### The linear Hopf oscillator

In this section, we show the correspondence between the Hopf normal form in the time domain with  $\beta = 0$ , which we call the linear case, and the harmonic oscillator. Recall that the linear form of the Hopf normal form for  $z = h + iu$  reads

$$\frac{dz}{dt} = i\Omega z + \epsilon z - \frac{i}{\alpha} p. \quad (2.27)$$

The dynamics of the damped harmonic oscillator with observable  $y$  is given by

$$m \frac{d^2 y}{dt^2} + \gamma \frac{dy}{dt} + m\Omega_0^2 y = F(t), \quad (2.28)$$

with mass  $m$ , damping constant  $\gamma$ , eigenfrequency  $\Omega_0$ , and driving force  $F(t)$ . If we identify  $y = h$  and set  $v = \frac{dh}{dt} = -\Omega u + \epsilon h$ , we obtain  $u = (\epsilon h - v)/\Omega$ . This leads to

$$\frac{dv}{dt} = 2\epsilon v - (\Omega^2 + \epsilon^2)h + \frac{\Omega}{\alpha} p,$$

which results in the identifications  $\gamma = -2\epsilon m$ ,  $\Omega_0 = \sqrt{\Omega^2 + \epsilon^2}$ . Note that  $\epsilon$  influences both friction and eigenfrequency. For  $\epsilon < 0$  the friction is positive and vice versa, as expected.

However, different choices of identification are also possible. We reproduce one other choice [152], taking also longitudinal coupling into account, which will turn out to be useful for considerations in consecutive chapters. Suppose we have Eq. (2.28) with  $F(t) = \hat{k}_{el}(y_2 - 2y + y_0) + \hat{k}_{di}(\partial_t y_2 - 2\partial_t y + \partial_t y_0)$ , where  $y_2, y_0$  are two oscillators to which  $y$  is coupled by means of elastic and dissipative coupling  $\hat{k}_{el}$  and  $\hat{k}_{di}$ , respectively. By identifying  $z = y - i/\Omega_0 \partial_t z$  in Eqs. (2.27) and (2.28), we obtain

$$\frac{dz}{dt} = i\Omega z + 2i\epsilon u + 2ik_{el}(h_0 - 2h + h_2) + 2ik_{di}(u_0 - 2u + u_2), \quad (2.29)$$

where  $z_j = h_j + iu_j$  (for  $j = 0, 2$ ) are the oscillators to which  $z$  is coupled. We arrive at

$$\Omega = \Omega_0, \quad \epsilon = -\gamma/(2m), \quad k_{el} = -\hat{k}_{el}/(2m\Omega_0), \quad k_{di} = \hat{k}_{di}/(2m). \quad (2.30)$$

By incorporating an additional term of third order in  $z$  in Eq. (2.29), we obtain

$$\frac{dz}{dt} = i\Omega z + 2i\epsilon u + 2ik_{el}(h_0 - 2h + h_2) + 2ik_{di}(u_0 - 2u + u_2) + O(z^3). \quad (2.31)$$

If the system described by this equation is close to the Hopf bifurcation and if oscillations are small, Eq. (2.31) can be written in the Hopf normal form

$$\frac{dz}{dt} = i\Omega z + \epsilon z + (k_{di} + ik_{el})(z_0 - 2z + z_2) - B|z|^2 z, \quad (2.32)$$

where  $B$  is the parameter governing the strength of the nonlinearity. This formulation will be used later for introducing longitudinal coupling.

Coupled harmonic oscillators can be employed to describe BM segments, taking into account observable physiological properties such as mass, damping, stiffness, and experimentally measured coupling strengths. This is not easily possible in the framework of the Hopf normal form. The coupling strength relations in Eq. (2.30) enable us to compare coupling strengths used in the model with experimentally observed coupling strengths. Note that the conversion factors of elastic and dissipative coupling differ by the factor  $\Omega$ . In particular, a ratio of  $r = k_{el}/k_{di}$  for coupling strengths of the model involving Hopf oscillators corresponds to a ratio of  $r\Omega_0$  in the harmonic oscillator model. For the frequencies under consideration in this thesis, the last-mentioned ratio is substantially higher than the first one.

Note that the first transformation presented here,  $h = y$ , can be also performed in presence of elastic longitudinal coupling  $k_{el}(h_0 - 2h + h_2)$ , resulting in an identification  $\hat{k}_{el} = -m\Omega_0 k_{el}$ .

### The linear cochlea

The nonlinearity  $\beta$  ensures that oscillations do not grow without bounds. Provided the hydrodynamic coupling together with the discrete setup of the model or the bifurcation parameter limit the oscillations of each oscillator, the nonlinearity is not essential in the following sense: It does not determine whether or not there are non-zero oscillations at a certain location. It only influences the magnitude of oscillations significantly above a certain threshold. For small sinusoidal stimuli the nonlinearity acts only in the vicinity of the resonance. This fact can be used to approximate cochlear waves by means of analytical approaches such as the WKB method [10]. We show the result which was presented for the model developed by T. Duke and F. Jülicher [41]: In regions where the nonlinearity  $\beta$  can be neglected, the WKB approximation can be employed. Considering the Fourier transformed time domain model equations with  $\beta = 0$ , we obtain  $\tilde{p} \approx 2\alpha(\omega(x) - \omega)\tilde{h}$ , see Eq. (2.37), and  $-\omega^2\tilde{h} = \frac{l}{2\rho}\partial_x^2 p$ , arriving at the second-order ordinary differential equation

$$\frac{l\alpha}{\rho\omega^2} \frac{d^2\tilde{p}}{dx^2} = \frac{-1}{\omega(x) - \omega} \tilde{p}. \quad (2.33)$$

The WKB approximation of the BM displacement gives the two terms

$$\tilde{h}_{1,2}(x) = (\omega(x) - \omega)^{3/4} e^{\pm i \int_0^x dx' q(x')}, \quad q(x') = \sqrt{\frac{\rho\omega^2}{l\alpha(\omega(x) - \omega)}}, \quad (2.34)$$

whose weighted sum describes  $\tilde{h}$ , where the weights are determined by the boundary conditions. The formula shows that for  $\omega < \omega(x)$  there are two traveling waves  $\tilde{h}_1, \tilde{h}_2$ , corresponding to real  $q(x)$ , and for  $\omega > \omega(x)$  the wave is quickly decaying as  $q(x)$  becomes imaginary.

## 2.4 Comparison with a frequency domain approximation

In this section, we compare the model developed in the time domain in section 2.1 with the model formulated in the frequency domain, proposed by T. Duke and F. Jülicher [41].

The Hopf normal form in the time domain for an oscillator driven by a pressure difference  $p$  reads

$$\frac{dz}{dt} = (\epsilon + i\omega(x))z - \frac{\beta}{\alpha}|z|^2 z - \frac{i}{\alpha}p. \quad (2.35)$$

Assuming that  $|\tilde{z}|^2 \tilde{z} \approx \widetilde{|z|^2 z}$ , the Fourier transformation of this equation takes the form

$$\tilde{p} \approx \alpha(\omega(x) - \omega - i\epsilon)\tilde{z} + i\beta|\tilde{z}|^2 \tilde{z}. \quad (2.36)$$

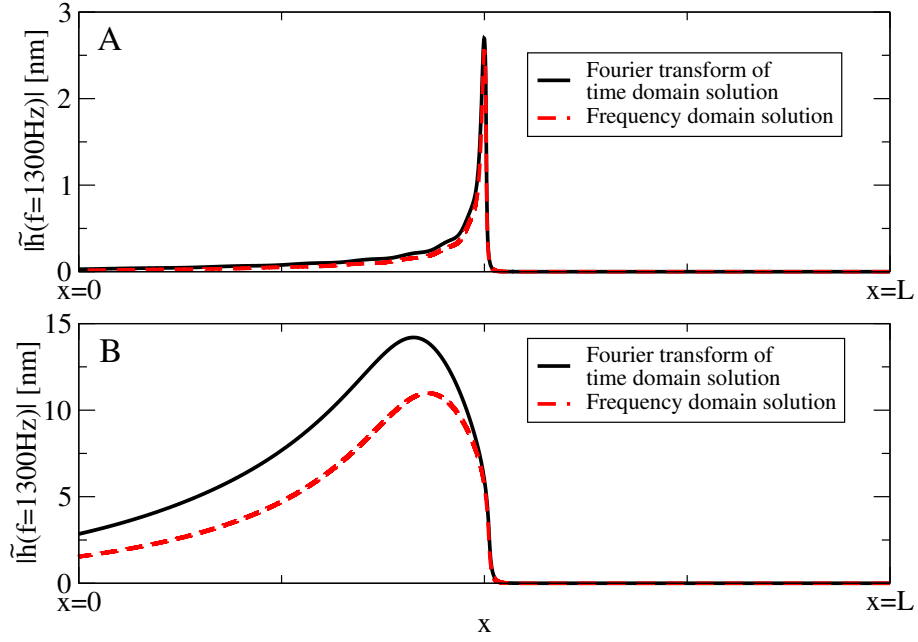


Figure 2.4: Absolute BM displacement  $|\tilde{h}|$  in response to a sinusoidal input stimulus with  $f = 1300$  Hz for low and high intensity: A) 40 dB, B) 80 dB. The black lines denote the Fourier transform of the response of the time domain model, considered at the driving frequency. The red lines represent the solution of the frequency domain model. Note that all oscillators are critical, i.e.,  $\epsilon = 0$ .

Note that  $\tilde{z} = \tilde{h} + i\tilde{u}$ . Assuming  $h$  and  $u$  are roughly of the same magnitude, it holds  $|\tilde{z}| \approx 2|\tilde{h}|$ . If we insert the approximation  $\tilde{z} = 2\tilde{h}$  and write the approximations as equations, we obtain

$$\tilde{p} = 2\alpha(\omega(x) - \omega - i\epsilon)\tilde{h} + i \cdot 8\beta|\tilde{h}|^2\tilde{h}. \quad (2.37)$$

The corresponding equation of the model proposed by T. Duke and F. Jülicher [41], formulated in the frequency domain, reads

$$\tilde{p} = \hat{\alpha}(\omega(x) - \omega - i\epsilon)\tilde{h} + i\hat{\beta}|\tilde{h}|^2\tilde{h}. \quad (2.38)$$

By choosing the parameters  $\alpha = \hat{\alpha}/2$ ,  $\beta = \hat{\beta}/8$  we obtain a time model corresponding to the frequency domain model under the assumption  $\tilde{z} = 2\tilde{h}$ . Fig. 2.4 shows the BM response to a pure tone of 1300 Hz for the model in the frequency domain and the time domain. We see that the approximation above is reasonably good. The waves are of similar form and height. There are deviations on the basal side. In the peak region the amplitudes are comparable, in particular for small stimuli. Note that exact agreement of the two models could not be expected due to the approximation above and due to approximating the Fourier transform of  $|h|^2h$  by  $|\tilde{h}|^2\tilde{h}$ .

It is possible to derive an exact formula for the relation between  $\tilde{p}$  and  $\tilde{h}$  if we assume there is a unique positive solution of the cubic equation relating  $|\tilde{p}|$  and  $|\tilde{z}|$ , i.e., we have  $|\tilde{z}|^2 = |\tilde{z}|^2(\tilde{p})$ . Applying the Fourier transformation to Eqs. (2.14) and (2.15), results in

$$i\omega\tilde{h} = -\omega(x)\tilde{u} - \frac{\beta}{\alpha}|\tilde{z}|^2\tilde{h} + \epsilon\tilde{h}, \quad (2.39)$$

$$i\omega\tilde{u} = \omega(x)\tilde{h} - \frac{\beta}{\alpha}|\tilde{z}|^2\tilde{u} - \frac{1}{\alpha}p + \epsilon\tilde{u}, \quad (2.40)$$

where  $|\tilde{z}|^2 = (\tilde{h}^2 + \tilde{u}^2)$ . Solving Eq. (2.39) for  $\tilde{u}$  and Eq. (2.40) for  $\tilde{p}$ , we obtain

$$\tilde{p} = \tilde{h} \frac{\alpha}{\omega(x)} \left( \omega(x)^2 + \left( \epsilon - \frac{\beta}{\alpha}|\tilde{z}|^2 - i\omega \right)^2 \right). \quad (2.41)$$

It is clear that parameter values in this formula cannot be compared directly with parameter values in Eq. (2.38) as for instance even in the linear case  $\beta = \hat{\beta} = 0$  with  $\epsilon = 0$ , the terms are of structurally different form: The difference  $(\omega(x) - \omega)$  is linear in one equation and quadratic in the other.

In the following, we discuss the choice of parameter functions in the frequency domain model [41] as this deepens the understanding of the time domain formulation as well:

In general the Hopf normal form in the frequency domain [25] reads

$$\tilde{p} = A\tilde{h} + B|\tilde{h}|^2\tilde{h}. \quad (2.42)$$

The linear term  $A$  has to vanish at the resonant frequency if the system is at the critical point. The simplest choice of  $A$  ensuring this property is given by the ansatz

$$A = \hat{\alpha}(\omega(x) - \omega). \quad (2.43)$$

$\hat{\alpha}$  can be derived experimentally from the static relation between pressure and vertical BM displacement in the linear case. The parameter  $B$ , which is employed to describe the nonlinearity for frequencies near the resonance frequency, is chosen to be

$$B = i\hat{\beta}, \quad (2.44)$$

where  $\hat{\beta}$  is real, and thus  $B$  is imaginary. By choosing  $A$  purely real and  $B$  purely imaginary it is ensured that there are no spontaneous oscillations corresponding to a non-zero solution of  $\tilde{h}$  for Eq. (2.42) with  $\tilde{p} = 0$  which would be unphysiological. The choice of  $\alpha$  and  $\beta$  turns out to facilitate numerical simulations of the system. Note that for low frequencies this description breaks down as the static response of the cochlea is rather linear.

## 2.5 Determination of incoming and outgoing pressure waves

In order to understand otoacoustic emissions of our model, it is helpful to measure the strengths of forwards and backwards traveling waves at the stapes. For this reason, in the following we determine incoming and outgoing pressure waves of the cochlea model. We perform this analysis both in the frequency and in the time domain.

Thus far we prescribed and fixed the total pressure amplitude  $A$  at the stapes, which are located at  $x = 0$ . However, in experiments the total pressure at  $x = 0$  is not the input presented to the system. In contrast, it is the driving pressure in the ear canal that is fixed. From the ear canal the input pressure is transmitted via the tympanum, the ossicles and the oval window to the inside of the cochlea. These considerations suggest that the input might be more appropriately approximated by the incoming pressure at  $x = 0$  instead of the total pressure at  $x = 0$ , which is a superposition of the incoming and outgoing pressure. For strong driving the total pressure is dominated by the incoming pressure. However, for small pressure amplitudes this does not necessarily hold true due to back reflections from the inside of the cochlea.

In general, incoming and outgoing waves cannot be uniquely determined and thus not distinguished in inhomogeneous media (for an example see [22] or [2], p. 49). The BM is a slowly varying medium where we can assume that there is a unique discrimination of the two directions (see [2] for more details). We assume that at the left end, i.e., in the proximity of  $x = 0$ , the nonlinear term in the oscillator equation can be neglected and thus we are in the linear, passive and homogeneous case where it is possible to uniquely define incoming and outgoing waves.

In the frequency domain for  $\tilde{p}$  in the neighborhood of  $x = 0$ , we make the ansatz

$$\tilde{p}(x, \omega) = p_{in} e^{-i(kx + \phi_{in})} + p_{out} e^{i(kx + \phi_{out})} \quad (2.45)$$

$$\Rightarrow \frac{d}{dx} \tilde{p}|_{x=0} = ik (-p_{in} e^{-i\phi_{in}} + p_{out} e^{i\phi_{out}}), \quad (2.46)$$

where the wave number  $k$  is yet to be determined, and  $p_{in}$  and  $p_{out}$  are the amplitudes of the incoming and outgoing waves in the frequency domain. Employing the two equations above,  $p_{in}$  and  $p_{out}$  can be related to the pressure and its derivative at the boundary as follows:

$$p_{in} = \frac{1}{2} \left| \tilde{p}(x=0) - \frac{1}{ik} \frac{d}{dx} \tilde{p}|_{x=0} \right|, \quad p_{out} = \frac{1}{2} \left| \tilde{p}(x=0) + \frac{1}{ik} \frac{d}{dx} \tilde{p}|_{x=0} \right|. \quad (2.47)$$

In the following, we determine the wave vector  $k$  at  $x = 0$ : For the approximate formulation of the Fourier transform of the model in the time domain, Eq.

(2.37), we obtain  $\tilde{p} = \alpha(\omega(x) - \omega + i\epsilon)\tilde{h}$  in case of  $\beta = 0$ . Consequently, the hydrodynamic equation can be written as

$$\frac{d^2\tilde{p}}{dx^2} = -\frac{2\rho\omega^2}{l}\tilde{h} = -\frac{2\rho\omega^2}{l}\frac{\tilde{p}}{\alpha(\omega(x=0) - \omega + i\epsilon)} \quad (2.48)$$

$$\Rightarrow k = \omega\sqrt{\frac{2\rho}{l\alpha(\omega_0 - \omega + i\epsilon)}}. \quad (2.49)$$

Using the more exact formula (2.41) of the Fourier transform of the time domain model in the linear case, we obtain

$$\frac{d^2\tilde{p}}{dx^2} = -\frac{2\rho\omega^2}{l}\tilde{h} = -\frac{2\rho\omega^2}{l}\tilde{p}\frac{\omega(x=0)}{\alpha(\omega(x)^2 + (\epsilon - i\omega)^2)} \quad (2.50)$$

$$\Rightarrow k = \omega\sqrt{\frac{2\rho\omega_0}{l\alpha(\omega_0^2 + (\epsilon - i\omega)^2)}}. \quad (2.51)$$

This result, which is more precise compared to the value obtained by Eq. (2.49), can be employed to investigate SFOAEs in the frequency domain model.

### 2.5.1 Extracting $p_{in}$ in the time domain

In this section, we address the problem of extracting the amplitude of incoming and outgoing waves in the spatially discretized version of the time domain model. For this we only need to know the trajectories of the two left-most oscillators  $p(x=0, t), p(x=L/N, t)$ . We abuse notation by using  $p_0$  for describing the amplitude of the pressure at  $x=0$  instead of the pressure itself.

We assume that in the vicinity of  $x=0$  we are able to make the ansatz

$$p(x, t) = \frac{1}{2} \left[ p_0^+ e^{i(kx - \omega t + \phi_+)} + p_0^+ e^{-i(k^*x - \omega t + \phi_+)} + p_0^- e^{i(-kx - \omega t + \phi_-)} + p_0^- e^{-i(-kx - \omega t + \phi_-)} \right], \quad (2.52)$$

where  $p_0^+$  and  $p_0^-$  denote the amplitudes of incoming and reverse pressure, respectively. Note that pressures are always real. We describe the pressure at position  $x=0$  by a (real valued) oscillation of frequency  $\omega$ , amplitude  $p_0$  and phase  $\phi_0$ . Thus, we can write

$$p(x=0, t) = \frac{p_0}{2} \left( e^{i(\phi_0 - \omega t)} + e^{i(-\phi_0 + \omega t)} \right). \quad (2.53)$$

The pressure at  $x=0$  is a superposition of incoming and outgoing waves,

$$p_0 e^{i\phi_0} = p_0^+ e^{i\phi_+} + p_0^- e^{i\phi_-}. \quad (2.54)$$

Analogously, we obtain

$$\partial_x p|_{x=0} = \frac{p_\Delta}{2} \left( e^{i(\phi_\Delta - \omega t)} + e^{i(-\phi_\Delta + \omega t)} \right), \quad (2.55)$$

$$p_\Delta e^{i\phi_\Delta} = k \left( p_0^+ e^{i(\phi_+ + \pi/2)} - p_0^- e^{i(\phi_- + \pi/2)} \right). \quad (2.56)$$

Eq. (2.54) gives us  $p_0^- e^{i\phi_-} = p_0 e^{i\phi_0} - p_0^+ e^{i\phi_+}$  which we insert into Eq. (2.56).

$$\begin{aligned} p_\Delta e^{i\phi_\Delta} &= k \left( 2p_0^+ e^{i(\phi_+ + \pi/2)} - p_0 e^{i(\phi_0 + \pi/2)} \right) \quad (2.57) \\ \Rightarrow p_0^+ &= \frac{1}{2} e^{-i(\phi_+ + \pi/2)} \left( \frac{p_\Delta}{k} e^{i\phi_\Delta} + p_0 e^{i(\phi_0 + \pi/2)} \right) \\ &= \frac{1}{2} \sqrt{\left( \frac{p_\Delta}{k} \cos(\phi_\Delta) - p_0 \sin(\phi_0) \right)^2 + \left( \frac{p_\Delta}{k} \sin(\phi_\Delta) + p_0 \cos(\phi_0) \right)^2}. \quad (2.58) \end{aligned}$$

The last equation follows because  $p_0^+$  is real by definition. Similarly, we obtain

$$\begin{aligned} p_0^- &= \frac{1}{2} e^{-i(\phi_- + \pi/2)} \left( -\frac{p_\Delta}{k} e^{i\phi_\Delta} + p_0 e^{i(\phi_0 + \pi/2)} \right) \\ &= \frac{1}{2} \sqrt{\left( -\frac{p_\Delta}{k} \cos(\phi_\Delta) - p_0 \sin(\phi_0) \right)^2 + \left( -\frac{p_\Delta}{k} \sin(\phi_\Delta) + p_0 \cos(\phi_0) \right)^2}. \quad (2.59) \end{aligned}$$

The value of  $k$  can be calculated from the model. The quantities  $p_0$  and  $\phi_0$  are input variables and thus also known. The values of  $p_\Delta$  and  $\phi_\Delta$  can be determined by Fourier transforming  $(p(L/N, t) - p(0, t))/\Delta x \approx \partial_x p(x=0, t)$ , taking one cycle as data set for the transformation. This gives a time-dependent value for the reflection coefficient  $R = p_0^-/p_0^+$ , which can be used for the analysis of SFOAEs of the model in the time domain and in general for similar time domain models of inhomogeneous, slowly varying media. However, we do not apply this analysis to the model as there exists a middle ear boundary condition, introduced in chapter 3, which corresponds better to the experimental setup than the boundary condition at  $x=0$  which we employed here.

## 2.6 Low frequency modes

In the time domain model of the cochlea which we presented in the previous sections, two slow modes are present. In the following, we show that the lower mode is the fundamental mode of the system, and the one with the higher frequency is the first harmonic of the lower one. This is done by means of calculating an approximate formula for the fundamental mode. We compute the frequency of the fundamental mode for a string and apply the obtained results to the BM.

Consider a string of length  $L$  with fixed boundary conditions. The fundamental mode possesses the wave length  $\lambda_0 = 2L$ . We want to calculate the frequency  $\nu_0$  of the fundamental mode. Let the wave equation of the string be given by

$$\partial_t^2 y = c^2 \partial_x^2 y, \quad (2.60)$$

where  $y$  is the displacement in the vertical direction, and  $c$  is the speed of the wave. For now we assume  $c$  is a constant. Solutions of the above equation are given by  $f(x - ct)$  and  $g(x + ct)$  for arbitrary two times differentiable functions  $f, g$ . It holds  $c = \nu_0 \lambda_0 \Rightarrow \nu_0 = \frac{c}{\lambda_0} = \frac{c}{2L}$ . By writing  $c = \frac{L}{T}$ , where  $T$  is the time the wave needs to travel the distance  $L$ , we obtain

$$\nu_0 = \frac{1}{2T}. \quad (2.61)$$

In summary, for given  $c$  and  $L$ , it is possible to calculate  $T$  and consequently  $\nu_0$ .

In the following, we exploit this result for the calculation of the fundamental mode of the BM. First, we calculate  $c(x)$  of the BM, where  $c(x)$  is a non-constant,  $x$ -dependent function. Knowing  $c(x)$ , we can determine  $T$ , which enables us to compute the frequency  $\nu_0$  of the fundamental mode of the BM.

The hydrodynamic equation (2.6) of the cochlea reads  $\partial_t^2 h = \frac{l}{2\rho} \partial_x^2 p$ . In the linear, passive approximation for the static deflections it holds  $p = \alpha\omega(x)h$ . Inserting this relation into the hydrodynamic equation, results in

$$\partial_t^2 p = \frac{\alpha\omega(x)l}{2\rho} \partial_x^2 p \quad (2.62)$$

and hence

$$c(x) = \sqrt{\frac{\alpha\omega(x)l}{2\rho}}, \quad (2.63)$$

where  $c(x)$  is the local, position dependent wave propagation velocity. We assume the existence of wave functions  $f(x - c(x)t)$  and  $f(x + c(x)t)$  which solve Eq. (2.62) approximately and travel forward and reverse, respectively, with velocity  $c(x)$ .

For an object moving in longitudinal direction, let  $X(t)$  denote the value of its longitudinal position  $x$  at time  $t$ . The velocity as a function of time is given by  $\frac{dX(t)}{dt}$ . Defining  $c(x)$  as the velocity as function of location (assuming the object moves only in one direction), we obtain  $c(x(t)) = \frac{dX(t)}{dt}$ . The time  $T$  the object needs to travel from  $x = 0$  to  $x = L$ , is given by

$$T = \int_0^T 1 dt = \int_{X(0)}^{X(T)} \frac{dt}{dx} dx = \int_0^L \frac{1}{c(x)} dx. \quad (2.64)$$

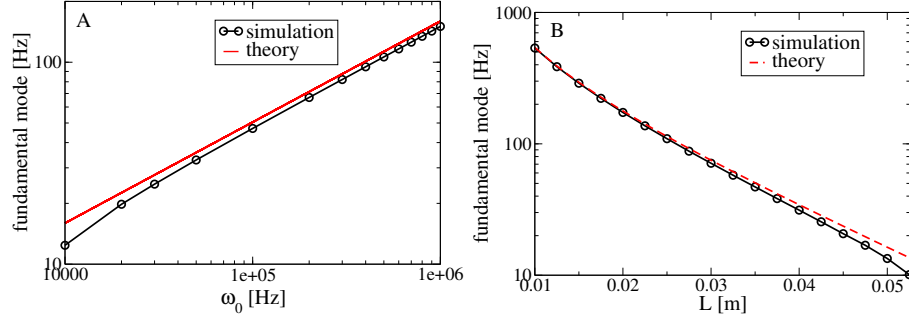


Figure 2.5: Comparison between the simulation results (black lines) and theoretical predictions (red lines) of the frequency of the fundamental mode. A: The frequency of the fundamental mode is plotted as a function of  $\omega_0$ . The standard parameter value is given by  $\omega_0=10^5$  Hz. B: The frequency of the fundamental mode is plotted as a function of  $L$ , the length of the cochlea, where  $L=35$  mm is the standard length.

Combining this relation with Eq. (2.63), we obtain

$$T = \int_0^L \frac{1}{c(x)} dx = \sqrt{\frac{2\rho}{\alpha\omega_0 l}} \int_0^L e^{\frac{x}{2a}} dx = \sqrt{\frac{2\rho}{\alpha\omega_0 l}} 2a \left( e^{\frac{L}{2a}} - 1 \right). \quad (2.65)$$

Thus, the frequency of the fundamental mode of the BM reads

$$\nu_0 = \frac{1}{2T} = \frac{\sqrt{\alpha\omega_0 l}}{4\sqrt{2\rho}d \left( e^{\frac{L}{2a}} - 1 \right)}. \quad (2.66)$$

The theoretical value of  $\nu_0$  for the time domain model according to the equation above reads  $\nu_0 = 50.5$  Hz. Simulations of the system, employing the boundary conditions  $p(x=0) = 0$  and  $p(x=L) = 0$ , give  $\nu_0 = 47.0$  Hz. In order to verify the theoretical approximation, the model is simulated for varying  $\omega_0$  and  $L$ , for which the frequency of the fundamental mode is measured. There is a good agreement between the theoretical prediction and simulation results, see Fig. 2.5, which becomes better for high maximal angular eigenfrequencies  $\omega_0$  and large cochlea lengths  $L$ . In both cases the agreement becomes better for increasing frequencies  $\nu_0$  of the fundamental mode.

The boundary conditions at the helicotrema and the apex are fixed in terms of  $p$  as the pressure differences vanish. Note that due to the vanishing pressures, the BM motion at the boundaries is rather small and we can consider the boundary conditions to be approximately fixed in terms of  $h$  as well. The fundamental mode also visible as a pronounced peak in the power spectrum of the pressure in the ear canal if we use the boundary condition proposed in the subsequent chapter. In this case, the frequency of the fundamental mode is reduced to

about 36 Hz and two higher harmonics are visible.

Note that the theoretical approximation above is only valid if  $\nu_0$ , the frequency of the fundamental mode, is lower than the lowest characteristic frequency on the BM, which is the case all data points in Fig. 2.5. This ensures that the wave is always propagating and not decaying at some point. This would be the case for frequencies which are higher than the eigenfrequency on the BM, because the factor  $c(x)$  in the wave equation would become negative for  $x$  larger than the resonance point  $x_r$ , leading to an exponentially decaying wave solution. This is visible in the WKB approximation, which we considered previously.



## Chapter 3

# Effects of boundary conditions, longitudinal coupling and static disorder

In the previous chapter, we presented a simple and generic model of the cochlea. Now we advance towards a more biophysical description in order to study evoked and spontaneous cochlear activity, in particular phenomena such as stimulus frequency otoacoustic emissions, which we abbreviate with SFOAEs, and SOAEs. In section 3.1 we incorporate a new boundary condition taking into account middle ear mechanics. We describe the middle ear acting as a harmonic oscillator. This provides a natural way to implement a boundary condition, which corresponds well to the experimental setup, where the cochlea is stimulated by a driving pressure in the ear canal. Furthermore, this boundary condition ensures that the pressure in the ear canal is an observable, which is vital in order to compare model results with experiments. Section 3.2 determines the response of the model to sinusoidal stimuli. These SFOAEs are an important measure in the field of mechanics of hearing, and they are connected to other observables such as SOAEs, which we will investigate further in chapter 4. Section 3.3 investigates the problem of determining the bifurcation point of the global system. For a single Hopf oscillator this point is located at  $\epsilon = 0$ , but for the global system this does not have to remain true. Subsequently, we add dynamical noise, which accounts for intrinsic fluctuations of the oscillatory elements, representing diverse forces acting on the BM. The issue of longitudinal coupling is addressed in 3.4, where we gather experimental results and study the effect of longitudinal coupling on the model. In section 3.5, we perturb parameters and investigate if it suffices to introduce disorder in the parameters to cause the generation of SOAEs. It turns out that disorder in the frequency gradient  $\omega(x)$  or the nonlinearity  $\beta$  is not sufficient. Solely disorder in the bifurcation parameter is sufficient to provoke SOAEs.

After introducing longitudinal coupling and dynamical noise, the full equation for the local oscillator dynamics is given by the following generalized complex Ginzburg-Landau equation:

$$\partial_t z = (\epsilon(x) + i\omega(x))z - \frac{\beta}{\alpha}|z|^2 z + (\kappa + i\kappa')\partial_x^2 z - \frac{i}{\alpha}p + \xi(x, t), \quad (3.1)$$

where  $\epsilon(x)$  is the bifurcation parameter (which we will choose to be position-dependent in chapter 4),  $\kappa, \kappa'$  denote the dissipative and elastic coupling, respectively. The dynamical noise, represented by  $\xi(x, t)$ , is chosen to be a zero-mean Gaussian noise which is white in both space and time.

### 3.1 Dynamic boundary condition mediated by the middle ear

Thus far we have only modeled the inner part of the ear. However, despite the fact that the active inner ear contains the key elements of cochlear mechanics, the outer and in particular the middle ear, which are both essentially passive, are also integral components of the auditory system and contribute substantially to the hearing process by transmitting acoustic energy into the cochlea. The fluid-filled cochlea is not directly connected to the outer environment. The transmission to and from the outer environment is mediated by the middle ear, which is an air-filled cavity comprising the three bones (see Fig. 3.1 A), and by two membranes: The tympanum and the oval window separate the middle ear from other parts of the ear. They are connected via a lever-like construction composed of the ossicles, namely the incus, malleus and the stapes. The lever joint is fixated via the muscular system and ligaments, and it is driven by two forces acting on them both from the outside via the tympanum and from within the cochlea via the oval window.

The main function of the middle ear is widely believed to be matching impedances [5, 55]. Put differently, the task of the middle ear is connecting the air-filled ear canal with the fluid-filled cochlea in such a way that transmission losses due to reflections at the boundaries are minimized. Small pressure amplitudes at the tympanum are transformed to high pressure intensities at the oval window. This is achieved by two factors introducing a mechanical gain: The area of the tympanum is more than an order of magnitude larger than the oval window, and the ossicles act like a lever with two different lever arm lengths, built such that large motions of the tympanum are transformed into small motions at the oval window. The presence of the middle ear allows for a transmission of approximately 60% of incoming sound energy into the cochlea. Without impedance matching, i.e., if the oval window was directly connected to the outer environment, less than 0.1% of the acoustic energy would be transmitted, and consequently over 99.9% would be reflected back [5].

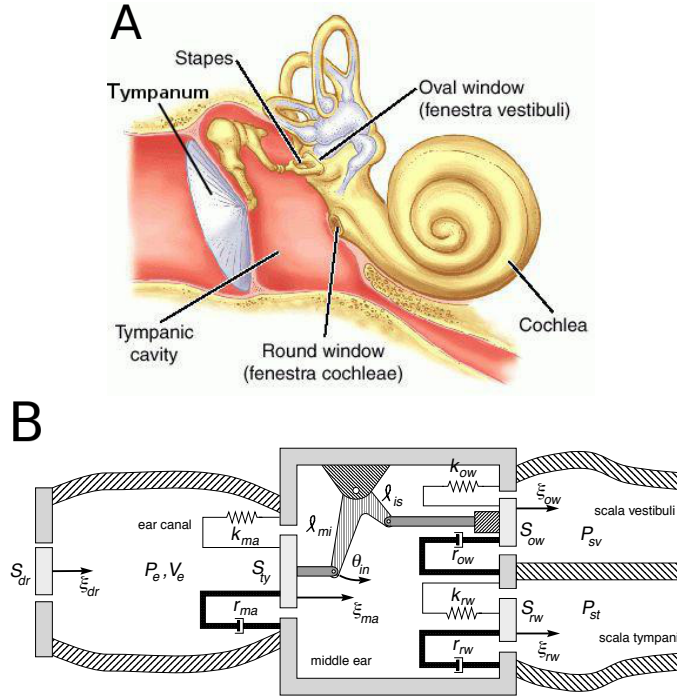


Figure 3.1: A: Sketch of the human middle ear. Modified from [39]. B: Sketch of the middle ear model. The calibrated driving pressure drives the middle ear via  $\xi_{dr}$ . In the ear canal of volume  $V_e$  the pressure is denoted by  $p_e$ . The ossicles are represented by a lever with two lever arms, whose lengths are  $\ell_{mi}$  and  $\ell_{is}$ , and two surfaces at the respective ends, the tympanum with area  $S_{ty}$ , and the oval window with area  $S_{ow}$ . Graph adopted from [148].

However, this is only a simplified picture of the middle ear, as the dynamics of this system are complex and strongly frequency-dependent. Note that the precise mechanism of middle ear dynamics is not yet fully understood and the subject of active research [120]. For instance, it is not entirely clear why the middle ear transmission factors in forward and reverse direction as a function of frequency are neither shifted nor reciprocal versions of each other [119, 154, 37, 38].

In this section, we employ a different boundary condition for the base resulting from hydrodynamic considerations. Subsequently, we present a middle ear model which is based on the representation of the middle ear as a lever, thus acting as a system with one degree of freedom, driven from two oppositional sides. The boundary condition as well as the model of the middle ear stem from Talmadge et al. [148].

The boundary condition results from the following considerations: Balance of inertial forces and resulting external forces at the base inside the cochlea give us, as in section 2.1,  $\rho\partial_t J_1 = -bl\partial_x P_1(0, t)$  and  $\rho\partial_t J_2 = -bl\partial_x P_2(0, t)$ . As  $J_2 = -J_1$  and thus  $2J_1 = j$  we obtain  $\rho\partial_t j_0(t) = -bl\partial_x p(0, t)$ , where  $j_0(t) = 2J_1(x = 0, t)$ . Spatial discretization gives

$$\rho\frac{d}{dt}j_0(t) = -bl\frac{p_1(t) - p_0(t)}{\Delta x}, \quad (3.2)$$

where we define  $p_0(t) = p(x = 0, t)$  and  $p_1(t) = p(x = \Delta x, t)$ . The volume flow at the base is dominated by the movements of the oval window (see the discussion at the end of this section for a detailed justification). Let  $q$  denote the displacement in longitudinal direction of the the oval window, where a positive  $q$  corresponds to a motion towards the inside of the cochlea. Neglecting contributions from movements of  $h_0$ , we attain  $J_1 \approx S_{ow}\frac{d}{dt}q(t)$ . Consequently, we arrive at the condition

$$p_1(t) - p_0(t) = -2\frac{\rho S_{ow}\Delta x}{b\ell}\frac{d^2}{dt^2}q. \quad (3.3)$$

This is the boundary equation we use henceforth in this thesis. It remains to determine the dynamics of  $q$ .

According to Talmadge, we model the middle ear as a lever, thus assuming a single degree of freedom, i.e., making the ansatz that ossicles and membranes move as one, see Fig. 3.1 B. The dynamics of the middle ear are described by a harmonic oscillator with the variable  $q$ . The effective areas of the oval window and tympanum are represented by  $S_{ow}$  and  $S_{ty}$ , respectively. We assume that the oval window and the tympanum move in piston-like manner. The oval window is subject to the force  $S_{ow}p_0$  from the inside of the cochlea and the force  $\Gamma_{mi}S_{ty}p_e$  due to pressure variations in the ear canal.  $\Gamma_{mi}$  is the lever factor, resulting from the ratio of the lever arm lengths, and  $p_e$  is the pressure in the ear canal. Thus, we arrive at

$$m\frac{d^2}{dt^2}q + \gamma\frac{d}{dt}q + m\omega_{ow,e}^2q = -S_{ow}p_0(t) + \Gamma_{mi}S_{ty}p_e(t), \quad (3.4)$$

where  $m, \gamma$  and  $\omega_{ow,e}$  are the mass, damping constant and eigenfrequency of the middle ear, which can be estimated by physiological data and a more biophysical middle ear model. See table 3.1 for parameter values. We make the simplification that the pressure in the ear canal is uniform and can be described by a single variable  $p_e$ . The minimal wavelength of SOAEs, which corresponds to the upper bound of 8 kHz in terms of reported SOAE frequencies, is about two times larger than the length of the ear canal. However, note that the outer ear exhibits a resonance at about 3 kHz [117].

In general, pressure is understood to be not the absolute pressure but rather the difference to the ambient pressure. In this section, this convention applies to  $p_e$  and  $p_{dr}$ . Also note that sound pressure waves in the air are very small

compared to the ambient pressure, typically at least 5 orders of magnitude lower in pressure amplitude.

Eq. (3.4) has the drawback that we have to insert  $p_e$  as an input variable. We would rather use  $p_e$  as an observable like in experiments. In order to achieve this, we introduce  $p_{dr}$ , the calibrated driving pressure, and relate the ear canal pressure to the driving pressure:  $p_{dr}$  is defined to be the pressure which is present in the ear canal if the tympanum is fixed to its rest position. The compression of the air in the ear canal can be assumed to be adiabatic, i.e., to happen without exchange of energy with the surrounding environment. This holds true for fast processes. In the case of acoustic stimulation in the ear canal the assumption is approximately fulfilled. For an adiabatic processes,  $PV^{\gamma_{air}} = \text{const}$  or equivalently  $dP = -\gamma_{air}P\frac{dV}{V}$ , where  $\gamma_{air}$  is the ratio of specific heats,  $V$  is the volume, and  $P$  the pressure. By applying this to our setup, we obtain  $dP = p_e - p_{dr}$  and  $dV = S_{ty}\Gamma_{mi}q$ , where  $V = V_e$  is the volume of the ear canal, and  $P = P_e^0$  is the ambient air pressure in the ear canal. Employing the relation for adiabatic processes, we attain

$$p_e(t) = p_{dr}(t) - \frac{\gamma_{air}P_e^0 S_{ty}\Gamma_{mi}}{V_e}q(t). \quad (3.5)$$

Inserting this result into Eq. (3.4) leads to

$$m\frac{d^2}{dt^2}q + m\gamma\frac{d}{dt}q + m\omega_{ow}^2q = -S_{ow}p_0(t) + \Gamma_{mi}S_{ty}p_{dr}(t), \quad (3.6)$$

where  $\omega_{ow}^2 = \omega_{ow,e}^2 + \gamma_{air}P_e^0 S_{ty}^2 \Gamma_{mi}^2 / (mV_e)$ . Eq. (3.3) provides the dynamics of  $q$ , necessary for employing Eq. (3.6). Taken together, these two equations provide a boundary condition where the input is given by the calibrated driving pressure  $p_{dr}$ . As in experiments, the pressure in the ear canal,  $p_e$ , is an observable via Eq. (3.5). For the case of SOAEs, by definition  $p_{dr} = 0$ , and thus  $p_e$  is proportional to the oval window displacement  $q$ .

Henceforth, we will use this boundary condition together with the dynamics for  $q$  and the equation for the ear canal pressure, Eq. (3.5). Employing this boundary condition also influences the response to pure tones. Furthermore, we will use a modified value for the nonlinearity  $\beta = 4 \cdot 10^{23} \text{ Pa/m}^3$  which in the new setup corresponds better to the BM deflection amplitudes in the frequency domain model than with the previously chosen value of  $\beta$ .

Table 3.1: List of parameters used for the model that includes the middle ear boundary condition

Parameter	Definition	Value
$b$	average breadth of BM	1.1 mm
$\beta$	nonlinearity	$4 \cdot 10^{23}$ Pa/m <sup>3</sup>
$\Gamma_{mi}$	lever factor	1.3
$\gamma_{air}$	specific heat ratio of air	1.4
$\gamma_{ow}$	middle ear damping	0.0295 N s m <sup>-1</sup>
$l$	height of upper/lower chamber	1 mm
$m$	mass of middle ear	0.059 g
$P_e^0$	ambient pressure in ear canal	10 <sup>5</sup> Pa
$S_{ow}$	area of oval window	3.2 mm <sup>2</sup>
$S_{ty}$	area of tympanum	49 mm <sup>2</sup>
$\omega_{ow}$	eigenfrequency of middle ear	$2\pi \cdot 1500$ Hz
$V_e$	volume of ear canal	160 mm <sup>3</sup>

*Discussion of the middle ear model and its limitations.*

In order to verify the earlier assumption that the volume flow at the base is dominated by oval window movements, we compare the change of volume flow at  $x = 0$  caused by the oval window longitudinal displacement  $q$  with the change of flow caused by  $h_0$ , the vertical displacement of the BM at  $x = 0$ . This is done by comparing  $S_{ow} \frac{d}{dt} q$ , where  $S_{ow}$  is the area of the oval window, to  $b \Delta x \frac{d}{dt} h_0$ . It holds  $S_{ow} = 3.2 \cdot 10^{-6}$  m<sup>2</sup>,  $b \Delta x = 1.1 \cdot 10^{-8}$  m<sup>2</sup>, which gives a 300-fold difference in areas. Simulations show that the amplitude of the motion of  $h_0$  exceed the magnitude of the movements of  $q$  by not more than a factor of 20 for frequencies up to 4kHz. Thus, the contribution of the oval window dominates the volume flow at the stapes.

We represent the middle ear by a harmonic oscillator driven by two forces. This model captures essential physical principles of the middle ear and facilitates comparison with experiments by providing a setup that corresponds well to the experimental setup when measuring otoacoustic emissions. However, the model also includes several simplifications. Experimental results show that in certain respects the middle ear is more complex. The lever joint in real cochleae is not fixed but can move. For high frequencies, the ossicles move in a considerably more complicated manner than a lever [5]. Moreover, the piston-like motion of the two membranes is only an idealization which is not met in reality. However, note that in the model we use effective areas of the membranes to take this fact into account. In addition, complex modes of membrane motion were observed in experiments [120]. Furthermore, the assumption of a uniform pressure in the ear canal is not satisfied for high frequencies. External ear canal resonance was reported to be at about 3 kHz [20]. The model is also too simple regarding

its transmission properties. Forward and reverse transmission of the middle ear are not reciprocal, nor are they shifted versions of each other. The transmission behavior of the middle ear is considerably more complex than that of a harmonic oscillator and is strongly dependent on frequency [119]. The loads of the cochlea and the ear canal are very different, which influences measurements of forward and reverse transmission. Moreover, the umbo, which is the notch with which the tympanic membrane is mainly moving, does not behave symmetrically with respect to the direction of stimulation [38].

Forward transmission properties are expected to influence the cochlear response to pure tones and other incoming sounds. Reverse transmission and ear canal resonance are likely to have an effect on different distributions of SOAEs, in particular the statistics of emission frequencies.

Finally, note that the oval window in the model is in a different angle and position relative to the cochlea than what is observed experimentally, see Fig. 3.1 A. Due to the incompressibility of the fluid and the encapsulated structure of the inner ear, the angle is assumed to not alter the physics of the system significantly. Furthermore, in our one-dimensional model we describe the pressure difference as a scalar quantity, for which the angle of stimulation is not essential.

However, the detailed view of the cochlear architecture can explain parameter values which might seem paradoxical: The effective area of the oval window, which impinges on the apical side of the upper chamber, is about three times larger than the average cross-sectional area of the upper chamber. This can be understood by Fig. 3.1 A and the fact that the experimental cross-sectional area of the upper chamber is not constant as we assume in our model but increases for locations closer to the stapes. Note that the area of the oval window is slightly larger than the cross-sectional area of the upper chamber at the base.

## 3.2 Stimulus frequency otoacoustic emissions

The response of the cochlea to pure tone stimulations is an important observable to describe the behavior of the auditory system. It is of particular interest to study the BM deflection and the magnitude of the total or outgoing pressure waves in the ear canal. The pressure responses to pure tone stimuli, measured in the ear canal, are the SFOAEs. These quantities can be studied by analyzing the Fourier transforms of the pressure time traces in the cyclo-stationary state, considered at the driving frequency. Typically, the cochlear response is measured as a function of driving frequency. Remarkably, SFAOEs exhibit connections to SOAEs, which we address below.

Fig. 3.2 A shows typical SFOAE curves of one ear for different stimulus amplitudes. We observe three striking features: Firstly, the amplitude of the response decreases slowly for increasing frequency, rather independent of stimulus amplitude. Secondly, the fine-structure of these SFOAE curves comprises fast oscillations with a regular spacing on top of the slowly varying decrease. Thirdly, note that the fast oscillations decrease in size for increasing stimulus

amplitude. The fast oscillations of the experiment show a surprising regularity. Let  $\Delta f = f_2 - f_1$  denote the difference between two maxima at  $f_1$  and  $f_2$  of an

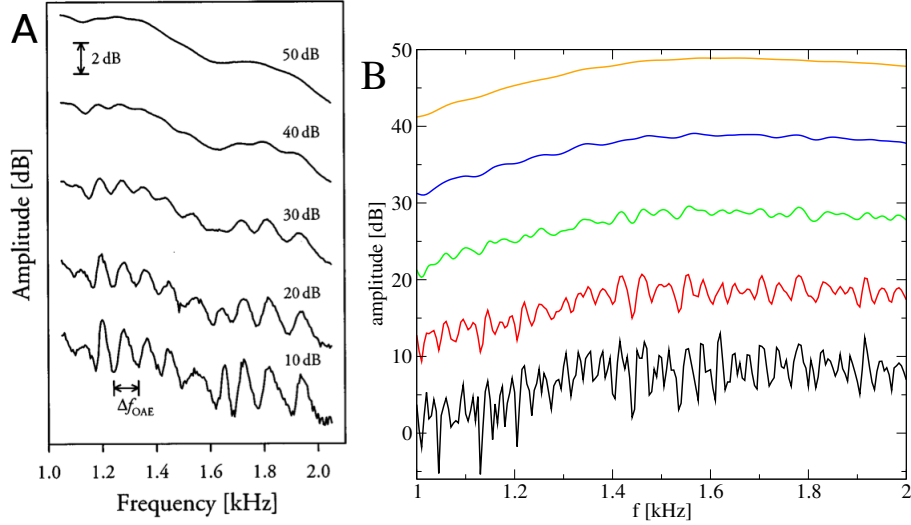


Figure 3.2: The total sound pressure amplitude at the driving frequency, measured in the ear canal during a stimulation with a pure tone, plotted as a function of driving frequency. A) shows experimental results for one ear and different stimulus amplitudes. Adopted from [136]. B) displays the result of the model for a stimulus amplitude of the same dB levels as in A). The system was simulated with  $\tilde{\omega}(x) = \omega(x)(1 + \nu(x))$ , where  $\nu(x)$  is white Gaussian noise with zero mean and a standard deviation of 0.01. All curves were simulated with the same realization of the perturbation  $\tilde{\omega}$ . The amplitudes of the stimulus for the different curves are 10 (black), 20 (red), 30 (green), 40 (blue), and 50 dB SPL (orange).

SFOAE curve as depicted in 3.2 A, and  $f = \sqrt{f_1 f_2}$  their geometric mean. For experiments it holds true that

$$\frac{\Delta f}{f} \approx \frac{1}{15}. \quad (3.7)$$

Consequently, for frequencies around 1500 Hz this corresponds to a spacing of 100 Hz. The relative distance of 1/15 has also been found to be the preferred minimal distance between neighboring SOAEs. Note that this value changes slightly as a function of frequency, and a value of  $\Delta f/f = 1/17$  was also reported, corresponding to a distance of one semitone. On basis of theoretical considerations, it was hypothesized that small, random irregularities in parameters, for instance in the frequency gradient  $\omega(x)$ , can be responsible for this

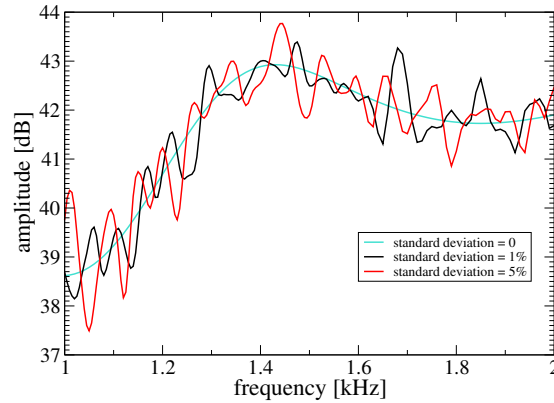


Figure 3.3: The total sound pressure amplitude in the ear canal, measured as the value of the Fourier transform evaluated at the driving frequency, during a stimulation of 5 s with a pure tones of 40 dB, plotted as a function of varying frequency for three different standard deviations of the perturbation of  $\omega(x)$ .

pattern [161]. Indeed, we see in Fig. 3.3 that the SFOAE curve of the model does not contain fast oscillations for a smooth, unperturbed  $\omega(x)$ . By perturbing  $\omega(x)$  with white Gaussian noise we obtain fast oscillations. For a driving amplitude of 40 dB, the frequency of the fast oscillations are of the order of the ones in experiments. However, they do not exhibit the high regularity observed in experiments. Fig. 3.2 B shows the SFOAE response of the model for varying amplitudes. The SFOAE curves of the model are of a different overall shape compared to experimental data, first they increase until at around 1.6 kHz where they start decreasing. The maximum at 1.6 kHz is presumably partly due to the presence of the harmonic oscillator which represents the middle ear and has an eigenfrequency of 1.5 kHz. The frequency of the fast oscillations for low stimulus amplitudes is too high. For medium stimuli, the oscillations are of a similar frequency, as visible in Fig. 3.3. As in experiments, the fast oscillations vanish for higher stimulus amplitudes, shown in Fig. 3.2.

One explanation of the fine-structure and its relation to SFOAEs has been provided on theoretical grounds by G. Zweig and C.A. Shera [161, 137], putting forward the idea of coherent reflection filtering which describes the cochlea as an analog of a laser with certain modes, i.e., global standing waves. In a nutshell, the explanation of the regular oscillations is based on roughness of some parameter, for instance the frequency gradient. Random irregularities of the before smooth frequency gradient  $\omega(x)$  act as a source of reflection, leading to regular spacings in the SFOAE curves. The fact that the fine-structure disappears for large stimulation amplitudes is explained by the claim that for high input intensities the traveling wave is reflected over a broad range of the cochlea, resulting in non-coherent reflections. This hypothesis serves as a possible answer for both the periodicity in SFOAEs and SOAEs, where one also observes a characteristic

minimal distance of  $1/15$  between neighboring SOAEs.

According to the theory sketched above, SOAEs are a global collective phenomenon in contrast to local autonomous oscillations. We will investigate this question further in section 3.5.

### 3.3 Spontaneous activity of the system

In this section, we ask under which conditions the model exhibits spontaneous activity, measured in terms of pressure fluctuations in the ear canal. Single dynamical systems governed by the Hopf normal form exhibit spontaneous oscillations if and only if the bifurcation parameter is positive, i.e., in the unstable regime. Although our model comprises a chain of coupled oscillators described by the Hopf normal form, the global bifurcation point  $\epsilon_{crit}$  of the model does not have to coincide with the bifurcation point of an individual oscillator, which is located at 0. Indeed, it turns out that the global system possesses a small but non-zero value  $\epsilon_{crit} > 0$ . However, the transients are too long to precisely determine the exact value. Furthermore, there is a spatial dependence of the activity. The model is most insensitive to overcritical oscillators placed in the middle of the cochlea. The measure we employ for spontaneous activity is chosen to be the variance of the pressure in the ear canal.

Relaxation times of the system become rather large near the global critical point  $\epsilon_{crit}$  of the system, similar to the diverging relaxation rate for a single Hopf oscillator near the critical point. Thus, we choose to approximate  $\epsilon_{crit}$  by means of a method which is similar to procedures employed in case of hysteresis but which is solely due to transients: We equip all oscillators of the model with a constant  $\epsilon_{global} = -1$ , thus locating them in the stable regime, except for two neighboring oscillators which possess a high  $\epsilon_{loc} > 0$ . We simulate the model for a period  $T_{sim}$  and measure the variance of  $p_e$ . Subsequently, we vary the parameter  $\epsilon_{loc}$  for the two selected neighboring oscillators. Starting from a high value,  $\epsilon_{loc}$  is first decreased multiple times and then increased again. This leads to curves like the one depicted in Fig. 3.4, where we start from high values on the right, proceed to low values on the left, and then move to the right by increasing  $\epsilon_{loc}$  again. By choosing a threshold, which corresponds to the reference pressure of 0 dB SPL, and determining the  $\epsilon_{loc}$ -values for which the threshold value is reached, we can infer an estimate of upper and lower bounds of  $\epsilon_{loc}$  of the two oscillators for which the system becomes active.

By carrying out this procedure for different positions of the active oscillators we obtain an estimate of  $\epsilon_{crit}$  as a function of  $x$ , as displayed in Fig. 3.5. The model is most insensitive to active oscillators positioned in the middle of the cochlea, corresponding to intermediate frequencies. The apical part of the BM is easier excitable than the basal portion and exhibits higher magnitudes of spontaneous oscillation in the presence of noise. However, the basal end is closer to the ear canal, thus transmission might be facilitated in comparison to low frequencies.

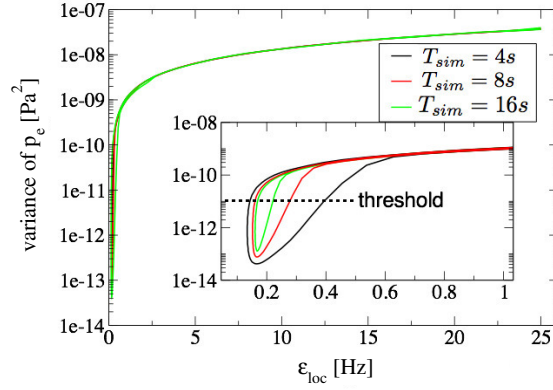


Figure 3.4: The variance of  $p_e$  shown as a function of  $\epsilon_{loc}$  for three different simulation times: 4 s (black), 8 s (red), and 16 s (green). For a given value of  $\epsilon_{loc}$ , we simulate the system for a period  $T_{sim}$ , measure the variance of  $p_e$  and then change the parameter  $\epsilon_{loc}$ . Starting from a high value of  $\epsilon$ , it is first decreased and then increased again. The threshold corresponds to the reference pressure of 0 dB SPL.

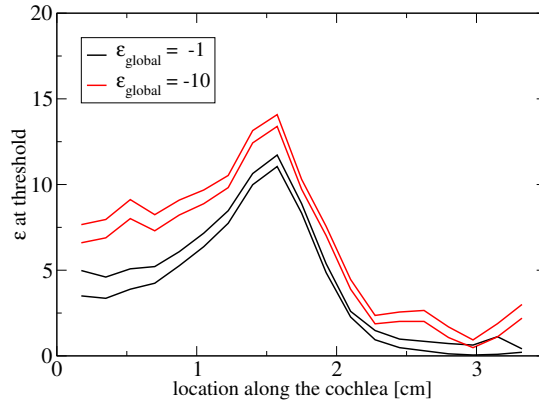


Figure 3.5: Upper and lower bounds of  $\epsilon_{loc}$  as a function of the position of the two neighboring overcritical oscillators for a system size of  $N = 100$ , for two different values of  $\epsilon_{global}$ . The black lines denotes  $\epsilon_{global} = -10$  Hz, the red lines indicate  $\epsilon_{global} = -1$  Hz. Similar results are obtained for other choices of  $N$ .

Note that we chose a local threshold criterion for determining activity of the global system, namely the pressure in the ear canal, i.e., the pressure next to the basal end of the cochlea. The two above mentioned competing effects, the vicinity to the base and an easier excitability, might lead to the maximum observed in Fig. 3.5.

### 3.4 Longitudinal coupling of oscillators

In this section, we are concerned with longitudinal coupling of the BM. We review experimental findings and study the effects of longitudinal coupling on the model.

There is contradictory findings about the nature and relevance of longitudinal coupling in the organ of Corti. In 1960, experiments by Békésy led to the conclusion that there is non-negligible longitudinal coupling in cadaver cochleae [14]. In contrast to Békésy's results, Voldrich found in 1978 that for live guinea pig cochleae longitudinal coupling can be discarded and that the organ of Corti is organized as a system of parallel fibers [153]. However, a more recent experimental investigation in 2001 found that longitudinal coupling in living cochleae is indeed significant [104, 105], in accordance with the results obtained by Békésy. The strength of the longitudinal coupling may be irrelevant in some respects, as for instance in case of SFOAEs with high stimuli, but relevant in others, for instance for SOAEs. It was shown experimentally and theoretically that coupling reduces the influence of noise on hair cells and thus enhances nonlinear amplification [35, 36, 9], leading to a possible explanation to the question of why the entire cochlea is more sensitive than its key individual constituents, the hair cells. Additionally, it was found that longitudinal coupling of active Hopf oscillators can lead to the formation of synchronized clusters of oscillators. Thus, longitudinal coupling provides a possible mechanism for the separation of SOAEs and the characteristic minimum distance between neighboring SOAEs [152], as mentioned in the sections 1.1 and 3.2.

We introduce next-nearest neighbor coupling in the model. In its continuum formulation the local oscillator dynamics including coupling is given by Eq. (3.1). The response of the model to longitudinal coupling is displayed in Fig. 3.6. Introducing elastic coupling leads to a similar shape of the power spectrum but with shifted frequencies of the small peaks in Fig. 3.6 B. In contrast, dissipative coupling diminishes small peaks, smoothening the spectrum. This corresponds better to the experimental spectra, which exhibit a very smooth background spectrum, and potentially discrete, well separated peaks on top of that. We chose all oscillators in the model for the simulations of Fig. 3.6 to be critical. The effect of longitudinal coupling on active oscillators will be studied in the subsequent chapter of this thesis.

There exist several possible sources of longitudinal coupling by means of tissue connectivity in the cochlea. The three main candidates are given by the

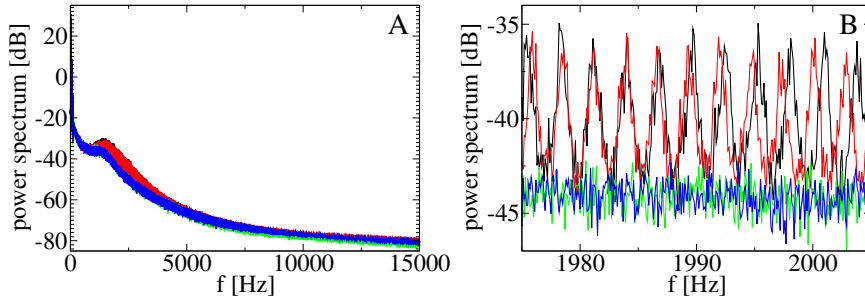


Figure 3.6: **Power spectra for different cases of the longitudinal coupling.** A: Black: No longitudinal coupling, red: Purely elastic coupling, green: Purely dissipative coupling, blue: Elastic and dissipative coupling. B: Zoomed in version of graph A. Parameters as in table 2.1.

tectorial membrane, the reticula lamina, and the BM. The tectorial membrane is situated on top of the tips of the hair bundles, thus connecting stereocilia of different hair cells, which are widely believed to be the source of the active amplification. The reticula lamina consists of hexagonal tilings placed on the top surfaces of the outer hair cells and the phalangeal processes of the Deiter's cells [84]. The BM is located below the hair cells, supporting the whole organ of Corti. In both a theoretical order of magnitude analysis by Jaffer and an experimental study by Naidu and Mountain, the reticula lamina was found to be the main source of longitudinal tissue connectivity [104, 60, 61]. However, it seems also plausible that longitudinal coupling mediated by the BM or the tectorial membrane contributes in a significant manner [105, 125].

### 3.5 Static disorder in the properties of oscillators and spontaneous emissions

Based on the ubiquitous presence of stochasticity in nature in general, introducing perturbed parameters of the cochlea comes to mind. In hearing research, mainly irregularities in the characteristic frequency  $\omega(x)$  are considered, in particular as a possible mechanism for the preferred minimal distance in SOAEs and the periodicity of SFOAEs [137] (see section 3.2). Note that we use the words disorder, perturbation, and irregularities synonymously.

In the following, the effect of irregularities in different parameters is examined: Static disorder is added to the characteristic frequency  $\omega(x)$ , the nonlinearity  $\beta(= \beta(x))$ , and the bifurcation parameter  $\epsilon(x)$ , and the effect of these perturbations are compared. More exactly, for a smooth parameter function  $\gamma(x)$ , the perturbed case is given by  $\gamma(x)(1+\nu(x))$ , where  $\nu$  is static, white Gaussian noise with zero mean and a small standard deviation. In particular, we investigate whether these perturbations serve as sources for SOAEs.

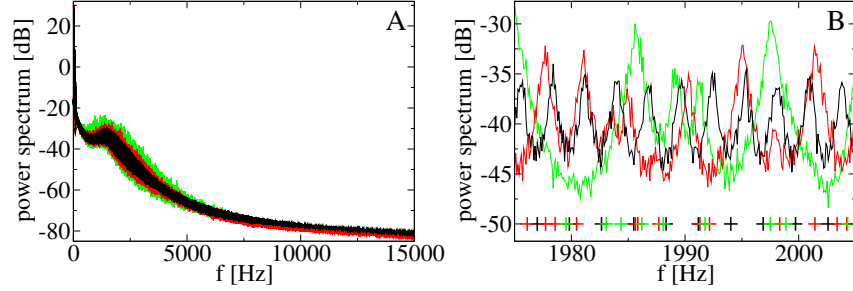


Figure 3.7: **Typical power spectra of  $p_e$  for disorder in the local best frequency  $\omega(x)$ .** A: Typical spectra of  $p_e$  for different standard deviations of the disorder in  $\beta$ :  $\delta\omega(x) = 0$  (black line),  $\delta\omega(x) = 1\text{‰}$  (red line),  $\delta\omega(x) = 1\%$  (green line). B: Zoomed in version of graph A with the same spectra. The x-values of the crosses indicate the eigenfrequency  $\omega(x)/(2\pi)$  of the oscillators. The y-value of the crosses was chosen arbitrarily.

In case of critical oscillators, i.e.  $\epsilon = 0$ , we find strong numerical evidence that disorder in  $\omega(x)$  or  $\beta$  does not elicit SOAEs. Only disorder in the bifurcation parameter  $\epsilon(x)$  is sufficient to generate SOAEs, which become manifest in peaks in the power spectrum of  $p_e$ . This finding also holds true in case of active oscillators, i.e. for  $\epsilon > 0$ , or in presence of longitudinal coupling, i.e. in these cases we also find strong numerical evidence that disorder in  $\beta$  or  $\omega(x)$  does not lead to SOAEs, in contrast to disorder in  $\epsilon$ . Note that for the spectra shown below, the system was simulated for 300 s with zero driving pressure, i.e.,  $p_{dr} = 0$ , employing the stochastic Hopf normal form with small additive white noise, taking the form of Eq. (3.1). Consequently, time traces of the ear canal pressure  $p_e(t)$  are obtained over 300 s via Eq. (3.5). From these time traces, the spectral density  $S(f)$  is computed by averaging the squares of the Fourier coefficients obtained for 1 s intervals.

### 3.5.1 Characteristic frequency

Perturbing  $\omega(x)$  with different strengths gives typical spectra as displayed in Fig. 3.7. The left side shows a larger part of the spectrum, the right side a more detailed view of the left side. As it is visible in Fig. 3.7 B, all model spectra consist of numerous small peaks in contrast to the smooth experimental spectra, which possess a very smooth background spectrum. The relative difference in characteristic frequency of neighboring oscillators is  $e^{\Delta x/d} - 1 = e^{10^{-5}/0.007} - 1 \approx 1.4\text{‰}$ . The magnitudes of the disorders in Fig. 3.7 are 1 ‰ (red line) and 1 % (green line). Thus, the disorder of the red line is comparable to the average

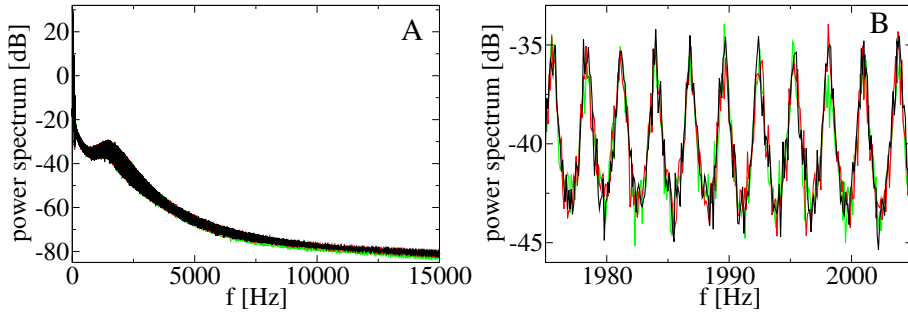


Figure 3.8: **Typical power spectra of  $p_e$  for disorder in the nonlinearity  $\beta$ .** A: Typical spectra of  $p_e$  for different standard deviations of the disorder in  $\beta$ : 5% (black line), 1% (red line), 1 ‰ (green line). B: Zoomed in version of graph A.

relative distance of neighboring oscillators, whereas the disorder of the green line is significantly higher. Hitherto, detailed experimental data on the heterogeneity of the physiological frequency gradient is lacking. The graph also demonstrates that disorder in  $\omega(x)$  leads to some oscillators having similar frequencies which in turn can lead to slightly higher peaks in the spectra. However, all spectra lack large peaks which rise substantially above the background spectrum. Note that we simulated numerous different realizations of disorders to verify if the presented results hold true in general and if the presented spectra are typical. We conclude that introducing disorder in the characteristic frequency is not sufficient to generate SOAEs.

### 3.5.2 Oscillator nonlinearity

Disorder in the nonlinearity  $\beta$  is another possible candidate for causing SOAEs. We perturb the constant  $\beta = \beta(x)$  as before spatially by adding frozen disorder in the form of white Gaussian noise. Graph 3.8 displays typical power spectra for different disorder strengths  $\delta\beta$ . It is visible that disorder in  $\beta$  is not sufficient to cause SOAEs. In fact, the spectra are basically indistinguishable from each other. It seems plausible that stochasticity in  $\beta$  does not suffice for SOAE generation because the nonlinearity only becomes a significant factor for oscillations above a certain magnitude.  $\beta$  does not influence small oscillations and mainly prevents the active Hopf oscillator from diverging.

### 3.5.3 Bifurcation parameter

In this subsection, we perturb the bifurcation parameter  $\epsilon(x) = 0$ . Introducing disorder in  $\epsilon(x)$ , realized as static white Gaussian noise, causes the system to exhibit SOAEs. This is plausible as the single oscillator exhibits oscillations if  $\epsilon$  is larger than zero. Fig. 3.9 displays typical power spectra for different strengths

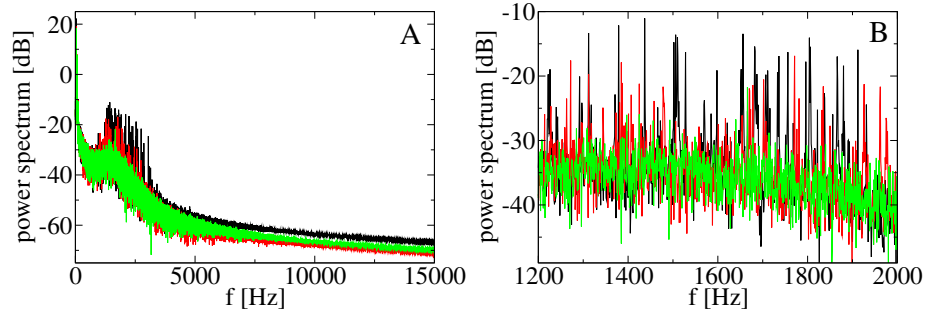


Figure 3.9: **Typical power spectra of  $p_e$  for disorder in the bifurcation parameter  $\epsilon(x)$ .** A: Typical spectra of  $p_e$  for different standard deviations of the disorder in  $\epsilon(x)$ : 5 Hz (black line), 2 Hz (red line), 1 Hz (green line). The mean value of  $\epsilon(x)$  is 0. B: Zoomed in version of graph A .

of disorder in  $\epsilon(x)$ . As expected, greater disorder in  $\epsilon(x)$  elicits stronger peaks in the spectrum. Peaks occur in a certain limited frequency range which is significantly smaller than the range of local characteristic frequencies being present on the BM. The local best frequencies present on the BM in the model,  $\omega(x)/(2\pi)$ , range from about 100 Hz up to 16000 Hz. Note that in contrast to experiments there is no preferred minimum distance visible between neighboring peaks in the spectrum. In conclusion, disorder in  $\epsilon$  elicits SOAEs, but in this setup it cannot account for the statistics of SOAEs. This suggests there might be an additional mechanism at work which prevents SOAEs from being too close to each other.

Switching on longitudinal coupling can lead to a separation of neighboring peaks and thus to the existence of a preferred minimal distance between neighboring emissions, as will be shown in the subsequent chapter (section 4.3).

## Chapter 4

# Statistics of spontaneous emissions in the model and in vivo

SOAEs possess rich statistics. In this chapter, we present experimental data and compare it with statistics obtained from the model employing longitudinal coupling and irregularities in the bifurcation parameter. The majority of the model parameters are fixed. We tune free model parameters to match the statistics observed in experiments. Furthermore, we discuss several extensions of the model, and we present pure tone responses of the new model, showing that it still functions as an 'ear' in the sense that it is able to detect sinusoidal stimuli.

Two examples of emission spectra of our model were already presented in Fig. 1.7 C and D. In the panels below the subgraphs C and D, the corresponding irregularities  $\epsilon$  are plotted as a function of the local best frequency  $\omega(x)/(2\pi)$ . Spectra typically contain emissions in frequency regions where oscillators are active (i.e.,  $\epsilon(x) > 0$ ), while the converse is not necessarily true, i.e., positive excursions of the bifurcation parameter  $\epsilon(x)$  do not necessarily lead to emissions in the spectra.

SOAEs typically occur in the frequency range of up to 8 kHz. The lower bound for accepting an emission as a SOAE is 500 Hz. The number of SOAEs per ear is an exponentially decaying distribution. Furthermore, SOAEs show the striking and puzzling feature of a characteristic minimal distance of about one semi-tone between neighboring emissions. This preferred minimum spacing decreases slightly for increasing frequency. It is presently unresolved what the underlying mechanism for these statistics is. In this chapter, we provide a model that accounts qualitatively and quantitatively for those statistics.

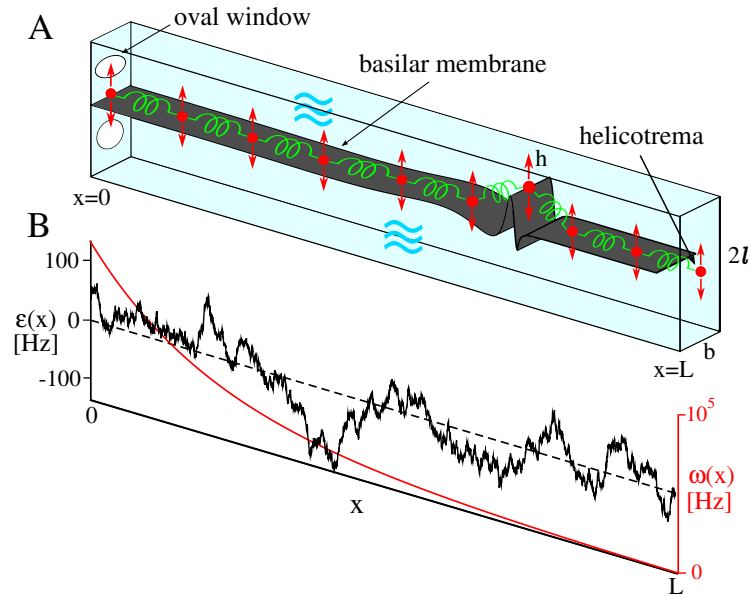


Figure 4.1: **Schematic representation of the full cochlear model in the time domain including elastic and dissipative coupling and irregularities in the bifurcation parameter.** A: The rectangular cochlea of length  $L$ , breadth  $b$ , and height  $2\ell$  is separated by the BM (dark gray) in two fluid-filled chambers. The oval window and the helicotrema are located at  $x = 0$  and  $x = L$ , respectively. Vertical displacements of the BM are denoted by  $h(x)$ . The BM is represented by a discrete chain of oscillators (red dots), which are coupled via hydrodynamic interactions (blue waves) and elastic and dissipative coupling (green springs). B: The frequency profile  $\omega(x)$  (red line) is shown together with a typical profile of the irregularities  $\epsilon(x)$  (black line) along the cochlea.

We compare the model results with experimental data which were kindly provided by Talmadge [146]. He investigated 76 humans or, equivalently, 152 ears. For each ear he recorded time traces of the pressure in the ear canal for 5 minutes. Ears of the same person are not independent regarding their SOAE properties. For instance, if a SOAE with frequency  $f_1$  is present in one ear, the other ear possesses a higher than average probability to exhibit a SOAE within a few hundred Hertz of  $f_1$ . However, when we calculate the histograms for the data from all 152 ears. We compare the model results with experimental statistics by simulating 152 individual realizations of the model using the final parameter values (see table 4.1) for 300 s, each provided with static irregularities in the bifurcation parameter  $\epsilon(x)$ . Repeating this procedure ten times gives the averages and standard deviations for these model distributions indicated by the gray shaded areas in the figures presented subsequently.

Table 4.1: List of free fit parameters

Parameter	Definition	Value
$D$	noise strength	$10^{-21} \text{ m}^2/\text{s}^2$
$\kappa$	dissipative coupling	39 Hz
$\kappa'$	elastic coupling	330 Hz
$n_c$	correlation length of $\epsilon(x)$	$5 \cdot 10^{-3} \text{ m}$
$\sigma$	standard deviation of $\epsilon(x)$	58.5 Hz

The time-independent, perturbed bifurcation parameter  $\epsilon(x)$  lends individuality to each simulation run. We model  $\epsilon(x)$  as a static Ornstein-Uhlenbeck process, thus attaining a bifurcation parameter which possesses a Gaussian distribution with standard deviation  $\sigma$  and zero mean, and which is exponentially correlated in longitudinal direction in space with correlation length  $n_c$ .

The dynamical noise is realized as additive white Gaussian noise and is not a key factor in our simulations. We use it mainly as a regularization instrument. The strength of the noise is chosen such that the background of the spectrum is in a reasonable physiological range. However, note that we do not aim for a description of the background. The noise mildly influences the frequency distribution of SOAEs and the distribution of distances between adjacent SOAEs.

We utilize the remaining free parameters of the model to fit the statistics of the experiment. In particular, we use the standard deviation  $\sigma$  and correlation length  $n_c$  of the bifurcation parameter, and the strengths of dissipative and elastic coupling  $\kappa, \kappa'$ .  $\sigma$  is chosen such that the total number of SOAEs of all 152 realizations of the model matches the total number of 588 experimental SOAEs summed over all ears. The range of occurring frequencies is dependent on multiple parameters including the free parameters and the value of  $\alpha$ , which we leave fixed. In the linear case of the model,  $\alpha \cdot \omega(x)$  is the stiffness per unit area of the BM. The numerical value of  $\alpha$  was derived from measurements of the static vertical deflection of human post-mortem BMs in response to global pressure [41, 14]. This determines only the static response, whereas the model is manufactured to describe the cochlear response to frequencies in the range of the local best frequencies of the BM. Although stiffness is not a very vulnerable physiological property, a more realistic value of  $\alpha$  would have to be inferred from experiments with living specimen and at non-zero frequencies. However, the chosen value of  $\alpha$  serves as an approximation and upper bound of a more realistic value.

The distribution of the number of emissions per realization depends mainly on  $n_c$ , but it is also influenced by the threshold criterion. The longer the correlation, the more likely are realizations with a high number of SOAEs, provided we adjust the standard deviation  $\sigma$  such that the total number of 588 and thus the average number of 3.9 SOAEs per cochlea remains constant. In the limit of small  $n_c$  we find a rather narrow distribution of the number of emissions centering around the mean of 3.9 SOAEs per realization. Note that an increase

of  $n_c$  while keeping all other parameters constant leads to a decrease in the total number of emissions, as we will discuss later. The preferred relative inter-emission interval length of neighboring SOAEs is predominantly determined by the coupling, more exactly by the relation between elastic and dissipative coupling. For our model, the elastic coupling dominates the dissipative. However, including dissipative coupling is necessary to obtain a characteristic minimum distance between neighboring emissions. As it was found in experiments, the inverse relative inter-emission interval slightly increases for higher frequencies of SOAEs.

A sketch of the model is presented in Fig. 4.1. The model equations we consider in this chapter are given by the usual hydrodynamic equation (2.6), together with the middle ear equations developed in the last chapter and the following equation for the local oscillator dynamics presented in the continuum notation:

$$\partial_t z = (\epsilon(x) + i\omega(x))z - \frac{\beta}{\alpha}|z|^2 z + (\hat{\kappa} + i\hat{\kappa}')\partial_x^2 z + \xi(x, t) - \frac{i}{\alpha}p. \quad (4.1)$$

We consider disorder in the bifurcation parameter, which elicits SOAEs as we saw in the previous chapter. However, in this chapter the disorder possesses a different form. The disorder, which lends individual time-independent characteristics to a model cochlea, is generated by an Ornstein-Uhlenbeck-process via the stochastic differential equation

$$n_c \frac{d}{dx} \epsilon(x) = -\epsilon(x) + \nu(x), \quad (4.2)$$

where  $\nu(x)$  is a Gaussian stochastic variable with zero mean and correlations  $\langle \nu(x)\nu(x') \rangle = 2\sigma^2 n_c \delta(x - x')$ .  $\sigma$  and  $n_c$  are the standard deviation and the correlation length of  $\epsilon(x)$ , respectively. We employ the boundary conditions presented in the previous chapter given by Eq. (2.11) and Eq. (3.3) in combination with Eq. (3.6).

The continuum description of Eq. (4.1), Eq. (4.2), and Eq. (2.6) was introduced for the ease of notation. In the simulations of the model we solve a discrete version of these equations for the variables  $h_j, u_j, p_j, \epsilon_j$  at  $N$  discrete sites with positions  $x_j = \Delta x \cdot j$ ,  $j = 0, \dots, N$ , and  $\Delta x = L/N = 10^{-5}$  m, as outlined in section 2.2. We choose  $N = 3500$  corresponding to the approximate number of rows of hair cells in the human cochlea [32]. The spatially discretized form of Eq. (4.1) reads

$$\frac{dz_j}{dt} = (\epsilon_j + i\omega(x_j))z_j - \frac{\beta}{\alpha}|z_j|^2 z_j + (\kappa + i\kappa')(z_{j+1} - 2z_j + z_{j-1}) + \xi(x_j, t) - \frac{i}{\alpha}p_j. \quad (4.3)$$

Eq. (4.2) is simulated once for each simulation and is kept constant throughout the time evolution of the specific realization of the model. Starting at  $x = 0$  with a value drawn from the stationary distribution, the Ornstein-Uhlenbeck process is simulated forward in longitudinal direction by employing the Euler

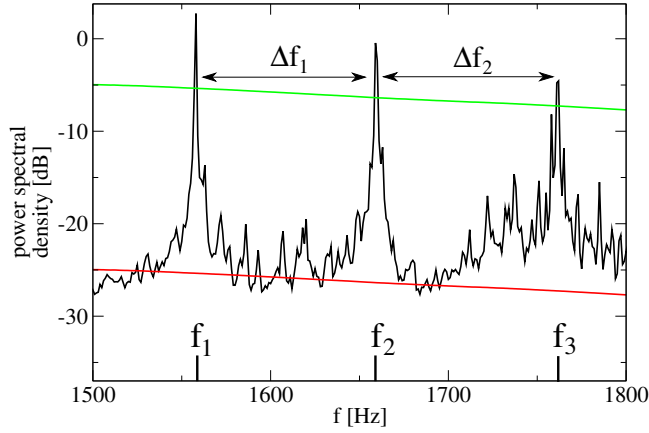


Figure 4.2: **Detection criterion of spontaneous emissions.**: An example of a power spectrum  $S$  (black line) of the ear canal pressure  $p_e$  obtained in the model in a small frequency interval exhibiting three emissions at frequencies  $f_1$  to  $f_3$ . Intervals between neighboring emissions are denoted by  $\Delta f_1$  and  $\Delta f_2$ . The running average of  $\log(S)$  (red curve) is determined with a window size of 1000 Hz. If an emission in the power spectrum exceeds the running average by 20 dB (indicated by the green curve), an emission is detected.

scheme with a step size of  $10^{-8}$  m until  $x = L$  is reached. The discrete values of  $\epsilon_i$ , where  $i = 0, \dots, N$ , are obtained by sampling each 1000th point.

The parameters values used in this chapter for fitting the experimentally observed statistics are denoted in table 4.1. For the other parameters see tables 2.1 and 3.1.

## Emission detection

From the simulations, time traces of the ear canal pressure  $p_e(t)$  are obtained via Eq. (3.5) for a simulation time  $T = 300$  s corresponding to the measurement time in the experiments by Talmadge. From these time traces, the spectral density  $S(f)$  is computed by averaging the squares of the Fourier coefficients obtained from 1 s intervals. The starting conditions are given by  $h_i = u_i = p_i = 0$  for all  $i = 0, \dots, N$ . Note that the system reaches a cyclo-stationary steady state in less than 1 s. Furthermore, the starting conditions do not affect simulation results significantly.

In the field of mechanics of hearing, there is no consensus on the optimal detection criterion, as experiments face substantial challenges and diverse noise sources such as line noise [146]. Consequently, in experiments different SOAE detection criteria were put forward over the course of time. A frequent crite-

tion is the requirement that the peak in the power spectrum is 3 dB above the background spectrum [131].

Here we use a self-referencing threshold criterion, as illustrated in Fig. 4.2: For each spectrum (black line) we define spontaneous otoacoustic emissions as peaks in the spectrum  $S(f)$  which rise above the background level by more than a threshold level which we choose at 20 dB, indicated by the green line. The background is defined as the running average of the decibel values of the spectrum over a 1000 Hz interval, indicated by red line.

We compare the statistics of the so defined SOAEs with those obtained from experiments by Talmadge [146]. For the peak detection in experimental spectra, Talmadge used slightly different criteria which were needed because of considerable amounts of noise, which affected the background and introduced additional AC peaks. Since such artifacts are absent in our simulations, we can detect peaks by the simpler criterion stated above. The criterion used by Talmadge is that a peak has 5 points above the visual top of the noise floor. This condition is chosen to ensure that the false alarm rate is small. Put differently, the method shall reduce the number of emission which are accepted as SOAEs but are in fact none. One difficulty in experiments is the so called 'line noise', which is due to electrical currents that show higher harmonics, even in the range of the 100th higher harmonic.

The uniqueness and the constance over time of emission spectra is caused in our model by the static irregularities of the bifurcation parameter  $\epsilon_n$  in a given realization. From the procedure specified above, we obtain for a given realization of  $\epsilon_n$  a discrete sequence of peak frequencies  $f_m$ , with  $m = 1, \dots, M$ , where  $M$  is the number of emissions in the spectrum. In order to compare the statistics of SOAEs in our simulations with human cochleae, we use 152 different realizations of  $\epsilon_n$  corresponding to the number of individual cochleae studied in the experiments by Talmadge et al. [146].

## 4.1 Emission frequencies

The range of experimental SOAEs spans the entire frequency range from 0.5 to 8 kHz. Peaks in the power spectrum with frequencies below 500 Hz are discarded due to the presence of physiological noise sources (such as respiratory, muscular or cardiovascular activity) that might cause these peaks. The blue count histogram in Fig. 4.3 displays the experimental distribution of the SOAE frequencies exhibiting a bimodal distribution with two (local) maxima at 1.5 kHz and 3 kHz. The histogram is binned logarithmically, each bin corresponding to two semitones. Note that the bimodality is also present in the experimental data set measured by others [20, 131]. The 3 kHz mode has been attributed to a resonance in the external ear canal, whereas for the 1.5 kHz mode it has been claimed that there is no mechanical explanation [20]. In particular, there is experimental data that suggests that the eigenfrequency of the middle ear is not 1.5 kHz and thus cannot be the source of this mode. However, the middle ear model employed by Talmadge possesses an eigenfrequency of 1.5 kHz [148]

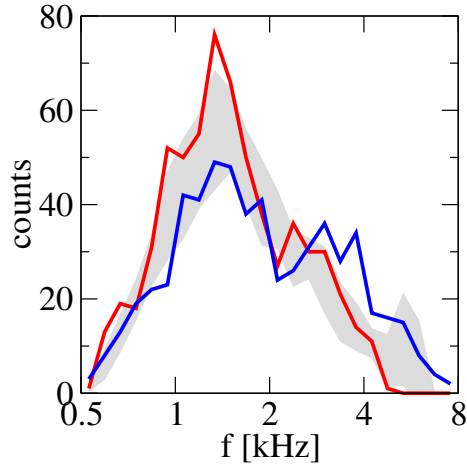


Figure 4.3: **Histogram of the frequencies of SOAEs.** Count histograms of emission frequencies detected in the experiments on 152 individual cochleae in the experiments (blue) and the model (red). The gray region depicts the standard deviation around the average calculated from 10 sets of 152 model realizations.

and stems from a more complicated, biophysical model. Thus, there is some apparent conflict between Braun’s statement above and the model employed by Talmadge et al.

The red line in Fig. 4.3 depicts the count histogram of SOAE count histogram of SOAE frequency obtained in our model from 152 realizations of the irregularities.

The simulated frequency statistics of emissions accounts for both the range of otoacoustic emissions (0.5 - 8 kHz) and the peak in the experimental histogram near 1.5 kHz. In some of our simulation results we obtain a bimodal distribution as well. The pronounced maximum at 1.5 kHz corresponds to the eigenfrequency of the harmonic oscillator representing the middle ear. In the model we assume a uniform pressure in the entire ear canal, describing it by one variable  $p_e$ , thus excluding the phenomenon of a possible resonance in the ear canal.

## 4.2 Emission numbers

In the experimental data from Talmadge [146], the total number of emissions  $M$  for a given cochlea varies broadly. A histogram of the emission number is shown in Fig. 4.4, indicated by the blue circles. 67 of the 152 cochleae studied did not possess any SOAEs. Emission numbers above 20 occurred occasionally and reached up to 32 SOAEs per cochlea [146].

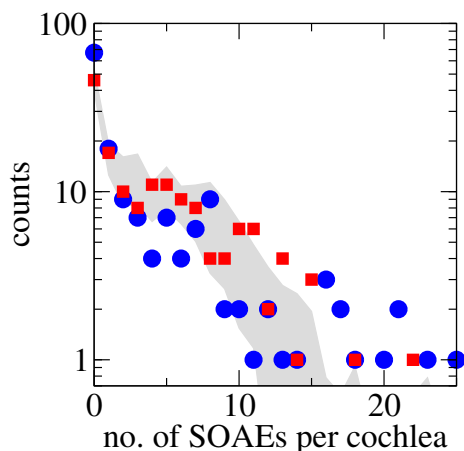


Figure 4.4: **Histogram of the number of SOAEs per cochlea.** Histogram of the SOAE number per cochlea detected in 152 individual cochleae in the experiments (blue circles) and the model (red squares). The gray region indicates the standard deviation around the average determined from 10 repetitions of 152 realizations of the model.

The experimental histogram of the number of emissions  $M$  is well captured by our model. A typical histogram of  $M$  obtained from the model with parameters as in table 4.1 is displayed by the red squares in Fig. 4.4. Using ten sets of 152 realizations each, we see a shoulder in the histogram, indicated by the gray band, which seems consistent with the experimentally obtained data. However, there are slightly more cochleae with more than 20 emissions in the experimental data compared to the simulations. A possible reason for this discrepancy might be that the experimental, physiological equivalent to the bifurcation parameter in the model does not possess Gaussian statistics. However, we will see later that a slightly negative mean value of the bifurcation parameter leads to more similar distributions of the number of emissions. Both the experimental and the model distribution follow roughly an exponential decay with the exception of the data point indicating the number of zero emissions.

The number of emissions is related to the number and size of active regions in the cochlea, which is governed by the parameters  $n_c$  and  $\sigma$  characterizing the irregularities.  $\sigma$  is adjusted such that for given  $n_c$ , the total number of SOAEs summed over all 152 cochleae corresponds to the number of 588 SOAEs detected in experiments. For small  $n_c$  the number of SOAEs per realization does not follow an exponential shape but resembles a Gaussian distribution. For fixed  $\sigma$ , an increase in  $n_c$  leads to a decrease of the total number of SOAEs.

These observations can be explained in the framework of the peak separation and the resulting preferred distance between neighboring emissions. A long active region of the cochlea, corresponding to a long positive and uninterrupted

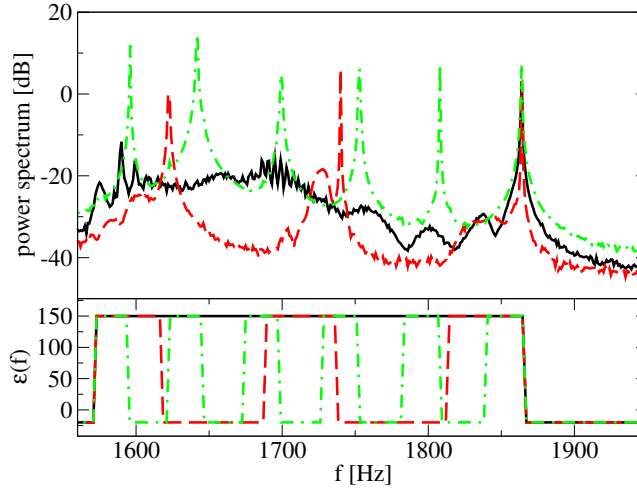


Figure 4.5: **Power spectra exhibit more peaks for more small intervals with  $\epsilon > 0$  than few long intervals with  $\epsilon > 0$ , if longitudinal coupling is present.** Lower panel: Bifurcation parameters  $\epsilon(f)$  for three different lengths of active intervals, i.e.,  $\epsilon > 0$ , plotted as a function of  $f$ , using the correspondence between  $f$  and  $x$  via  $\omega(x)$ . Upper panel: Three power spectra obtained from simulations of the model with the three corresponding bifurcation parameters from the lower panel, where the black spectrum belongs to the black bifurcation parameter realization, and similarly for red and green.

excursion of bifurcation parameter  $\epsilon$ , causes fewer emissions than a number of short sections which together span the same length. The latter case corresponds to a bifurcation parameter  $\epsilon$  which is positive for short, consecutive intervals that are separated by intervals with  $\epsilon < 0$ . Fig. 4.5 shows a long interval with positive  $\epsilon$  (black line in the lower panel) and the resulting power spectrum (black line in the upper panel). Also plotted are two realizations with short intervals of positive  $\epsilon$ , separated by small regions of  $\epsilon < 0$  (red and green lines in the lower panel), together with the obtained power spectra (red and green lines in the upper panel). It is apparent that the power spectrum indicated by the green broken line exhibits more SOAEs than the spectrum indicated by the red line, and likewise the spectrum marked in red exhibits more emissions than the power spectrum marked in black. The correlation length  $n_c$  governs the probability of long excursions. An increase of  $n_c$  makes long excursions more likely and thus leads to a smaller total number of emissions if all other parameters remain constant.

Now we want to explain the observation that an increase  $n_c$  makes large numbers of emissions per cochlea more likely, provided we increase  $\sigma$  such that the total number of emissions remains constant.

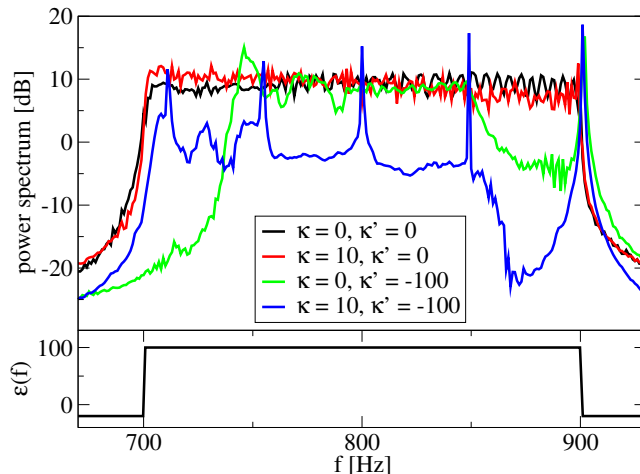


Figure 4.6: **Power spectra for different strengths of longitudinal coupling.** For all spectra in the upper panel the bifurcation parameter  $\epsilon(f)$  is as depicted in the lower graph by the black line: For oscillators with eigenfrequencies ranging from 700 to 900 Hz, we have  $\epsilon = 100$  Hz, all others possess values of  $\epsilon = -20$  Hz. The strengths of the longitudinal coupling for the power spectra are given by 0 Hz (black line), 10 Hz (red),  $-i \cdot 100$  Hz (green),  $10 - i \cdot 100$  Hz (blue), where the terms with and without the factor  $-i$  denote the strength of dissipative and elastic coupling, respectively.

Leaving  $\sigma$  fixed and increasing  $n_c$  leads to an increase in the variance of the average number  $\bar{\epsilon}$  of each realization of  $\epsilon$ , i.e.,  $\bar{\epsilon} = \sum_{j=0}^{j=N} \epsilon_j / (N + 1)$ , for an individual realization of the irregularities. Note that the theoretical mean value of  $\epsilon$  is by definition  $\bar{\epsilon} = 0$ , which would correspond to an infinite sampling. A larger  $n_c$  leads to an effectively smaller number of samplings: The sample size of 3501 remains constant, but for higher  $n_c$  the individual values are more similar due to the higher correlation length. The two extremes are  $n_c = 0$ , where we sample 3501 independent values of  $\epsilon$ , and  $n_c \rightarrow \infty$ , where we sample 3501 identical values.

If we increase  $n_c$  and then also increase  $\sigma$  such that the total number of emissions remains constant, we obtain a higher variance of  $\bar{\epsilon}$  and also a higher variance of  $\epsilon_n$ . This increases the probability of realizations with a high value of  $\bar{\epsilon}$ . Such irregularities lead in turn to large numbers of emissions per realization.

### 4.3 Relative frequency intervals between emissions

Inner ears of different species exhibit the puzzling feature of a regular relative inter-emission intervals with a preferred relative distance. For humans the dis-

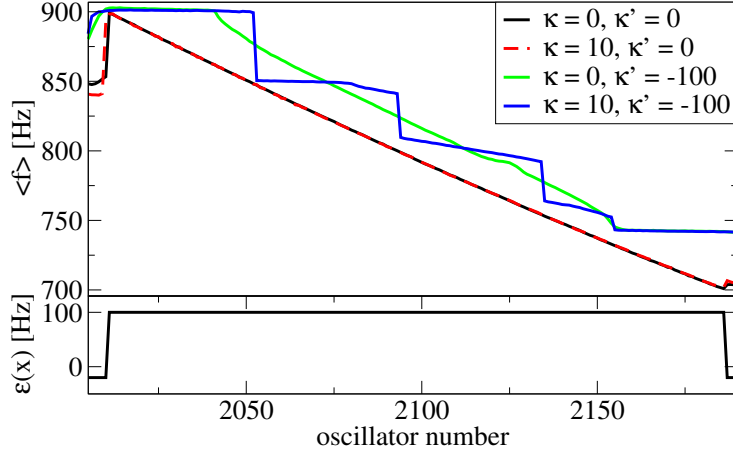


Figure 4.7: **Average frequencies for different strengths of longitudinal coupling.** Average oscillation frequencies  $f = 1/\langle T \rangle$  determined from the average oscillation period  $T$  in the simulation as a function of oscillator number  $j$  for bifurcation parameter depicted in the lower panel, given different coupling strengths of 0 Hz (black line), 10 Hz (red),  $-i \cdot 100$  Hz (green),  $10 - i \cdot 100$  Hz (blue), where real and imaginary numbers denote the strength of dissipative and elastic coupling, respectively. The data is obtained from the same simulation as in Fig. 4.6.

tribution of the relative distance shows a maximum at one semitone, which is equivalent to a value  $\bar{f}/\Delta f = \sqrt{f_1 \cdot f_2}/|f_2 - f_1| \approx 17$  for two neighboring frequencies  $f_1, f_2$ , and exhibits a trend towards higher values of  $\bar{f}/\Delta f$  for increasing frequencies. It was shown that longitudinal coupling of active oscillators can lead to synchronized clusters of oscillators, resulting in a set of discrete peaks in the spectrum with a preferred minimal distance [152]. By introducing elastic and dissipative longitudinal coupling, we can capture both the preferred minimum distance of 100 Cent, equivalent to one semitone, as well as the trend. First, we describe the mechanism involving longitudinal coupling, then we present statistics of the experiments and the model.

### Emission mechanism

In the upper panel of Fig. 4.6 we see power spectra for cochleae with an activated stripe in the region from 700-900 Hz (i.e., oscillators with eigenfrequencies in this interval possess  $\epsilon > 0$ ) for four different cases of longitudinal coupling, where the bifurcation parameter values are given by the lower panel and are the same for all four spectra. The power spectrum for the system without longitudinal coupling (black line) exhibits a plateau and no discrete peaks. The same holds true for the case of purely dissipative or purely elastic coupling (red and green, respectively). In contrast, if both elastic and dissipative coupling are present

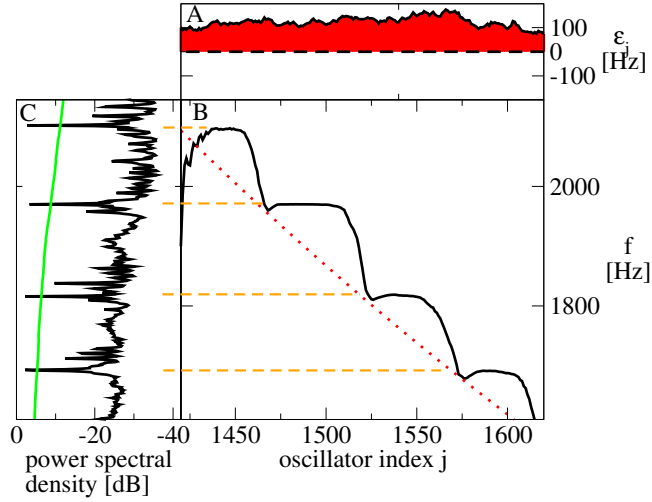


Figure 4.8: **Oscillation frequencies within an active region in the cochlea model.** A: Irregularities  $\epsilon$  as a function of oscillator index  $j$  within a small frequency interval. The red area indicates  $\epsilon > 0$  corresponding to active oscillators. B: Actual frequency oscillation  $f = 1/\langle T \rangle$  calculated from the average oscillation period  $T$  in the simulation (black) together with characteristic frequency (red dotted line). C: Power spectrum of the ear canal pressure in the model. The threshold line (green) is employed to identify emissions. Spontaneous emissions, visible as peaks in the spectrum in C, correspond to frequency plateaus in B (dashed orange line).

(blue), where the elastic coupling dominates, the spectrum exhibits sharp, well-separated peaks. Note that, in general, dissipative coupling alone can also lead to peak separation [152]. Fig. 4.7 displays the corresponding actual average frequencies of oscillation. In this parameter regime, plateaus emerge only if both dissipative and elastic coupling are switched on. These sharp plateaus lead to separated peaks in the power spectrum, and the frequency of the plateaus correspond to the frequencies of the peaks in the spectrum. The length of these plateaus determine the frequency differences between the resulting plateaus and thus the frequency differences of emissions in the power spectra. Due to the presence of the elastic coupling, the frequency of each plateau is determined by the oscillator with the highest eigenfrequency within the group of synchronized oscillators [152].

Each realization of  $\epsilon_j$  defines regions in which  $\epsilon > 0$  and the model cochlea is active, see Fig. 4.8 A. The length of these regions is of the order of  $n_c$ , the correlation length of the irregularities. The typical maximum of such excursions in  $\epsilon$  is substantially smaller than the eigenfrequency  $\omega(x_j)$ . In an active region, oscillators, which possess a gradually varying intrinsic local best frequency  $\omega(x_j)$ , tend to oscillate spontaneously. Due to the presence of elastic and dissipative

coupling, oscillators form synchronized clusters, i.e. groups emerge in which they oscillate with the same frequency. Fig. 4.8 B shows the local average frequency as a function of oscillator index  $j$ , indicated by the black solid line. In this plot, synchronized clusters correspond to frequency plateaus in the black line. The average frequency is defined as the average number of oscillation periods per unit time determined for oscillator  $j$  in the model. The power spectrum of the ear canal pressure  $p_e$  in Fig. 4.8 C reveals the correspondence between the frequencies of peaks in the spectrum and the oscillation frequencies of the plateaus, indicated by the dashed orange lines. Thus, the number of oscillators  $N_{syn}$  which cooperate in a synchronized cluster determines the distance between two emissions. In the example of Fig. 4.8  $N_{syn} \approx 40$  corresponding to  $\bar{f}/\Delta f \approx 17$ . For the parameter values used here  $N_{syn} < N_c$ , the number of correlated oscillators, given by  $N_c = n_c \Delta x$ . Consequently, active regions typically split up into several synchronized clusters, causing multiple neighboring discrete peaks in the power spectrum. Due to the presence of elastic coupling, the frequency of each plateau corresponds to the oscillator in the cluster with the highest characteristic frequency [152]. Unfortunately, there is still a lack of theoretical understanding of clustering in presence of both elastic and dissipative coupling. Osipov and Sushchik investigated the case of a chain of purely dissipatively coupled active oscillators with a linear frequency gradient and derived an approximate formula for the cluster size [113], which we will employ in the following subsection. However, they did not consider a cochlea model. In particular, no hydrodynamic interactions are present in their study.

### Inter-emission interval statistics

Given the peak separation mechanism, which was described in the previous section, we now turn towards the statistics of the inter-emission intervals. The statistics of intervals  $\Delta f = f_n - f_{n-1}$  between adjacent emissions are of special interest. We consider the inverse relative interval  $\bar{f}/\Delta f$ , where  $\bar{f} = (f_{n-1}f_n)^{1/2}$  and alternatively the interval measured in Cent units defined as  $I(f_n, f_{n-1}) = 1200 \cdot \log_2(f_n/f_{n-1})$ . Note that, by definition, 100 Cent are equal to one semitone. Both interval measures have been employed previously to characterize spontaneous emissions [131, 19, 137]. Fig. 4.9 A displays the reverse relative intervals as a function of the mean frequency  $\bar{f}$  (blue circles), which scatter around  $\bar{f}/\Delta f \approx 17$ . There is a trend towards larger values of the inverse relative interval  $\bar{f}/\Delta f$  for increasing frequencies. Many intervals lie around a straight line corresponding to a power law [137]

$$\Delta f \sim \bar{f}^\nu. \quad (4.4)$$

A value of  $\nu = 0.31 \pm 0.05$  was estimated by Shera [137] for the data shown in Fig. 4.9 A as blue circles. The distribution of the relative intervals in Cent units is shown in Fig. 4.9 B. In the experimental data (blue histogram), the most frequent relative interval occurs at 100 Cent corresponding to one semitone interval [19].

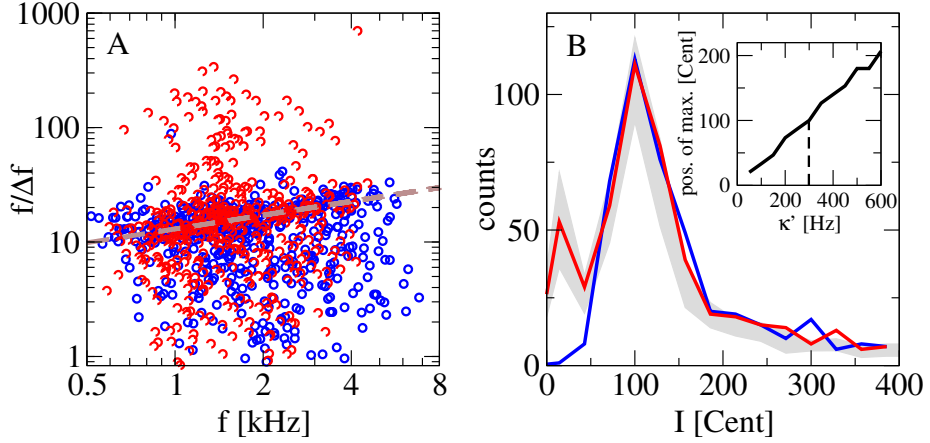


Figure 4.9: **Comparison of the statistics of emission frequency intervals in model (red) and experiment (blue).** A: Inverse relative frequency intervals  $\frac{\bar{f}}{\Delta f} = \frac{\sqrt{f_1 f_2}}{|f_2 - f_1|}$ , where  $f_1$  and  $f_2$  are frequencies of two adjacent emissions in the spectrum. Data points correspond to pairs of emissions in 152 realizations (model) or ears (experiment). The dashed brown line indicates the relation  $\Delta f \sim f^{0.39}$ . B: Histogram of the relative frequency intervals, defined by  $1200 \log_2 \frac{f_2}{f_1}$ , given in units of Cent (1200 Cent correspond to one octave) for the same data as in A. The gray region indicates the standard deviation around the average determined from 10 repetitions of 152 realizations of the model. The inset shows the relative frequency interval corresponding to the maximum in the histogram as a function of the elastic coupling strength of oscillators. The dashed line denotes the parameter value of the elastic coupling used for simulations.

The scatterplot of inverse relative emission intervals obtained from the model, plotted versus frequency (see Fig. 4.9 A), corresponds well to the experimental data. However, in simulations there are more small intervals  $\Delta f$  with  $\bar{f}/\Delta f > 100$ , which lead to second peak at small Cent values in Fig. 4.9 B. This difference in distributions might be partly due to the different peak detection criteria employed in experiments and simulations. Observe that the model can capture both the maximum at about 100 Cent and the overall shape of the interval histogram shown in Fig. 4.9 B for large Cent values. Finally, our model also accounts for the trend of the intervals towards higher values for increasing frequency  $\bar{f}$ , described by Eq. (4.4). Fitting this relation to the maxima of the distribution of the inverse relative intervals, we estimate  $\nu \approx 0.39 \pm 0.04$  for the model data and  $\nu \approx 0.33 \pm 0.1$  for the experimental data. Thus, the model value is consistent with the experimental data within the error margin. Note that the error margin in our estimate of the value of  $\nu$  obtained from the experimental data is higher than the value reported by Shera, which is due to the employment of different estimation schemes.

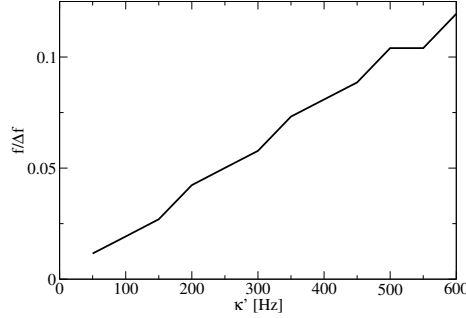


Figure 4.10: Preferred minimum distance  $\Delta f/\bar{f}$  as a function of elastic coupling strength  $\kappa'$ .

The number of oscillators  $N_{syn}$  which cooperate in a synchronized cluster determines the distance between two emissions. For the parameter values used here, it holds  $N_{syn} \approx 40$  corresponding to  $\bar{f}/\Delta f \approx 17$ . As  $N_{syn} < N_c = 500$ , where  $N_c$  is the correlation length of the Ornstein-Uhlenbeck process measured in numbers of oscillators, active regions typically break up into several synchronized clusters, see Fig. 4.8.

In order to discuss the typical intervals between emissions, we need to understand the size  $N_{syn}$  of synchronized clusters [41, 113]. Hitherto, there exists no general theory for the cluster size  $N_{syn}$ . For purely dissipative coupling and a linear frequency gradient, a necessary condition for global synchronization was calculated [113],

$$\left| \frac{(\omega(x_n) - \omega(x_{n-1}))N_{syn}^2}{8\hat{\kappa}} \right| < 1, \quad (4.5)$$

where  $\hat{\kappa}$  denotes a coupling strength. We make the assumption that relation (4.5) can be used to estimate the maximal size of clusters in case of a chain that breaks up into several clusters. In addition, we assume that the relation holds even in the presence of elastic coupling and for nonlinear frequency gradients. Thus, we obtain a relation for the inter-emission interval,  $\Delta f = \Delta\omega/(2\pi)$ , with  $\Delta\omega \approx N_{syn}(\omega(x_{n-1}) - \omega(x_n))$ . Employing  $\omega(x_{n-1}) - \omega(x_n) \approx \partial_x\omega(x_n)\Delta x = \omega(x_n)\Delta x/d$ , relation (4.5) leads to

$$\frac{(\Delta\omega)^2 d}{8\hat{\kappa}\omega(x)\Delta x} < 1. \quad (4.6)$$

In order to estimate the maximal values for which this relation still holds, which gives us the maximal cluster size, we assume equality in this relation. Thus, we arrive at  $\Delta\omega \sim \omega^{1/2}$  corresponding to  $\nu = 1/2$ . This value is not consistent with experimental data, but it is also not drastically different from it.

The inset in Fig. 4.9 shows the position of the maximum of the Cent histogram as a function of elastic longitudinal coupling strength  $\kappa'$ . Stronger coupling

leads to an increase in cluster size and consequently to larger frequency differences between neighboring clusters, causing larger relative frequency differences between neighboring SOAEs. The relation between the elastic coupling strength  $\kappa'$  and the mean relative frequency difference  $\Delta f/\bar{f}$  is roughly linear, shown in Fig. 4.10, in contrast to the prediction of formula (4.5). However, note that consistency with the formula could not be expected as the formula holds only in case of purely dissipative coupling.

## Discussion

The level of the background of the power spectra is significantly lower than seen in experiments. However, we do not aim for a description of the background, which might depend on the measurement apparatus and technique, which might be influenced by microphone noise and other noise sources. Utilizing stronger additive noise leads to a diminishing of the cooperative effect if all other parameters are kept constant. This results in less clustering and consequently more small relative SOAE distances and fewer inter-emission intervals of one semitone or larger.

The quality of an emission in a power spectrum is defined as the ratio of the frequency and the full half-width, see Fig. 1.11. For a single Hopf oscillator the quality is determined by noise, the bifurcation parameter and the nonlinearity, see subsection 1.3.2. An increase in additive noise leads to smaller and broader peaks in the power spectrum. This holds also for our model consisting of an array of coupled Hopf oscillators. For the model with parameters used for matching the statistics, see table 4.1, quality factors of SOAEs center around 100000, which is three orders of magnitude higher than what is observed in experiment, where quality factors range from about 10 to 10000 with a maximum around 100, see Fig. 4.11. Note that some quality factors of the model might be even higher. This is due to the fact that simulation time was limited to 300 s. The accuracy of the estimate of the quality factors is dependent on the simulation time. In order to precisely measure high quality factors corresponding to small widths, long simulation times of the model are required. The discrepancy between quality factors from model and experiments is presumably partly due to the different peak detection criterion: For the model, only those peaks are identified as SOAEs which rise 20 dB above the background spectrum, thereby discarding low and broad peaks and detecting emissions regardless of their width. In contrast, Talmadge identified peaks as SOAEs if the peak rises above the visual noise floor for at least 5 points of the spectrum (with a resolution of about 1 Hz). This implies that small but broad peaks may also be counted (the data set indeed contains peaks which rise less than 3 dB above the noise floor), whereas large and sharp peaks might be discarded. However, these differences do not fully account for the observed discrepancy. Thus, the model indicates that the influence of noise on the system might be substantially more complex than processes which can be captured by dynamical, additive white Gaussian noise. There might be other processes taking place in the cochlea which determine the quality and are not captured or well described by the noise we employed. Other

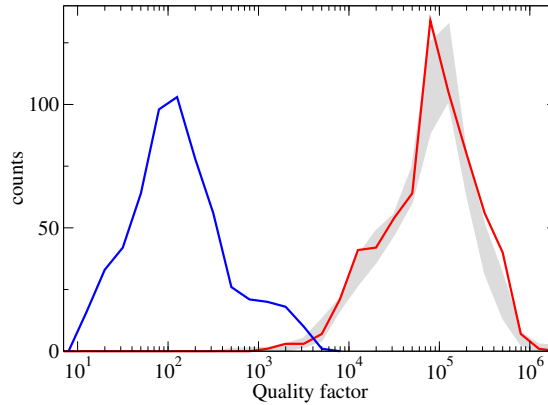


Figure 4.11: **Distributions of the quality factor of SOAEs in experiment and simulation.** The graph shows the count histograms of the quality factor of SOAEs in the experiment (blue) and the model (red) with the standard parameters of chapter 4. Data are shown for 152 individual ears in experiment and results from the model obtained from 152 realizations of the irregularities. The gray region indicates the standard deviation around the average determined from 10 repetitions of 152 model realizations.

noise sources such as physiological noise, caused for instance by cardiovascular activity, which is known to influence SOAEs [83], might be more appropriately described by a noise which acts on the phase of the oscillator, thus perturbing its characteristic frequency. Employing such noise leads indeed to a correct mean value of the quality, as shown in section 4.5.

The power of emissions in the model is comparable to the power seen in experiments, see Fig. 4.12. Both distributions have a similar mean power. However, the distributions exhibit different skews, and the experimental power distribution is wider than the distribution obtained from the model. In particular, some SOAEs from experiments reach higher maximal power than SOAEs in the model. This might be partly due to the different widths of the SOAEs, i.e., the fact that peaks in the model are substantially more narrow than in experiment. By increasing the noise in the model, two peaks which are very close to each other might merge and form one peak, whose power is the sum of the two individual peaks. In both model and experiment these results are influenced by diverse sources of uncertainties. Some degree of uncertainty results from the procedures with which the power is determined. Talmadge obtained the power of experimental SOAEs by performing a nonlinear fit consisting of a Lorentzian function plus background terms [146]. The fit parameters associated to the Lorentzian were then used to determine the power. The power distribution obtained from the model is calculated by integrating the numerical power spectrum in a small window and subtracting the background spectrum. In case of the model, this method is more reliable for determining the power of peaks because the method employed by Talmadge is strongly influenced by the

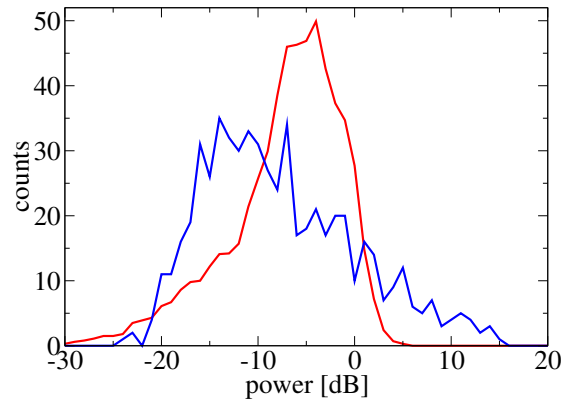


Figure 4.12: **Distributions of power of SOAEs in experiment and simulation.** The graph shows the count histograms of the power of SOAEs in the experiment (blue) and the model (red) with the standard parameters of chapter 4. Data shown for 152 individual ears in experiment and results from the model obtained from the average determined from 10 repetitions of 152 model realizations of the irregularities.

fit results of the widths. Due to the small values of the widths in the model, their fits are not very precise.

The power of SOAEs is influenced by both the power within the cochlea and the transmission properties of the middle ear. There exist diverse possible sources of the discrepancies between the power of SOAEs in the model and experiments. One source is given by the different transmission properties of the physiological middle ear and the harmonic oscillator representing the middle ear in the model. Put differently, transmission properties of the middle ear are more complex than transmission properties of the harmonic oscillator.

In cats it was observed that the prediction of the mechanical gain is higher than what is observed for the middle ear transmission in experiments [5]. It is difficult to perform this comparison in humans, but due to the anatomical similarity of mammalian cochleae, the discrepancy is believed to hold true for humans as well. The gain in humans (and other mammals including cats) varies among individuals and is strongly frequency dependent, and transmission gains in forward and backward direction are not related by an easy relation. These properties are due to several factors: The ossicles were found to behave differently with respect to forwards and reverse transmission. The lever joint of the ossicles is not completely fixed as it is held by ligaments and muscles. Besides, the ossicles display more complex motions than a lever does, particularly for higher frequencies [138]. The lever factor of the ossicles is not constant with respect to frequency as the ossicles do not move in total synchrony. Furthermore, the tympanum exhibits complex modes depending on the frequency [46, 38]. Moreover, the middle ear cavity is connected to mastoid air cells, which are air-filled cavities of varying sizes inside the temporal bone. These air cells influence

transmission properties as well and are considered to be important for the functioning of the middle ear [51, 98, 120]. Finally, the position of the microphone in the ear canal plays a role for the measurements of SOAEs, and the volume of the ear canal influences the strength of SOAEs.

In the following, we discuss parameter choices and estimates. The free parameters were fitted because there is no experimental evidence determining these parameters. However, for some we can provide estimates of upper bounds. The dynamical white Gaussian noise possesses a clear upper bound, given by the constraint that the background of model spectra may not be higher than experimental spectra. An increase in the dynamical noise leads to a rising background. Note that experimental backgrounds vary significantly and are dependent on several factors such as the measurement technique and the experimental setup. However, in the model spectra, the background is well below typical, experimentally observed backgrounds.

We made the assumption of an exponentially correlated bifurcation parameter with zero mean and exponential correlation in space. It is unclear whether those hypotheses are met in nature. We argue that it seems plausible and that we chose a generic description. In particular, there is no estimate of the correlation length. However, we can estimate rough upper bounds for the standard deviation of the bifurcation parameter as we know that spontaneous oscillations should be small. Furthermore, it seems plausible that the BM operates close to a Hopf bifurcation. Thus, the bifurcation parameter should be also small compared to the characteristic frequency. Both conditions are met by the particular choice of the standard deviation of the bifurcation parameter.

It is not clear whether longitudinal coupling of the strength we employed in the model exists in reality and whether it is both elastic and dissipative. Experimental results indicate there is longitudinal coupling, which is mainly elastic. However, it seems plausible that it is also weakly dissipative.

In order to estimate the strength coupling in the model, a transformation to other description of local dynamics is necessary, as the Hopf normal form is an effective, phenomenological description without physiological details. We choose to compare the Hopf normal form to an harmonic oscillator by means of a transformation presented in section 2.3. Dissipative and elastic longitudinal coupling of strengths  $\kappa$  and  $\kappa'$  in the Hopf oscillator correspond to coupling strengths  $|\hat{k}_{el}| = 2m\Omega_0|\kappa|$  and  $|2m\hat{k}_{di}| = |\kappa'|$  in the description of the harmonic oscillator, where  $m$  and  $\Omega_0$  are mass and eigenfrequency of the harmonic oscillator, respectively. In simulations we use  $\kappa = 39$  Hz,  $|\kappa'| = 300$  Hz. For the comparison we choose a medium angular frequency of  $10^4$  Hz. Corresponding to the setup of our model, we choose  $m$  to be the mass of a segment of the cochlear partition of length  $\Delta x = 10\mu\text{m}$ . Estimates for the mass of the cochlear partition vary [106]. However, it can be assumed that the density of the partition is not significantly higher than the density of water, which is  $10^3$  kg/m<sup>3</sup>. The breadth of the partition is about 1 mm. Its height is less than 1 mm, thus the volume is less is not greater than  $10^{-11}$  m, resulting in a mass of less than  $10^{-8}$  kg. Duifhuis gives a value of  $0.5$  kg/m<sup>2</sup> for the areal density of the partition [40],

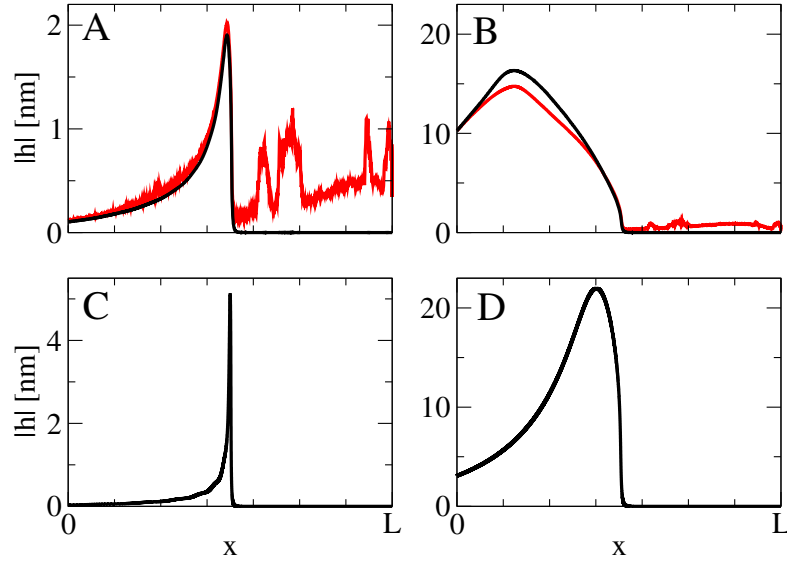


Figure 4.13: **Response of the time and frequency domain models to periodic stimuli of frequency  $f = 1300$  Hz and varying strengths.** A: Maximal BM deflection  $|h|$  as a function of position  $x$  along the cochlea (red line), where the maximum is computed for each position over a small time window, shown together with the magnitude of the Fourier transformation at the driving frequency (black line) for a stimulus of 40 dB SPL. B: Same graph as A but for a stimulus of 80 dB SPL. C,D: Magnitude of the response according to the cochlea model in the frequency domain [41] for 40 dB and 80 dB, depicted in C and D, respectively. Note that all the black lines, which represent either the results of Fourier model or the Fourier transform of the time model, were multiplied by two in order to correspond to the time domain response.

which leads to a mass of  $0.5 \cdot 10^{-8}$  kg. Inserting the value of  $m$  obtained with the parameter from Duifhuis into the above relation for the coupling strengths, we obtain  $\hat{k}_{el} = 0.03$  N/m,  $\hat{k}_{di} = 2 \cdot 10^{-7}$  N/m. Comparing the value of the elastic coupling with results obtained by Dierkes [36], the strength falls into the range of strong coupling of hair bundles.

#### 4.4 Stimulus frequency otoacoustic emissions revisited

As we saw in the previous sections, the model provided with longitudinal coupling can account for SOAEs including its statistics. The question remaining is whether the model can still account for the other three hallmarks of hearing given by an extreme sensitivity, a wide dynamic range, and a sharp frequency selectivity. In this section, we stimulate the system we proposed in this chapter with pure tones and measure its response, showing that this model, which

contains dynamical noise, longitudinal coupling, and disorder in the bifurcation parameter, still works as an 'ear' in the sense that it detects sinusoidal sound stimuli. Stimulating the cochlea with a pure sine tone, Fig. 4.13 shows a good agreement between the Fourier transform of the time series  $h(x, t)$  obtained from the time domain model including irregularities in  $\epsilon$ , indicated by the black lines in A and B, and the solution of the model in frequency space [41], shown in C and D. Thus, the time domain model extends the frequency domain model, hereby ensuring that the time domain model can function as an 'ear' in the sense of a sound detector for pure tones. However, note that there are differences between the responses of the two models. The envelopes in the time domain model are smaller and possess a broader overall shape compared to the model in the frequency domain. Furthermore, graphs 4.13 A and B show that in the time domain model, frequencies other than the stimulus frequency are also present, since the red lines, which denote the maximum of  $|h|$  for a small time window, are larger than the black one, particularly on the right side of the peak. In the frequency domain model no other frequencies are present. Differences between the two models are expected due to several reasons. First of all, the Fourier transform of the time domain model corresponds only in an approximate manner to the model in the frequency domain. Furthermore, the boundary conditions are different as we employ the middle ear boundary condition in the time domain. Besides, in contrast to the frequency domain model, the time domain model comprises dynamical noise, irregularities in the bifurcation parameter, longitudinal coupling. In addition, the values of the nonlinearity  $\beta$  differ. The numerical value of  $\beta$  in the time domain model was chosen such that the SFOAE response of the model resembles the SFOAE response of the basic frequency domain model [41]. Note that the magnitudes of the Fourier modes in Fig. 4.13 were multiplied by two in order to correspond to the time domain snapshot, as the Fourier transform of a sinusoid returns half the amplitude at the driving frequency.

## 4.5 Extensions of the model

Although the final model incorporates diverse biophysical features, such as the middle ear boundary condition, irregularities in the bifurcation parameter, longitudinal coupling, and dynamical noise, we avoided unnecessary modifications to maintain the generic character of the model. However, it might be interesting to consider different extensions and alterations of the model. We discuss statistics of the model 1) without any dynamical noise, 2) with both dynamical additive and phase noise, and, finally, 3) with a negative mean bifurcation value.

In order to obtain the desired statistics of the inter-emission intervals, the frequency distribution and the distribution of the number of emissions per cochlea, it is not necessary to include dynamical noise. For the system without dynamical noise and with otherwise unchanged parameters, we present typical statistics in Fig. 4.14 for an adjusted threshold value of 31 dB of the peak detection criterion,

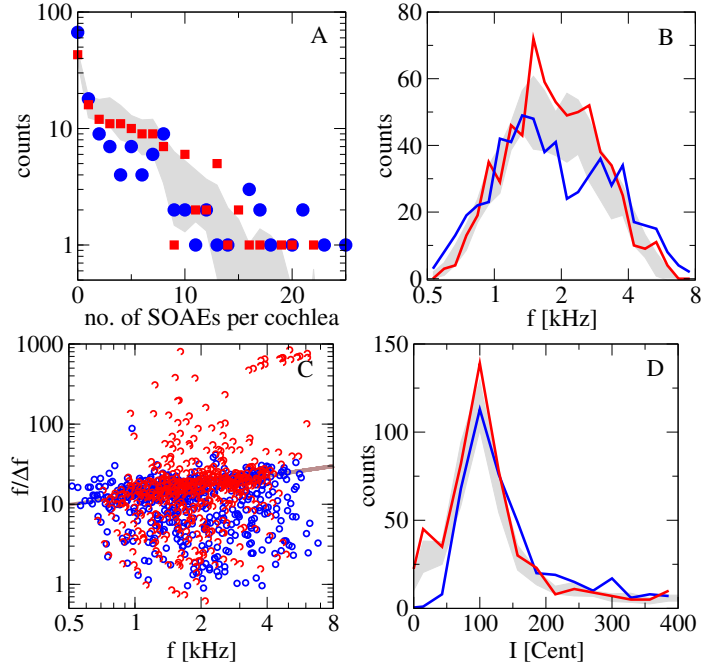


Figure 4.14: **Comparison of the statistics of SOAE frequency, number of SOAEs per cochlea, and inter-emission frequency intervals in experiment (blue) and model without dynamical noise (red).** Data shown for 152 individual ears in experiment and results from the model obtained from 152 realizations of the irregularities. A: Histogram of SOAE number per cochlea. B: Count histograms of emission frequency detected. C: Inverse relative frequency intervals  $\frac{\bar{f}}{\Delta f} = \frac{\sqrt{f_1 f_2}}{|f_2 - f_1|}$ , where  $f_1$  and  $f_2$  are frequencies of two adjacent emissions in the spectrum. The brown line indicates the relation  $\Delta f \sim f^{0.39}$ . D: Histogram of relative frequency intervals, given in units of Cent for the same data as in C. The gray regions in A, B, and D indicate the standard deviation around the average determined from 10 repetitions of 152 realizations. Parameter values are given by the standard parameters, as used for Figs. 4.3, 4.4, 4.9, except for the noise intensity, which is set equal to 0 here.

which is necessary to maintain an average number of SOAEs that corresponds to experimental data. The distributions do not change dramatically. The distribution of SOAE frequencies exhibits a slight second maximum. The histogram of the relative frequency distances between neighboring SOAEs exhibits fewer small distances, see Fig. 4.14 D, compared to the system with dynamical noise. This is in accordance with the observation that the peak separation mechanism is weakened by the presence of dynamical additive white noise. Furthermore, the rise of the threshold value also contributes to the decrease in the number of small distances, which corresponds to the observation that large peaks show a more pronounced separation effect compared to small peaks.

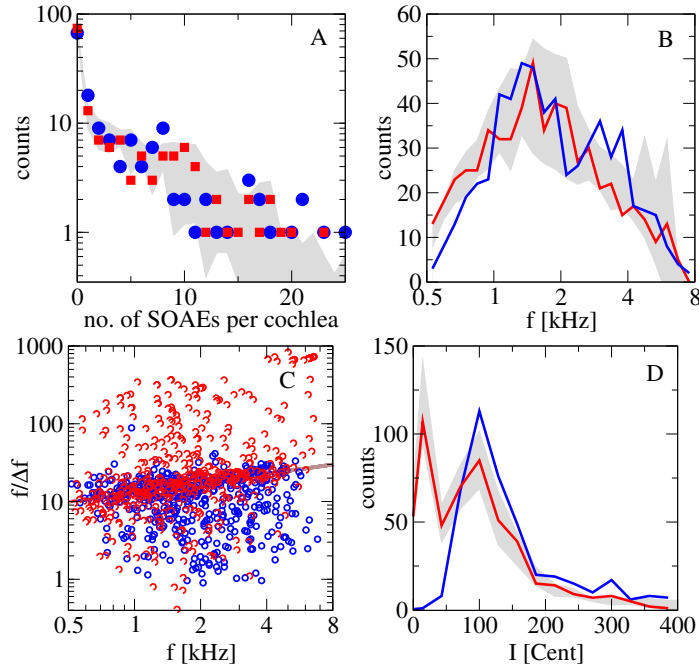


Figure 4.15: **Comparison of the statistics of SOAE frequency, number of SOAEs per cochlea, and inter-emission frequency intervals in experiment (blue) and model with negative mean bifurcation parameter (red).** The panels show the same quantities as explained in Fig. 4.14. Parameter values are given by the standard parameters, as used for Figs. 4.3,4.4,4.9, except for the mean bifurcation parameter  $\bar{\epsilon} = -80$  Hz, and the standard deviation  $\sigma = 97$  Hz.

Thus far we described  $\epsilon(x)$  by an Ornstein-Uhlenbeck process with theoretical mean equal to 0. Though it seems justified to set the mean exactly to 0, it is also possible that the mean bifurcation parameter corresponding to experiments is slightly different from 0. Choosing  $\bar{\epsilon} < 0$  has a regularizing effect on the spectra. Small peaks in the spectrum become less pronounced and thus regions between tall peaks become usually smoother. In case of  $\bar{\epsilon} = 0$ , the prevalence of model cochleae with one or more SOAEs is systematically higher than what is observed in experiments, corresponding to a lower number of realizations without any emissions, see Fig. 4.4. This feature is rather robust, and it appeared in most of the different setups and parameter sets that were investigated during this study. In addition, cochleae with a high numbers of SOAEs are less frequent in the model with  $\bar{\epsilon} = 0$  compared to experimental results. By choosing a slightly negative mean value  $\bar{\epsilon}$ , the agreement of the distribution of the number of SOAEs per cochlea obtained from the model and the experiment improves, see Fig. 4.15 A, compared to the case  $\bar{\epsilon} = 0$ , see Fig. 4.4. In particular, the

prevalence of cochleae with at least one SOAE can be captured which is equivalent to matching the number of cochleae with zero SOAEs. Furthermore, model cochleae with high numbers of SOAEs become more frequent.

The distribution of emission frequencies and the distribution of inter-emission intervals remain similar, see Fig. 4.15 B-D. Though, small inter-emission intervals become more likely, whereas large ones become slightly less frequent.

However, in order to keep the average number of emissions constant, choosing  $\bar{\epsilon} < 0$  needs to be compensated by an increase in  $\sigma$ . Thus, long excursions of an elevated level of the power spectra become more likely, by which we mean large frequency intervals of several hundred up to 1000 Hz in which all points in the spectrum lie above the background level.

In the following, we consider the model subjected to an additional noise source. The model system with the standard parameters including the standard strength of the additive noise exhibits unrealistically high quality factors centering around  $10^5$ , see Fig. 4.11, in comparison to experimental quality factors, which center around 100. This discrepancy might be partly due to other noise sources being present in the real cochlea, which are not captured by additive white noise. One possible candidate for a not captured noise source is the cardiovascular activity, in particular the heart beat, which modulates the blood pressure and is known to influence SOAEs [83]. Such noise sources might be more appropriately modeled by phase noise, which we investigate below.

We model the system with the standard parameters in presence of phase noise, which we describe by an additional term  $i\eta(t)z_j$  in Eq. (4.7), where  $\eta(t)$  is an Ornstein-Uhlenbeck process in time acting globally on all oscillators. Its standard deviation is  $\sigma_{pn}$  and the correlation time is 1 second. Thus, the local oscillator dynamics reads

$$\begin{aligned} \frac{dz_j}{dt} = & (\epsilon_j + i\omega(x_j) + i\eta(t))z_j - \frac{\beta}{\alpha}|z_j|^2 z_j \\ & + (\kappa + i\kappa')(z_{j+1} - 2z_j + z_{j-1}) + \xi(x_j, t) - \frac{i}{\alpha}p_j. \end{aligned} \quad (4.7)$$

We simulate the system including phase noise by simulating each local oscillator with an effective local frequency  $\omega(x_j) + \eta(t)$ . The statistics of this system, which is subject to global phase noise as well as additive white noise, is depicted in Fig. 4.16. In general, the distribution of the number of emissions, the distribution of emission frequencies and distribution of the inter-emission intervals do not differ drastically from the system without phase noise. However, small distances between adjacent emissions become less likely. This effect is facilitated by the increased width of SOAEs. Two narrow emissions which are very close to each other in the system without phase noise are not discriminable anymore in the presence of the phase noise if their distance is sufficiently small compared to the typical width of emissions caused by phase noise. In this case, the two emissions merge into one common emission.

Employing such noise leads indeed to a scatterplot of quality factor values that corresponds well to experimental data, see Fig. 4.17 A, and to a correct mean

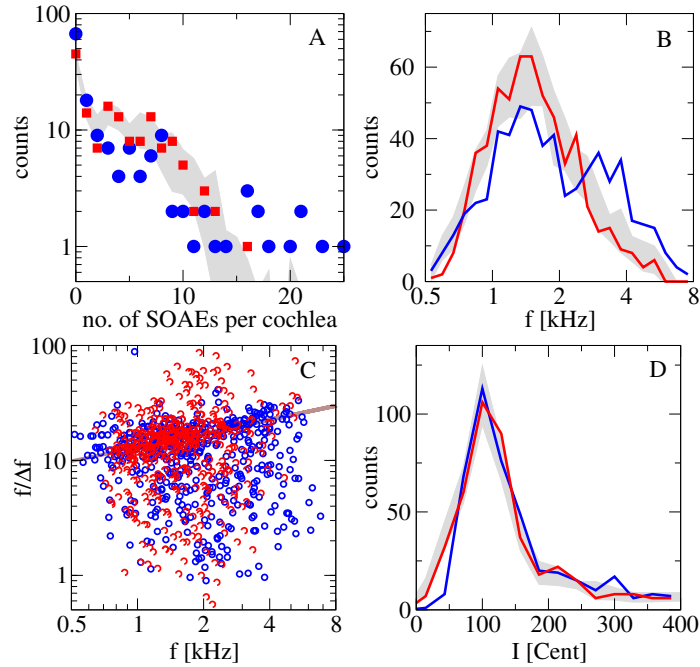


Figure 4.16: **Comparison of the statistics of SOAE frequency, number of SOAEs per cochlea, and inter-emission frequency intervals in experiment (blue) and model with phase noise (red).** The panels show the same quantities as explained in Fig. 4.14. Standard parameters are used (as for Figs. 4.3, 4.4, 4.9) except for the phase noise, which possesses a correlation time of 1 Hz and a standard deviation of 35 Hz. The SOAE detection threshold value is set to 9.5 dB.

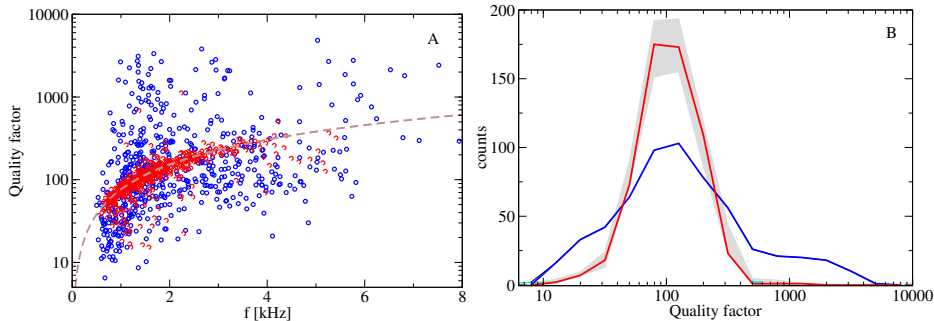


Figure 4.17: **Statistics of the quality factor in experiment (blue) and model in case of phase noise (red).** A: Scatterplot of quality factors as a function of frequency. The dashed brown line indicates the theoretical prediction  $Q = f/\lambda$ , where  $\lambda \approx 13$  Hz. B: Distribution of quality factors for the same data as in A. Standard parameters are used with an adjusted SOAE detection threshold value of 9.5 dB. Data from the same simulations as in Fig. 4.16

value of the quality, see Fig. 4.17 B. Furthermore, in both experiment and model the quality factors increase as a function of frequency, see Fig. 4.17 A. However, the distribution of quality factors in the model is narrower compared to the experimental quality factors, which span three orders of magnitude, despite the fact that SOAEs frequencies span only slightly more than one order of magnitude. This suggests that the question of how to represent noise is more complex in reality. The narrower distribution of the quality factors of the model can be explained by the limited range of SOAE frequencies and the similar width for all SOAEs, as the phase noise acts globally on all oscillators.

The width of the Gaussian distribution with mean  $\mu$  and  $\sigma$  is given by  $2\sigma\sqrt{2\ln(2)}$ . Assuming that the widths of the model SOAEs are solely determined by the standard deviation of the phase noise, the width of a SOAE can be approximated by  $2\sigma_{pn}\sqrt{2\ln(2)}/2/\pi$ , which we define as  $\lambda$ . The quality factors obtained from the model scatter around the theoretical approximation  $Q = f/\lambda$ , indicated by the brown dashed line in Fig. 4.17, showing a good agreement between model and theory.

It might be interesting to investigate other noise types or phase noise that is not global but contains some spatial variation. This might lead to an increased width of the distribution of quality factors in the model. In addition, investigating different functions governing the irregularities in  $\epsilon$  might provide new insights. Furthermore, it is likely that the bifurcation parameter  $\epsilon$  which corresponds to activity in the experiment is not static but changes slightly with time, as power spectra of the pressure in the ear canal are known to be stable with respect to the frequency of the emissions but not necessarily very stable with respect to the amplitude of the emissions. Indeed, emission amplitudes in experiments change over the course of time on various different time scales. Incorporating a time-dependent  $\epsilon$  might improve the correspondence between model and experiments. Moreover, the combination of irregularities in the bifurcation parameter and the characteristic frequency might represent a more realistic, biophysical model.

## Chapter 5

# Summary and conclusions

The auditory systems of numerous species including humans exhibit remarkable properties. Mammalian hearing is characterized by four hallmarks, given by an extreme sensitivity, a wide dynamic range, a sharp frequency selectivity, and spontaneous otoacoustic emissions (SOAEs). The last-mentioned are sounds which are generated by the cochlea, the hearing organ within the inner ear, in absence of external stimulation and become manifest as pressure fluctuations in the ear canal. The four characteristics, in particular SOAEs, are associated with an active nonlinear amplification process taking place on a mechanical level in the cochlea.

In this thesis, we extended the generic one-dimensional cochlea model which was proposed by T. Duke and F. Jülicher [41]. This model is set up in the frequency domain, and it represents the active nonlinear human cochlea by a chain of critical oscillators coupled via hydrodynamic interactions. It does not aim for describing each detail of the cochlea as for instance some three-dimensional models with finite element methods do. In contrast, the model aims for an effective description of cochlear geometry and the essential biophysical principles that shape the mechanics of hearing. As this model is formulated in the frequency domain, only cyclo-stationary inputs and responses can be considered. It was found that this model accounts for three of the four hallmarks of hearing, with the exception of spontaneous emissions, which were not investigated.

We proposed a spatially discrete model in time space whose Fourier transform corresponds to the above frequency domain model. Our goal was to describe the fourth, remaining hallmark, spontaneous emissions including its main statistics, and thus eventually account for all four hallmarks of hearing by means of our generic model. We investigated hydrodynamic principles of the cochlea which were applied in both the time domain and the frequency domain model. The hydrodynamic equations we employed are valid in the long wavelength approximation, which assumes that the wavelength of the traveling wave is large compared to the channel height. However, for a traveling wave elicited by a pure tone this does not hold true for locations in the vicinity of the resonance.

---

We made additional approximations by assuming incompressibility and negligible viscosity of the fluid within the upper and lower chamber. Although this seems plausible, it might be interesting to take compressibility and viscosity into account.

Furthermore, we discussed the description of local dynamics in the time domain model, and we justified the usage of the Hopf normal form in time space. We performed an equidistant discretization of the model equations along the longitudinal axis of the cochlea, where each of the 3501 segments contains a set of one inner and three to five outer hair cells. Thus, we arrive at a chain of one-dimensional chain of oscillators, whose local dynamics are governed by the Hopf normal form. Like the previously proposed model in the frequency domain, our time domain model does not describe the details of the cochlear micromechanics, nor does it take details of the cochlear geometry into account. In particular, active hair bundle motility, electromotility, and their interplay are not captured by our model. The chosen number of segments in the model corresponds to the average number of natural segments of the organ of Corti and the basilar membrane. However, hair cell widths and thus also segment lengths vary along the cochlea and increase for locations closer to the apex [21]. Changing the discretization in the model might alter the dynamics and responses of the model. Subsequently, we provided procedures to simulate the proposed model system forward in time. We verified that the time domain model corresponds to the frequency domain model by investigating responses to pure tone stimulations. Moreover, forward and reverse traveling waves were determined at the base in the model. In particular, it was shown how to extract incoming pressure waves in the frequency and time domain. The model exhibits low frequency modes, present as spontaneous global basilar membrane oscillations in presence of additive white noise. On grounds of theoretical considerations, these modes were identified as the fundamental mode and the first harmonic of the system.

Albeit the above wave analysis is useful for calculating forward and reverse traveling waves, there is a more suitable framework to study SOAEs and incoming waves. We introduced a boundary condition proposed by Talmadge et al. [148], which corresponds better to the experimental setup. Henceforth, we employed this boundary condition, which involves the representation of the middle ear by a harmonic oscillator and a force balance equation at the base. It facilitates comparison with experiments by enabling us to treat and determine the pressure in the ear canal as an observable rather than an input variable. By incorporating this boundary condition, the modes of the model become manifest in pronounced peaks in the power spectrum of the pressure in the ear canal. It was shown that the response of the cochlea model to pure tones is consistent with the physiological response, though the generic description of the model cannot capture all details of the experimentally observed motion. The fit to specific experimental data might be improved by considering frequency-, location-, or strength-dependent parameters, which we did not investigate in order to focus on the generic properties of our model. Furthermore, we introduced elastic and dissipative longitudinal coupling of oscillators, accounting for experimental evidence of tissue connectivity via different structures. However,

there are inconsistent experimental results regarding the strength and relevance of longitudinal coupling are. In addition, it is yet unclear by which tissues the coupling is mediated. Plausible candidates are given by the tectorial membrane, the reticula lamina and the basilar membrane.

Elastic and dissipative longitudinal coupling have been used previously to account for minimal frequency differences between neighboring SOAEs in lizards. In this thesis, we employed longitudinal coupling in the human cochlea to account for the minimal frequency spacing between neighboring SOAEs. Irregularities in parameters have been claimed to be an important mechanism for the generation of mammalian SOAEs and their preferred minimal distance, postulated to cause back-scattering of the traveling waves and as a result spontaneous otoacoustic emissions emerge as a global phenomenon. We investigated this idea in the framework of our proposed model, finding strong numerical evidence that solely disorder in the bifurcation parameter governing the local activity can account for spontaneous emissions. However, we cannot exclude that spontaneous emissions are elicited by a mechanism which involves processes we did not consider or which cannot be adequately described by our generic model. For instance, it has been proposed that time-delayed stiffness can lead to spontaneous emissions.

The final version of the model incorporates longitudinal coupling, dynamical noise and irregularities in the bifurcation parameter. We assumed that static irregularities of the bifurcation parameter are normally distributed around zero and exponentially correlated in space, thereby lending individuality to each realization of the cochlea model.

All but five parameter values of the resulting model were fixed by experimental evidence. These five free parameters were given by the strength of the dynamical noise, the strength of the dissipative and elastic coupling, and the standard deviation and correlation length of the static (time-independent) irregularities in the bifurcation parameter. The strength of the dynamical noise did not play an essential part, and it was mainly employed for a regularizing effect. The remaining free parameters were used to match statistics observed for experimental SOAEs. In experiments on 152 cochleae by C.L. Talmadge [146], emission frequencies range from 500 Hz up to 8000 Hz. The distribution of the number of emissions per cochlea is monotonically decaying and follows roughly an exponential shape. Furthermore, there is a preferred minimal distance of one semitone between the frequencies of neighboring SOAEs, exhibiting a trend towards smaller values for higher frequencies.

The standard deviation and the correlation length of the irregularities in the bifurcation parameter strongly influence the statistics of the number of SOAEs per cochlea, in particular the average number of emissions. Both parameters also have an effect on the distribution of the frequencies of emissions. Furthermore, the statistics of the inverse, relative frequency intervals between neighboring emissions is predominantly controlled by the coupling strengths. For some sets of the free parameters, we were able to simultaneously match the distribution of SOAE frequencies, the number of SOAEs per cochlea, and the relative, inverse distance between neighboring SOAEs including its trend. Despite the good cor-

response, there remain some discrepancies, some of which can be resolved by extending the model. In contrast to experimental spectra, some model spectra display long regions of more than 100 Hz for which the spectrum rises above the background. This fact is associated with the length of the regions with a positive bifurcation parameter. Furthermore, the model spectra display more small peaks than experimental spectra, which display only few emissions on top of a smooth background spectrum. Note that we did not aim for a description of the background. The range of SOAE frequencies is well matched. However, the experimental distribution is bimodal with two maxima at 1.5 kHz and 3 kHz, whereas the model distribution exhibits only one strong maximum at 1.5 kHz. A second maximum at 3 kHz was only occasionally present in some sets of the 152 model cochleae. The experimental maximum at 3 kHz was attributed to a resonance in the ear canal. As we treat the pressure in the ear canal as a scalar, uniform quantity, we do not capture this resonance. The statistics of the number of emissions per cochlea obtained from model and experiment are similar, both exhibiting a monotonic decay of roughly exponential shape. Nevertheless, the model predicts a higher prevalence of humans with SOAEs. Furthermore, the probability of a high number of emissions per cochlea is higher in experiment than in the model, in particular for emission numbers greater than 15. This discrepancy is associated with the chosen distribution of the bifurcation parameter in the model which might not perfectly describe the corresponding experimental quantity. We found that changing the mean value of the bifurcation parameter from 0 to a slightly negative value leads to a better agreement of the distribution of the numbers of SOAEs including the prevalence of cochlea with at least one emission and the number of cochleae with numerous emissions. This might indicate that the bifurcation parameter corresponding to experimental data is on average in the proximity of the critical point but still in the stable regime. However, note that the prevalence of SOAEs is highly dependent on measurement techniques and detection criteria. It is plausible to assume that the local activity and thus the experimental equivalent to the bifurcation parameter exhibits inhomogeneities. However, the source is not clear. While Gaussian statistics and an exponential correlation are reasonable assumptions, there is no evidence supporting this ansatz. Put differently, the distribution of the experimental quantity that corresponds to the bifurcation parameter is not known. Besides, it is unclear whether there is significant spatial correlation. According to the model, the local activity is associated to SOAEs, which in turn exhibit several remarkable features that have to be in accordance with the notion of the inhomogeneities we propose. SOAE profiles are influenced by genetics, a result obtained by studying mono- and dizygotic twins. Moreover, SOAEs in the two ears of individuals display correlations in both frequency and number. This might be due to genetic factors or due to the influence of afferent neurons, directing signals from the brain towards the cochlea. Additionally, individual SOAEs vary both in frequency and amplitude over time. Frequencies change over various different time scales and systematically decrease over the course of years. These aspects are not understood yet and are not captured by our model. Fluctuations in the amplitude might be captured by non-static bifurcation ir-

regularities in the model.

The power of the emissions in model and experiment are comparable. Though, experimental SOAEs were reported to reach higher maximal strengths than in the model. However, there are several sources of approximations and uncertainties that influence the power of the model emissions, such as the middle ear, which we represent in our model by an harmonic oscillator. It has been shown that the middle ear is more complex than a harmonic oscillator, in particular regarding its forward and reverse transmission properties. Additionally, the power of emissions is influenced by the peak criterion, i.e., which peaks are accepted as SOAEs.

We discussed several extensions of our model and showed that the experimental statistics can be also captured by the model system without dynamical noise. One statistical feature the model cannot account for is given by the distribution of the quality factors of SOAEs. Each emission corresponds to a peak in the power spectrum. The quality factor of a peak is defined as the ratio of its center frequency to its width. In the model, quality factors are three orders of magnitude higher, centering around  $10^5$ , than what is observed in experiments, where values center around  $10^2$ . By incorporating global phase noise, the mean of the experimental quality factor distribution could be matched, but the width of the quality factor distribution in the model is slightly smaller compared to experiments.

According to the model, there is a fundamental mode present in the system. Due to several uncertainties, it might be intricate to verify this prediction experimentally. The frequency of the fundamental mode depends on the length of the individual cochlea. However, experiments find a natural variation of several millimeters in cochlea length. Furthermore, in the model simplifying assumptions were made regarding the local best frequencies, which influence the fundamental mode. The lowest eigenfrequency of the model cochlea is slightly above 100 Hz, whereas experimental best frequencies reach as low as 20 Hz. For an eigenfrequency as low as 20 Hz, the assumptions of the approximation are not fulfilled. Furthermore, diverse physiological noise sources are present in experiments, which might lead to peaks in the power spectrum which do not originate in the inner ear.

In addition, the model predicts the time course of the build up of basilar membrane vibrations in response to pure tone stimulation. In particular, it predicts the required time to reach a steady state. However, this has not been investigated experimentally hitherto.

In the model, spontaneous basilar membrane activity is associated with the bifurcation parameter. In particular, if a region of the basilar membrane displays spontaneous oscillations which are not due to the fundamental mode of the system, then the irregularities in the bifurcation parameter in that specific region are positive. The model requires active local oscillators as a source for SOAEs. Put differently, if a SOAE is present in the power spectrum of the pressure in the ear canal in the model, the oscillators in the area of the basilar membrane with

---

the corresponding local best frequency are active. Thus, the model requires that if a power spectrum from experiment exhibits a peak, then the corresponding, possibly isolated, section of the basilar membrane is vibrating spontaneously. The model could be falsified if these single sections with intact amplification mechanism would not exhibit spontaneous oscillatory motion. This correspondence between a peak in the power spectrum and local spontaneous oscillation of the basilar membrane has been established for one SOAE in a cochlea of a guinea pig [111].

The model does not predict the source of spontaneous basilar membrane vibrations, but a reasonable guess is that spontaneous oscillations of stereocilia elicit this spontaneous motion. However, partly due to the small dimensions of mammalian stereocilia, spontaneous oscillations of mammalian hair bundles have not been observed to the present date.

One other prediction is that an increase in dynamical, additive noise leads to a less effective peak separation. However, this is difficult to test in experiment. For instance, a rise in temperature in experiment, which might be associated with a higher additive noise in the model, might also lead to other effects such as changes in SOAE frequencies. Furthermore, the model predicts that elastic and dissipative longitudinal coupling play an essential role for the observed peak separation of spontaneous otoacoustic emissions. It would be interesting to probe this hypothesis by altering elastic and dissipative coupling in experiments without changing other system properties. This seems rather intricate, and for obtaining statistics this would have to be done in many specimens. However, it might be possible to test this hypothesis in single lizard ears exhibiting SOAEs by manipulating or removing the tectorial membrane and thus possibly changing longitudinal coupling. Changes in SOAE spectra might indicate the dependence of the frequency spacing on longitudinal coupling. Furthermore, it would be of interest to study inter-emission intervals in different lizard species as the family of lizards comprises species with and without a tectorial membrane. Alternatively, transgenic mice, some of which lack a tectorial membrane structure, could be employed to test the hypothesis of peak separation by means of longitudinal coupling. However, the peak separation phenomenon might still be present in mice which lack a tectorial membrane due to the presence of other connective tissues, such as the basilar membrane or the reticular lamina.

In conclusion, this dissertation presents an active nonlinear model of the cochlea in the time domain, which can account for all four hallmarks of the human auditory system. Furthermore, this model captures essential statistics of SOAEs including the remarkable finding of a preferred minimal distance between neighboring SOAEs. We find that spontaneous emissions are consistent with the notion of active oscillators out of thermodynamic equilibrium. Thus, by proposing this model we make a contribution to the deeper understanding of spontaneous emissions with implications on cochlear mechanics in general. Further investigation on model properties, predictions of the model, and comparison to different experimental data provide interesting topics for future research.

# Bibliography

- [1] Ablowitz M. J., Clarkson P. A. (1991) Solitons, Nonlinear Evolution Equations and Inverse Scattering. London Mathematical Society Lecture Notes 149, Cambridge University press.
- [2] Andor D. (2005) Energy transport, reflections and noise in the active cochlea. Dissertation, Cambridge.
- [3] Andor D., Duke T., Simha A., Jülicher F. (2006) Wave Propagation by Critical Oscillators. In Auditory Mechanisms - Processes and Models, Proceedings of the Ninth International Mechanics of Hearing Workshop Portland, Oregon, Nuttall A.L., Ren T., Gillespie P., Grosh K., de Boer E. (Eds.).
- [4] <http://audres.org/downloads/cochlea100.jpg>, accessed on April 15, 2013.
- [5] Ashmore J. (2002) The mechanics of hearing. In: *Signals and Perception: The Fundamentals of Human Sensation*, Roberts D. (Ed.) Palgrave Macmillan Limited.
- [6] Ashmore J. (2008) Cochlear Outer Hair Cell Motility. *Physiol Rev* 88: 173-210.
- [7] Ashmore J., Avan P., Brownell W.E., Dallos P., Dierkes K., Fettiplace R., Grosh K., Hackney C.M., Hudspeth A.J., Jülicher F., Lindner B., Martin P., Meaud J., Petit C., Santos-Sacchi J., Canlon B. (2010) The remarkable cochlear amplifier. *Hear Res.*, 266(1-2): 1-17.
- [8] Avitabile D., Homer M., Champneys A. R., Jackson J. C., Robert D. (2010) Mathematical modelling of the active hearing process in mosquitoes. *J. R. Soc. Interface*, 7: 105-122.
- [9] Barral J., Dierkes K., Lindner B., Jülicher F., Martin P. (2010) Coupling a sensory hair-cell bundle to cyber clones enhances nonlinear amplification. *Proc. Natl. Acad. Sci. USA*, 107: 8079-8084.
- [10] Bender, C.M.; Orszag, S.A. (1999) Advanced mathematical methods for scientists and engineers. Springer Verlag.
- [11] von Békésy, G. (1928) Zur Theorie des Hörens. Die Schwingungsform der Basilarmembran. *Phys. Z.* 29: 793-810.

- [12] von Békésy, G. (1944) Über die Frequenzauflösung in der menschlichen Schnecke. *Acta Otolaryngol* 32: 60-84.
- [13] von Békésy, G. (1947) The variation of phase along the basilar membrane with sinusoidal vibration. *J. Acoust. Soc. Am.* 19: 452-460.
- [14] von Békésy, G. (1960) Experiments in Hearing. McGraw-Hill, New York.
- [15] von Békésy, G. (1961) Concerning the pleasures of observing, and the mechanics of the inner ear. Nobel lectures, Physiology or Medicine 1942-1962. Elsevier, Amsterdam.
- [16] Bergevin C., Shera C. A. (2010) Coherent reflection without traveling waves: On the origin of long-latency otoacoustic emissions in lizards. *J. Acoust. Soc. Am.* 127 (4): 2398-2409.
- [17] Bergevin C., Fulcher A., Richmond S., Velenovsky D., Lee J. (2012) Interrelationships between spontaneous and low-level stimulus-frequency otoacoustic emissions in humans. *Hear Res.* 285(1-2): 20-28.
- [18] Bialek W., Wit H.P. (1984) Quantum limits to oscillator stability: Theory and experiments on acoustic emissions from the human ear. *Phys. Lett. A*, 104: 173-178.
- [19] Braun M. (1997) Frequency spacing of multiple spontaneous otoacoustic emissions shows relation to critical bands: a large-scale cumulative study. *Hear. Res.* 114: 197-203.
- [20] Braun M. (2006) A retrospective study of the spectral probability of spontaneous otoacoustic emissions: Rise of octave shifted second mode after infancy. *Hear. Res.* 215: 39-46.
- [21] Bredberg G. (1968) Cellular pattern and nerve supply of the human organ of Corti. *Acta Oto-Laryngol., Suppl.* 236: 1-135.
- [22] Brekhovskikh, L.M. (1980). Waves in Layered Media. Academic Press.
- [23] Brownell W.E., Bader C.R., Bertrand D., de Ribaupierre Y. Evoked mechanical responses of isolated cochlear outer hair cells. *Science*, 227: 194-196.
- [24] Burns E.M. (2009) Long-term stability of spontaneous otoacoustic emissions. *J. Acoust. Soc. Am.* 125(5): 3166-3176.
- [25] Camalet S., Duke T., Jülicher F., Prost J. (2000) Auditory sensitivity provided by self-tuned critical oscillations of hair cells. *Proc. Natl. Acad. Sci.* 97: 3183-3188.
- [26] Chen Z.X., Guo, G.Y. (1992) Analytic solutions of the Nagumo equation *IMA J. Appl. Math.*, 48: 107-115.

- [27] Chen F., Cohen H.I., Bifano T.G., Castle J., Fortin J., Kapusta C., Mountain D.C., Zosuls A., Hubbard A.E. (2006) A hydromechanical biomimetic cochlea: experiments and models. *J. Acoust. Soc. Am.* 119(1): 394-405.
- [28] Corti A. (1851) Recherches sur l'organe de l'ouïe des mammiferes. *Z. Wiss. Zool. Abt. A.* 3: 109-169.
- [29] Crawford A.C., Fettiplace R. (1985) The mechanical properties of ciliary bundles of turtle cochlear hair-cells. *J. Physiol.* 364: 359 -379.
- [30] Czinner, H.I., Hammerschlag, V. (1897) Beitrag zur Entwicklungsgeschichte der Corti'schen Membran. *Sitzungsberichte der Kaiserlichen Akademie der Wissenschaften mathematisch-naturwissenschaftlichen Classe*, Band CVI, Abtheilung III, Abteilung 3.
- [31] Dallmayr C. (1985) Spontane oto-akustische Emissionen: Statistik und Reaktion auf akustische Störtöne. *Acustica*, 59: 67-75.
- [32] Dallos P. (1992) The active cochlea. *J Neurosci* 12: 4575- 4585.
- [33] de Boer E. (1980) Auditory physics. Physical principles in hearing theory. I *Phys. Rep.* 62: 87-174.
- [34] de Boer E. (1996) Mechanics of the Cochlea: Modeling Efforts. In: *The Cochlea*, P. Dallos, A.N. Popper, and R.R.. Fay (Eds.), Springer-Verlag. p. 258-317.
- [35] Dierkes K., Lindner B., Jülicher F. (2008) Enhancement of sensitivity gain and frequency tuning by coupling of active hair bundles. *Proc. Natl. Acad. Sci.* 105: 18669-18674.
- [36] Dierkes K. (2010) Nonlinear amplification by active sensory hair bundles. Dissertation, Technical University Dresden.
- [37] Dong W., Olson E.S. (2006) Middle ear forward and reverse transmission in gerbil. *J. Neurophysiol.* 95(5): 2951-2961.
- [38] Dong W., Decraemer W. F., Olson E.S. (2012) Reverse Transmission along the Ossicular Chain in Gerbil. *J. Assoc. Res. Otolaryngol.* 13: 447-459.
- [39] Dorland W.A.N. (2007) Dorland's Illustrated Medical Dictionary, Edition 31. Elsevier Saunders, Philadelphia, Pennsylvania, USA.
- [40] Duifhuis H. (2012) Cochlear Mechanics. Introduction to a Time Domain Analysis of the Nonlinear Cochlea. Springer-Verlag.
- [41] Duke T., Jülicher F. (2003) Active Traveling Wave in the Cochlea. *Phys. Rev. Lett.* 90: 158101.
- [42] Duke T., Jülicher F. (2008) Critical oscillators as active elements in hearing. In: *Active Processes and Otoacoustic Emissions in Hearing*, Manley G.A., Fay R.R., Popper A.N. (Eds.), Springer-Verlag, Heidelberg.

- [43] Eguíluz, V. M., Ospeck M., Choe Y., Hudspeth A.J., Magnasco M.O. (2000) Essential Nonlinearities in Hearing. *Phys. Rev. Lett.* 84: 5232-5235.
- [44] Elliott S.J., Ku E.M., Lineton B. (2007) A state space model for cochlear mechanics. *J. Acoust. Soc. Am.* 122: 2759-2771.
- [45] Epp B., Verhey J.L., Mauermann M. (2010) Modeling cochlear dynamics: Interrelation between cochlea mechanics and psychoacoustics. *J. Acoust. Soc. Am.* 128(4): 1870-1883.
- [46] Fay J.P., Puria S., Steele C.R. (2006) The discordant eardrum. *Proc. Natl. Acad. Sci. USA*, 103 (52): 19743-19748.
- [47] Fritze W., Fritze P., Gedlicka W. (1992) The time course of spontaneous otoacoustic emissions. *Eur Arch Otorhinolaryngol.* 249(1): 20-23.
- [48] Fukazawa T., Tanaka Y. (1996) Spontaneous otoacoustic emissions in an active feed-forward model of the cochlea. *Hear. Res.* 95: 135-143.
- [49] Givelberg E., Bunn J. (2003) A comprehensive three-dimensional model of the cochlea. *J. Comp. Phys.* 191: 377-391.
- [50] Gold T. (1948) Hearing. II. The physical basis of the action of the cochlea. *Proc. R. Soc. London B* 135: 492-498.
- [51] Goode R.L., Killion M., Nakamura K., Nishihara S. (1994) New knowledge about the function of the human middle ear: Development of an improved analog model. *Am. J. Otol.* 15 (2): 145-154.
- [52] Göpfert M. C., Humphris A. D. L., Albert J. T., Robert D., Hendrich O. (2005) Power gain exhibited by motile mechanosensory neurons in *Drosophila* ears. *Proc. Natl. Acad. Sci. USA*, 102: 325-330.
- [53] Griffiths G.W., Schiesser W.E. (2011) *Traveling Wave Analysis of Partial Differential Equations: Numerical and Analytical Methods with Matlab and Maple.* Academic Press, Oxford, UK.
- [54] Hempstead R.D., Lax M. (1967) Classical Noise. VI. Noise in Self-Sustained Oscillators near Threshold. *Phys. Rev.* 161: 350-366.
- [55] von Helmholtz, H. (1863) *Die Lehre von den Tonempfindungen als physiologische Grundlage für die Theorie der Musik.* Vieweg, Braunschweig, 1863.
- [56] Holt J.R., Gillespie S.K.H., Provance Jr. D.W., Shah K., Shokat K.M., Corey D.P., Mercer J.A., Gillespie P. G. (2002) A chemical-genetic strategy implicates myosin-1c in adaptation by hair cells. *Cell*, 108(3): 371-381.
- [57] Hudspeth A.J. (1989) How the ear's works work. *Nature*, 341: 397-404.
- [58] Hudspeth A.J. (2008) Making an effort to listen: mechanical amplification in the ear. *Neuron* 59: 530-545.

- [59] Hudspeth A.J., Jülicher F., Martin P. (2010) A Critique of the Critical Cochlea: Hopf-a Bifurcation-Is Better Than None. *J. Neurophysiol.* 104: 1219-1229.
- [60] Jaffer T.S.A. (2000) Longitudinal elasticity of the cochlear partition and distortion product otoacoustic emissions. Dissertation, University of Toronto.
- [61] Jaffer T.S.A., Kunov H., Wong W. (2002) A model cochlear partition involving longitudinal elasticity. *J. Acoust. Soc. Am.* 112 (2): 576-589.
- [62] Johnstone B.M., Boyle A.J. (1967) Basilar membrane vibration examined with the Mössbauer technique. *Science* 158: 389-390.
- [63] Johnstone B.M., Patuzzi R., Yates G.K. (1986) Basilar membrane measurements and the travelling wave. *Hear. Res.* 22: 147-153.
- [64] Jülicher F., Andor D., Duke T. (2001) Physical basis of two-tone interference in hearing. *Proc. Natl. Acad. Sci.* 98: 9080-9085.
- [65] Jülicher F., Dierkes K., Lindner B., Prost J., Martin P. (2009) Spontaneous movements and linear response of a noisy oscillator. *Eur. Phys. J. E* 29(4): 449-460.
- [66] Kandel E.R., Schwartz J.H., Jessell T.M. (2000) Principles of neural science, 4th Ed. McGraw-Hill Professional, New York.
- [67] Kemp, D.T. (1978) Stimulated acoustic emissions from within the human auditory system. *J. Acoust. Soc. Am.* 64: 1386-1391.
- [68] Kemp, D.T. (1979) Evidence of Mechanical Nonlinearity and Frequency Selective Wave Amplification in the Cochlea. *Arch. Otorhinolaryngol.* 224: 37-45.
- [69] Kemp, D.T. (1979) The evoked cochlear mechanical response and the auditory microstructure - Evidence for a new element in cochlear mechanics. *Scand. Audiol. Suppl.* 9: 35-47.
- [70] Kemp D.T. (2002) Otoacoustic emissions, their origin in cochlear function, and use. *Br. Med. Bull.*, 63 (1): 223-241.
- [71] Kern A. (2003) A Nonlinear Biomorphic Hopf-Amplifier Model of the Cochlea. Dissertation, Swiss Federal Institute of Technology Zurich.
- [72] Kern A., Stoop R. (2003) Essential Role of Couplings between Hearing Nonlinearities. *Phys. Rev. Lett.* 91(12): 128101.
- [73] Köppl C., Manley G.A. (1992) Functional consequences of morphological trends in the evolution of lizard hearing organs. In: *The Evolutionary Biology of Hearing*, Fay, R.R., Popper A.N., Webster D.B. (Eds.), Springer-Verlag, New York. p. 489-509.

- [74] Köppl C., Manley G. (1993) Spontaneous otoacoustic emissions in the bob-tail lizard. I: General characteristics. *Hear. Res.* 71: 157-169.
- [75] Kolston P.J., de Boer E., Viergever M.A., Smoorenburg G.F. (1990) What type of force does the cochlear amplifier produce? *J. Acoust. Soc. Am.* 88(4): 1794-1801.
- [76] Kros C.J., Marcotti W., van Netten S.M., Self T.J., Libby R.T., Brown S.D.M., Richardson G.P., Steel K.P. (2002) Reduced climbing and increased slipping adaptation in cochlear hair cells of mice with Myo7a mutations. *Nat. Neurosci.* 5: 41-47.
- [77] Ku E.M., Elliott S.J., Lineton B. (2008) Statistics of instabilities in a state space model of the human cochlea. *J. Acoust. Soc. Am.* 124: 1068-1079.
- [78] Ku E.M., Elliott S.J., Lineton B. (2009) Limit cycle oscillations in a non-linear state space model of the human cochlea. *J. Acoust. Soc. Am.* 126: 739-750.
- [79] Kudryashov N.A., Sinelshchikov D.I. (2012) Exact solutions of the Swift-Hohenberg equation with dispersion. *Comm. Nonlinear. Sci. Numer. Simulat.* 17(1): 26-34.
- [80] Lindner B., Dierkes K., Jülicher F. (2009) Local Exponents of Nonlinear Compression in Periodically Driven Noisy Oscillators. *Phys. Rev. Lett.* 103: 250601.
- [81] Lighthill J. (1981) Energy flow in the cochlea. *J. Fluid Mech.* 106, 149-213.
- [82] Liu Z., Li B., Lai Y. (2012) Enhancing mammalian hearing by a balancing between spontaneous otoacoustic emissions and spatial coupling. *Europhys. Lett.* 98: 20005.
- [83] Long G.R., Talmadge C.L. (1997) Spontaneous otoacoustic emission frequency is modulated by heartbeat. *J. Acoust. Soc. Am.* 102: 2831-2848.
- [84] Mammano F., Nobili R. (1993) Biophysics of the cochlea: Linear approximation. *J. Acoust. Soc. Am.* 93: 3320-3332.
- [85] Manley G.A. (1990) *Peripheral Hearing Mechanisms in Reptiles and Birds.* Springer-Verlag, Heidelberg.
- [86] Manley G., Köppl C. (1998) Phylogenetic development of the cochlea and its innervation. *Curr. Opin. Neurobiol.* 8: 468-474.
- [87] Manley, G. (2000) Cochlear mechanisms from a phylogenetic viewpoint. *Proc. Natl. Acad. Sci.* 97(22): 11736-11743.
- [88] Manley G. A., Kirk D. L., Köppl C., Yates G. K. (2001) In vivo evidence for a cochlear amplifier in the hair-cell bundle of lizards. *Proc. Natl. Acad. Sci. USA*, 98: 2826-2831.

- [89] Manley G.A., Fay R.R., Popper A.N. (2008) Active Processes and Otoacoustic Emissions in Hearing, Springer Handbook of Auditory Research, Springer Verlag, Heidelberg.
- [90] Manoussaki D., Dimitriadis E.K., Chadwick R.S. (2006) Cochlea's graded curvature effect on low frequency waves. *Phys. Rev. Lett.* 96 (8): 088701.
- [91] Manoussaki D., Chadwick R.S., Ketten D.R., Arruda J., Dimitriadis E.K., O'Malley J.T. (2008) The influence of cochlear shape on low-frequency hearing. *Proc. Natl. Acad. Sci. USA*, 105(16): 6162-6166.
- [92] Martin P., Hudspeth A.J. (1999) Active hair-bundle movements can amplify a hair cell's response to oscillatory mechanical stimuli. *Proc. Natl. Acad. Sci.* 96: 14306-14311.
- [93] Martin P., Hudspeth A.J., Jülicher F. (2001) Comparison of a hair bundle's spontaneous oscillations with its response to mechanical stimulation reveals the underlying active process. *Proc. Natl. Acad. Sci.* 98(25): 14380-14385.
- [94] Martin P., Bozovic D., Choe Y., Hudspeth A.J. (2003) Spontaneous oscillation by hair bundles of the bullfrog's sacculus. *J. Neurosci.* 23: 4533-4548.
- [95] Martin P. (2008) Active Hair-Bundle Motility of the Hair Cells of Vestibular and Auditory Organs. In: *Active Processes and Otoacoustic Emissions in Hearing, Springer Handbook of Auditory Research*, Manley G.A., Fay R.R., Popper A.N. (Eds.), Springer Verlag.
- [96] Maruno K., Ankiewicz A., Akhmediev N. (2002) Exact soliton solutions of the one-dimensional complex Swift-Hohenberg equation. *Physica D*, 176: 44-66.
- [97] Mauermann M., Uppenkamp S., van Hengel P., Kollmeier B. (1999) Evidence for the distortion product frequency place as a source of distortion product otoacoustic emission (DPOAE) fine structure in humans. I. Fine structure and higher-order DPOAE as a function of the frequency ratio  $f_2/f_1$ . *J. Acoust. Soc. Am.* 106 (6): 3473-3483.
- [98] McElveen J.T., Goode R.L., Miller C., Falk S.A. (1982) Effect of mastoid cavity modification on middle ear sound transmission. *Ann. Otol. Rhinol. Laryngol.* 91(5 Pt 1): 526-32.
- [99] Meaud J., Grosh K. (2012) Response to a Pure Tone in a Nonlinear Mechanical-Electrical-Acoustical Model of the Cochlea *Biophys. J.* 102: 1237-1246.
- [100] Moleti A., Paternoster N., Bertaccini D., Sisto R., Sanjust F. Otoacoustic emissions in time-domain solutions of nonlinear non-local cochlear models. *J. Acoust. Soc. Am.* 126(5): 2425-2436.

- [101] Nadrowski B., Martin P., Jülicher F. (2004). Active hair-bundle motility harnesses noise to operate near an optimum of mechanosensitivity. *Proc. Natl. Acad. Sci.*, 101: 12195-12200.
- [102] Nadrowski B. (2004) Mechanical properties of active hair-bundles. Dissertation, Paris VII University.
- [103] Naidu, R.C., Mountain, D. C. (1998) Measurements of the stiffness map challenge a basic tenet of cochlear theories. *Hear. Res.* 124: 124-131.
- [104] Naidu, R.C., Mountain, D. C. (2000) Longitudinal coupling within the basilar membrane and reticula lamina. *Symposium on Recent Developments in Auditory Mechanics*.
- [105] Naidu, R.C., Mountain, D. C. (2001) Longitudinal coupling in the basilar membrane. *J. Assoc. Res. Otolaryngol.* 02: 257-267.
- [106] Neely, S. T. (1981) Finite difference solution of a two-dimensional mathematical model of the cochlea. *J. Acoust. Soc. Am.* 69: 1386-1393.
- [107] Neely S., Kim D. (1986) A model for active elements in cochlear biomechanics. *J. Acoust. Soc. Am.* 79: 1472-1480.
- [108] Press W.H., Teukolsky S.A., Vetterling W.T., Flannery B.P. (1992) Numerical Recipes in C. Cambridge University Press.
- [109] Nuttall A.J., Dolan D.F. (1996) Steady-state sinusoidal velocity responses of the basilar membrane in guinea pig. *J. Acoust. Soc. Am.* 99(3): 1556-1565.
- [110] Nuttall A.L., Guo M., Ren T., Dolan D.F. (1997) Basilar membrane velocity noise. *Hear. Res.* 114: 35-42.
- [111] Nuttall A.L., Grosh K., Zheng J., de Boer E., Zou Y., Ren T. (2004) Spontaneous Basilar Membrane Oscillation and Otoacoustic Emission at 15 kHz in a Guinea Pig. *J. Assoc. Res. Otolaryngol.* 5: 337-348.
- [112] Ó Maoiléidigh D., Jülicher F. (2010) The interplay between active hair bundle motility and electromotility in the cochlea. *J. Acoust. Soc. Am.* 128: 1175-1190.
- [113] Osipov G., Sushchik M. (1998) Synchronized clusters and multistability in arrays of oscillators with different natural frequencies. *Phys. Rev. E* 58: 7198-7207.
- [114] Ospeck M., Eguiluz V. M., Magnasco M. O. (2001) Evidence of a Hopf bifurcation in frog hair cells. *Biophys J.* 80: 2597-2607.
- [115] Penner M.J., Glotzbach L., Huang T. (1993) Spontaneous otoacoustic emissions: Measurement and data. *Hear. Res.* 68: 229-237.

- [116] Pickles J.O. (2003) An Introduction to the Physiology of Hearing - 2nd Edition. Academic Press, London, UK.
- [117] Pierson L.L., Gerhardt K.J., Rodriguez G.P., Yanke R.B. (1994) Relationship between outer ear resonance and permanent noise-induced hearing loss. *Am. J. Otolaryngol.* 15: 37-40.
- [118] Probst R., Lonsbury-Martin B.K., Martin G.K. (1991) A review of otoacoustic emissions. *J. Acoust. Soc. Am.* 89: 2027-2067.
- [119] Puria S. (2003) Measurements of human middle ear forward and reverse acoustics: Implications for otoacoustic emissions. *J. Acoust. Soc. Am.* 113: 2773-2789.
- [120] Puria S., Fay R. R., Popper A. N. (2013) The Middle Ear. Science, Otorhinology, and Technology. Springer Handbook of Auditory Research, Volume 46.
- [121] Purves D., Augustine G.J., Fitzpatrick D., Hall W.C., LaMantia A., McNamara J.O., White L.E. (2001) Neuroscience. Sinauer Associates, Inc., 2nd Ed.
- [122] Rabbitt R. D., Boyle R., Highstein S. M. (2010) Mechanical amplification by hair cells in the semicircular canals. *Proc. Natl. Acad. Sci. USA*, 107: 3864-3869.
- [123] Reichenbach T., Hudspeth A.J. (2010) A ratchet mechanism for amplification in low-frequency mammalian hearing. *Proc. Natl. Acad. Sci. USA*, 107(11): 4973-4978.
- [124] Reichenbach T., Hudspeth A.J. (2010) Dual contribution to amplification in the mammalian inner ear. *Phys. Rev. Lett.* 105(11): 118102.
- [125] Richter C.P., Emadi G., Getnick G., Quesnel A., Dallos P. (2007) Tectorial membrane stiffness gradients. *Biophys J.* 93: 2265-2276.
- [126] Rhode W.S. (1971) Observations of the vibration of the basilar membrane in squirrel monkeys using the Mössbauer technique. *J. Acoust. Soc. Am.* 49: 1218-1231.
- [127] Rhode, W.S. (1973) An investigation of post-mortem cochlear mechanics using the Mössbauer effect. In: *Basic Mechanisms of Hearing*, Møller A.R. (Ed.), Academic Press, New York. p: 49-67.
- [128] Rhode W.S., Robles L. (1974) Evidence from Mössbauer experiments for nonlinear vibration in the cochlea. *J. Acoust. Soc. Am.* 55(3): 588-596.
- [129] Robles L., Ruggero M.A. (2001) Mechanics of the Mammalian Cochlea. *Physiol. Rev.* 81(3): 1305-1352.

- [130] Russell I.J., Sellick P.M. (1977) The tuning properties of cochlear hair cells. In: *Psychophysics and Physiology of Hearing*, Evans E.F., Wilson J.P. (Eds.), Academic Press, London.
- [131] Russell, A.F. (1992) Heritability of spontaneous otoacoustic emissions. Dissertation, University of Illinois, Urbana-Champaign, IL, University Microfilms International, Ann Arbor, MI.
- [132] Russell I.J., Nilsen K.E. (1997) The location of the cochlear amplifier: Spatial representation of a single tone on the guinea pig basilar membrane. *Proc. Natl. Acad. Sci.* 99: 2660-2664.
- [133] Santo-Sacchi J. (1992) On the Frequency Limit and Phase of Outer Hair Cell Motility: Effects of the Membrane Filter. *J. Neurosci.* (5): 1906-1916.
- [134] Scott, A.C. (2005) *Encyclopedia of Nonlinear Science*. Routledge, Taylor & Francis Group, New York, NY.
- [135] Schloth, E. (1983) Relation between spectral composition of spontaneous otoacoustic emissions and fine-structure of threshold in quiet. *Acustica*, 53: 250-256.
- [136] Shera C.A., Guinan J.J. (1999) Evoked otoacoustic emissions arise by two fundamentally different mechanisms: A taxonomy for mammalian OAEs. *J. Acoust. Soc. Am.* 105 (2): 782-798.
- [137] Shera C.A. (2003) Mammalian spontaneous otoacoustic emissions are amplitude-stabilized cochlear standing waves. *J. Acoust. Soc. Am.* 114: 244-262.
- [138] Sim J.H., Chatzimichalis M., Lauxmann M., Rösli C., Eiber A., Huber A.M. (2010) Complex stapes motions in human ears. *J. Assoc. Res. Otolaryngol.* 11(3): 329-341.
- [139] Sisto R., Moleti A., Paternoster N., Botti T., Bertaccini D. (2010) Different models of the active cochlea, and how to implement them in the state-space formalism. *J. Acoust. Soc. Am.* 128(3): 1191-202.
- [140] Spiegel M.F., Watson C.S. (1984) Performance on frequency-discrimination tasks by musicians and nonmusicians. *J. Acoust. Soc. Am.* 76 (6): 1690-1695.
- [141] Spoendlin H. (1966) The organization of the cochlear receptor. *Adv. Oto-Rhino-Laryngol.* 13: 1-227.
- [142] Spoendlin H. (1970) Structural basis of peripheral frequency analysis. In: *Frequency analysis and periodicity detection in hearing*, R. Plomp, u . G. F. Smooresberg (Eds.), Leiden, p. 2-40.
- [143] Steele C.R., Zais J.G. (1985) Effect of coiling in a cochlear model. *J. Acoust. Soc. Am.* 77 (5): 1849-1852.

- [144] Strogatz S. H. (1994) *Nonlinear Dynamics and Chaos*. Perseus Books, Cambridge, Massachusetts.
- [145] Talmadge C.L., Tubis A., Wit H.P., Long G.R., (1991) Are spontaneous otoacoustic emissions generated by self-sustained cochlear oscillators? *J. Acoust. Soc. Am.* 89(5): 2391-2399.
- [146] Talmadge C.L., Long G.R., Murphy W.J., Tubis A. (1993) New off-line method for detecting spontaneous otoacoustic emissions in human subjects. *Hear. Res.* 71: 170-182.
- [147] Talmadge C.L., Tubis A. (1993) On modeling the connection between spontaneous and evoked otoacoustic emissions. In: *Biophysics of Hair Cell Sensory Systems*, Duifhuis H. , Horst J. W., van Dijk P., van Netten S. M. (Eds.), World Scientific, Singapore. p. 25-32.
- [148] Talmadge C.L., Tubis A., Long G.R., Piskorski P. (1998) Modeling otoacoustic emission and hearing threshold fine structures. *J. Acoust. Soc. Am.* 104: 1517-1543.
- [149] Taschenberger G., Manley G.A. (1997) Spontaneous otoacoustic emissions in the barn owl. *Hear. Res.* 110: 61-76.
- [150] Thorne M., Salt A.N., DeMott J.E., Henson M.M., Henson O.W. Jr., Gewalt S.L. (1999) Cochlear fluid space dimensions for six species derived from reconstructions of three-dimensional magnetic resonance images. *Laryngoscope*, 109(10): 1661-1668.
- [151] Triki H., Hayatb T., Aldossaryc O.M., Biswas A. (2011) Solitary wave and shock wave solutions to a second order wave equation of Korteweg-de Vries type. *Appl. Math. Comput.* 217(21): 8852-8855.
- [152] Vilfan A., Duke T. (2008) Frequency Clustering in Spontaneous Otoacoustic Emissions from a Lizard's Ear. *Biophys. J.* 95: 4622-4630.
- [153] Voldrich L. (1978) Mechanical properties of basilar membrane. *Acta Otolaryngol.* 86: 331-335.
- [154] Voss S.E., Shera C.A. (2004) Simultaneous measurement of middle-ear input impedance and forward/reverse transmission in cat. *J. Acoust. Soc. Am.* 116(4 Pt 1): 2187-2198.
- [155] Wen B., Boahen K. (2003) A Linear Cochlear Model with Active Bidirectional Coupling. *The 25th Annual International Conference of the IEEE Engineering in Medicine and Biology Society (EMBC 2003)*, p. 2013-2016.
- [156] Wen B. (2006) Modeling the nonlinear active cochlea. Dissertation, University of Pennsylvania.
- [157] Wiggins S. (1996) Introduction to Applied Nonlinear Dynamical Systems and Chaos. Springer-Verlag, New-York.

- [158] Wit H., van Dijk P. (2012) Are human spontaneous otoacoustic emissions generated by a chain of coupled nonlinear oscillators? *J. Acoust. Soc. Am.* 132: 918-926.
- [159] Zweig G. (1976) Basilar membrane motion. *Cold Spring Harbor Symp. Quant. Biol.* 40: 619-633.
- [160] Zweig, G. (1991) Finding the impedance of the organ of Corti. *J. Acoust. Soc. Am.* 89: 1229-1254.
- [161] Zweig G., Shera C.A. (1995) The origin of periodicity in the spectrum of evoked otoacoustic emissions. *J. Acoust. Soc. Am.* 98: 2018-2047.
- [162] Zwicker E., Peisl W. (1990) Cochlear preprocessing in analog models, in digital models and in human inner ear. *Hear. Res.* 44: 209-216.
- [163] Zwislocki J.J. (1946) Über die mechanische Klanganalyse des Ohrs. *Experientia* 2: 10-18.
- [164] Zwislocki J.J. (1948) Theorie der Schneckenmechanik: Qualitative und quantitative Analyse. *Acta Oto-Laryngol. Suppl.* 72.
- [165] Zwislocki J.J. (2002) Auditory Sound Transmission. An Autobiographical Perspective. Lawrence Erlbaum Assoc Inc. Mahwah, New Jersey.

# Versicherung

Hiermit versichere ich, dass ich die vorliegende Arbeit ohne unzulässige Hilfe Dritter und ohne Benutzung anderer als der angegebenen Hilfsmittel angefertigt habe; die aus fremden Quellen direkt oder indirekt übernommenen Gedanken sind als solche kenntlich gemacht. Die Arbeit wurde bisher weder im Inland noch im Ausland in gleicher oder ähnlicher Form einer anderen Prüfungsbehörde vorgelegt.

Die Arbeit wurde am Max-Planck-Institut für Physik komplexer Systeme in der Abteilung für Biologische Physik angefertigt und von Prof. Dr. Frank Jülicher und Prof. Dr. Benjamin Lindner betreut.

Ich erkenne die Promotionsordnung der Fakultät Mathematik und Naturwissenschaften der Technischen Universität Dresden vom 23.02.2011 sowie deren Änderung vom 15.06.2011 an.

---

Florian Fruth